Quantitative Three Dimensional Atomic Resolution Characterisation of Non-stoichiometric Nanostructures in Doped Bismuth Ferrite

LiQiu Wang

Presented as a thesis for the degree of Ph.D. at the
school of Physics and Astronomy, University of Glasgow
January 2013

Abstract

Over the last decade, the lead-free, environmentally-friendly multiferroic material, $BiFeO_3$ (BFO), has once again received tremendous attention from researchers, not only for its fundamental properties, but also for its potential applications such as novel devices that can be written by an electric field and read by a magnetic field. However, one of the most important limitations for applications is the high leakage current in pure materials. Doping has proved to be an effective way to reduce the leakage current caused by the electron hopping between Fe^{2+} and Fe^{3+}. In this work, a series of Nd^{3+} and Ti^{4+} co-doped BFO compositions have been studied using a combination of atomic resolution imaging and electron energy loss spectroscopy in STEM, especially concentrating on nanostructures within the $Bi_{0.85}Nd_{0.15}Fe_{0.9}Ti_{0.1}O_3$ composition, as nanostructures can play an important role in the properties of a crystal. Two types of novel defects – Nd-rich nanorod precipitates and Ti-cored anti-phase boundaries (APBs) are revealed for the first time. The 3D structures of these defects were fully reconstructed and verified by multislice frozen phonon image simulations. The very formation of these defects was shown to be caused by the excess doping of Ti into the material and their impact upon the matrix is discussed. The nanorods consist of 8 atom columns with two Nd columns in the very center forming the Nd oxide. Density functional theory calculation reveals that the structures of the nanorod and its surrounding perovskites are rather unusual. The Nd in the core is seven coordinated by oxygen while the coordination of B site Fe^{3+} at its surroundings are just five-coordinated by oxygen due to the strain between the nanorod and the surrounding perovskite. The APB is nonstoichiometric and can be treated as being constructed from two main structural units - terraces and steps. Within the terraces, Ti^{4+} occupy the centre of the terrace with Ti/Fe alternately occupying either side of the terrace. As for the step, this is constructed from iron oxide alone with a structure similar to γ-Fe_2O_3, and Ti is completely absent. Quantitative analysis of the structure shows the APB is negatively charged and this results in electric fields around the APBs that induce a local phase transformation from an antiferroelectric phase to a locally polarised phase in the perovskite matrix. Based on this thorough investigation of these defects, a new ionic compensation mechanism was proposed for reducing the conductivity of $BiFeO_3$ without the complications of introducing non-stoichiometric nanoscale defects.

Acknowledgements

I am very grateful for having the opportunity to be able to study in MCMP group under the supervision of Dr Ian MacLaren and Prof. Alan Craven. Their guidance, patience and encouragement have been greatly appreciated. Their attitude toward research has set up a very good example for me, which will guide me through my career whatever I will do in the future. Their caring, thoughtful, kind personality will never be forgotten. I am also very grateful for EPSRC founded me through my study. I would also like to give lots of thanks to Prof. Ian M Reaney who generously provided those precious samples and gave many fruitful and stimulating discussions and advice. The support from Dr Bernhard Schaffer and Dr Quentin Ramasse and other services at SuperSTEM have been incredible. To all the staff at SuperSTEM, I must say a big "thank you" to all of you. I am also very appreciated to Dr S. M. Selbach and Prof N. Spaldin for their wonderful calculation work.

The friendly environment provided by the MCMP group has been wonderful. Colloquiums organized by Dr Donald MacLaren have been a great benefit to my study. Technical staff is all very supportive. Especially, I would like to thank Dr Sam McFadzean for his useful discussions regarding TEM, and Mr Brian Miller who is missed very much for teaching and making TEM samples so patiently. I am also indebted to Dr Damien McGrouther for his invaluable help.

I would also like to say thank you all to other staff within the MCMP group and all the colleagues who stayed together in room 402 and 413 for making my study time so enjoyable and memorable.

A big thanks and a big hug should also be given to my Mum who is fighting for her lung cancer at the last stage. Without her support and encouragement and her wise guidance in my early years, this thesis wouldn't be made possible. I am also in debt to my sisters and brothers-in-law for looking my mum when she was ill. My daughter has contributed a lot to my thesis by being behaved very well, I would say, so a big hug and kiss to her. At last but not the least, my husband deserves more than thanks for being so thoughtful and so supportive whenever I needed it.

Declaration

This thesis has been written by myself and details the research I have carried out within the MCMP group under the supervision of Dr Ian MacLaren and Prof. Alan Craven in the school of Physics and Astronomy at the University of Glasgow from 2009 - 2013. The work described is my own except where otherwise stated.

This thesis has not previously been submitted for a higher degree.

Some parts of the work have been published in the following papers:

I. MacLaren, L. Q. Wang, B. Schaffer, Q. M. Ramasse, A. J. Craven, S. M. Selbach, N. A. Spaldin, S. Miao, K. Kalantari, I. M. Reaney, **(2013) Novel Nanorod Precipitate Formation in Neodymium and Titanium Codoped Bismuth Ferrite,** Advanced Functional Materials, Volume **23**, Issue **2**, 683-689.

I. M. Reaney, I. MacLaren, L.Q. Wang, B. Schaffer, A. J. Craven, K. Kalantari, I. Sterianou, S. Miao, S. Karimi, and D. C. Sinclair, **(2012) Defect chemistry of Ti-doped antiferroelectric $Bi_{0.85}Nd_{0.15}FeO_3$,** Applied Physics Letters, **100,** 182902.

L. Q. Wang, B. Schaffer, A. Craven, I. MacLaren, S. Miao and I. Reaney, **(2011) Atomic Scale Structural and Chemical Quantification of NonStoichiometric Defects in Ti and Bi Doped BiFeO3.** Microscopy and Microanalysis **17** (Suppl. 2, 1896-1897) doi:10.1017/S143192761101035X.

L. Q. Wang, B. Schaffer, I. MacLaren, S. Miao, A. J. Craven and I. M. Reaney**, (2012) Atomic scale structure and chemistry of anti-phase boundaries in $(Bi_{0.85}Nd_{0.15})(Fe_{0.9}Ti_{0.1})O_3$ ceramics**, Journal of Physics: Conference Series **371,** 012036.

L. Q. Wang, B. Schaffer, I. MacLaren, S. Miao, A. J. Craven and I. M. Reaney, **(2012) Atomic-resolution STEM imaging and EELS-SI of defects in $BiFeO_3$ ceramics co-doped with Nd and Ti,** Journal of Physics: Conference Series **371,** 012034.

Contents

Abstract i

Acknowledgements ii

Declaration iii

Contents iv

List of figures and tables viii

1 Introduction 1

1.1 Multiferroics 2

1.2 General Properties of Multiferroics 3

1.2.1 Ferroelectricity 3

1.2.1.1 Crystal symmetry with respect to ferroelectricity 3

1.2.1.2 Curie temperature and phase transitions 5

1.2.1.3 Domain and domain wall in ferroelectrics 6

1.2.1.4 Hysteresis 7

1.2.2 Ferromagnetism 8

1.2.3 Magnetoelectric (ME) effect - coupling between ferroelectricity and (anti-) ferromagnetism 10

1.3 Properties of BFO 11

1.3.1 Perovskites – ABO_3 corner sharing octahedra 11

1.3.2 Properties of $BiFeO_3$ (BFO) 12

1.4 Motivation of This Study 14

2 Instrumentation and Sample Preparation 21

2.1 Overview of The Microscopes Used in This Work 22

2.1.1 The FEI Tecnai T20 22

2.1.2 SuperSTEM2 27

2.1.3 Electron lenses and aberrations 29

2.1.3.1 Electromagnetic lenses 29
2.1.3.2 Defects of electromagnetic lenses - aberrations 31
2.1.3.2.1 Geometric aberrations 31
2.1.3.2.2 Chromatic aberration 35
2.1.4 Image resolution and aberration correction 36
2.1.4.1 Spherical aberration limited image resolution 39
2.1.4.2 Chromatic aberration limited image resolution 40
2.1.4.3 Diagnosis of spherical aberration – the electron Ronchigram 41
2.2 Imaging 43
2.2.1 Image contrast 43
2.2.2 Bright-field and ark-field diffraction contrast imaging – coherent imaging 43
2.2.3 High angle annular dark field (HAADF) imaging with STEM – incoherent imaging 45
2.3 Electron Energy-loss Spectroscopy 47
2.3.1 Interactions of electrons with sample 47
2.3.1.1 Elastic scattering 47
2.3.1.2 Inelastic scattering 48
2.3.2 Electron energy-loss spectrometer 48
2.3.3 EELS 50
2.3.4 Spectrum – imaging 52
2.4 Sample Preparation 54
2.4.1 Ceramic preparation 54
2.4.2 Specimens for TEM 54
3 Computational software related to data analysis 59
3.1 Introduction 59
3.2 Principal Component Analysis (PCA) 59
3.3 Drift Correction via The Statistically Determined Spatial Drift (SDSD) Method 64

3.4 iMtools 66
3.5 Distortion Correction and Primary Model Development 66
3.6 Image Simulation 67
3.6.1 Multislice algorithm 68
3.6.2 Frozen phonon method 70
3.6.3 QSTEM 71
3.7 Density Functional Theory 72
4 Characterisation of nanorod precipitates 77
4.1 Introduction 77
4.2 TEM Imaging of The Nanorods and Their Connection to The Domain Structure of $Bi_{0.85}Nd_{0.15}Fe_{0.9}Ti_{0.1}O_3$ 78
4.3 Quantitative Analysis of Atomic Resolution STEM Imaging and Chemical Mapping of The Nanorods from $Bi_{0.85}Nd_{0.15}Fe_{0.9}Ti_{0.1}O_3$ sample 80
4.3.1 Quantitative analysis of the atom positions from HAADF STEM images 80
4.3.2 Chemical mapping of the nanorods from the top view 85
4.3.3 Imaging of the nanorods from the side view 91
4.3.4 Chemical mapping of the nanorods from the side view 92
4.4 The 3-Dimensional Structure of The Nanorods 93
4.4.1 The primary 3D model of the structure of the nanorods 93
4.4.2 Optimum of the 3D structure model by DFT 94
4.4.3 Structural model confirmation by multislice image simulation-QSTEM 97
4.4.4 Summary of the features for the nanorod structural model 99
4.5 Properties of The Nanorods and Their Effects on The Perovskite Matrix 100
4.5.1 Strain interactions with the matrix, spontaneous alignment and domain pinning 100
4.5.2 Electronic properties of the nanorods 101

4.5.3 Doping level effect on the nanorods and the perovskite matrix 102
4.6 Conclusions 104
5 Novel anti-phase boundaries 108
5.1 Introduction 108
5.2 About The Novel APB 109
5.3 Quantitative Analysis of The APB - Terrace Part 111
5.3.1 Structural and chemical information about terrace 111
5.3.2 Creation of structural model and simulation results 113
5.4 Quantitative Analysis of The APB - Step Part 117
5.5 The Effect of The APB with Its Adjacent Matrix 122
5.6 Conclusions 125
6 Summary and Future Work 130
6.1 Summary 130
6.2 Future Work 131

List of Figures and Tables

List of Figures

Figure 1.1: A schematic diagram of relative permittivity of $BaTiO_3$ changes with the phase transitions.

Figure 1.2: A schematic diagram of Polarization vs. Electric Field (P-E) hysteresis loop for a typical ferroelectric crystal.

Figure 1.3: Four types of magnetic dipole ordering in magnetic materials.

Figure 1.4: (a) 3D network of corner sharing octahedra of O^{2-} ions (left) (b) A cubic ABO_3 perovskite-type unit cell (right).

Figure 1.5: A schematic hexagonal structure of BFO with pseudocubic unit cell (doubled perovskite unit cell).

Figure 1.6: Preliminary phase diagram for Bi_1-xNdxFeO3 derived using a combination of XRD, DSC, Raman, and TEM data.

Figure 2.1: A schematic diagram of FEI Tecnai T20 column consisting of illumination system (electron source, C1, C2/ C2 aperture), magnification system(objective lens, diffraction lens, intermediate lens and projector lenses, and objective, selected area apertures), SIS camera and GIF.

Figure 2.2: A principal ray diagram of FEI T20 showing the specimen being illuminated by a parallel beam and a bright-field image will be formed as the final image.

Figure 2.3: a) A schematic diagram of main components of the column of the Nion UltraSTEM 100 with an on-site picture of SuperSTEM2 (inserted). b) A principal ray diagram of SuperSTEM2 showing electrons are formed into a fine probe and is focused on the specimen after the aberration corrector.

Figure 2.4: A schematic section of a polepiece showing its structure and two paths of the electron ray due the radial component $\mathbf{B_r}$ of the magnetic field.

Figure 2.5: A schematic diagram showing spherical aberration - a point object is imaged as a disk with radius $r_s \approx C_s \alpha^3$ due to spherical aberration that causes the off-axis rays are not focused at the same point F as those paraxial rays.

Figure 2.6: Schematic diagram of axial astigmatism. Rays leaving an axial image point, focused by a lens (with axial astigmatism) into ellipses centred around F_x if they travel in x-z plane or F_y if they travel in y-z plane, with long axis normal to the plane they travel, or into a circle of smallest radius - the disc of least confusion.

Figure 2.7: Schematic diagram of coma aberration which causes an off-axis object point imaged as comet shaped. Rays travel through the peripheral field of the lens with an incident angle are focused at different point from those travel parallel to the optic axis or through the centre.

Figure 2.8: Schematic diagram shows electrons with different energies being focused at different planes due to chromatic aberration.

Figure 2.9: A schematic diagram of a focused beam on the specimen in CTEM showing the definition of convergence semi-angle α, which is determined by the condenser lens and condenser aperture and collection semi-angle β, which is determined by the spectrometer entrance aperture.

Figure 2.10: A schematic plot of $\sin\chi(\alpha)$ versus α showing the contrast transfer as a function of spatial frequency with uncorrected TEM. The first crossover indicating the maximum allowable spatial frequency for intuitive image interpretation. E_s is the envelope of spatial coherence of the source and E_t is the chromatic aberration envelope.

Figure 2.11: A typical electron Ronchigram with two characteristic rings of infinite magnification appear around the sample shadow image showing spherical aberration.

Figure 2.12: Ray diagrams showing how to form BF and DF images. A) a BF image formed from direct beam. B) a DF image formed from a specific diffracted beam by displacing the objective aperture. C) a DF image

formed by tilting the incident beam so that the scattered beam is on axis. The area selected by the objective aperture is shown on the viewing screen below each ray diagram.

Figure 2.13: A SAD pattern showing [001] orientation and its related DF image showing the grain boundaries clearly as marked by the light blue line ($BiFeO_3$ co-doped with 10% Nd, 3% Ti).

Figure 2.14: Schematic diagram shows relative positions of different detectors with semi-angles $\theta_1 <$ 10 mrad (BF), 10 mrad $< \theta_2 <$ 50 mrad (MAADF), $\theta_3 >$ 50 mrad (HAADF).

Figure 2.15: Schematic diagram showing interactions of direct beam with specimen.

Figure 2.16: EELS showing different energy loss regions of spectrum. A) a spectrum showing ZLP as marked in orange rectangle and the rest of the peaks are Plasmon caused by multiple excitation; Plasmon peaks are rather high because the sample is very thick. B) a spectrum showing core-loss region with characteristic ionization edges labelled .

Figure 2.17: A schematic diagram of spectrum imaging technique, which can be used for quantitative analysis.

Figure 2.18: Images of same silicon sample taken at same conditions of TEM. a) Before gentle milling. b) After gentle milling.

Figure 3.1: Comparison of spectra before and after PCA: left is the original spectrum; right is the spectrum after PCA was applied

Figure 3.2: An example of the screen plot, showing the correlation between log eigenvalue and components. Significant features are represented by those exponentially decreased principal component, experimental random noise are represented by the straight line in the scree plot. 10 components reconstructed spectrum image showing the random back ground noise has been greatly reduced.

Figure 3.3: Selected pairs of the loading spectra and the corresponding score images of the components showing significant features are represented by those

exponentially decreased principal components in the scree plot of Figure 3.2.

Figure 3.4: (a) One slice from a series of images taken using a dwell time of 5μs/pixel; (b) A sum of the image series after spatial drift correction.

Figure 3.5: Interface of iMtools and fitted peak image (top-right) from the SDSD corrected HAADF image (left) together with corresponding coordinates list.

Figure 3.6: A chart of the corresponding defect in Figure 3.5 plotted with Excel using the coordinations (x, y) extracted by iMtools.

Figure 4.1: a) Dark field image of one area examined by HRSTEM; diffraction patterns insets show the crystal orientation to either side of the domain boundary, which appears as a bright diagonal line. b) HAADF image of nanorod precipitates in an end-on orientation.

Figure 4.2: A typical procedure for linear distortions correction, including shifting peak positions to zero, rotation correction, shear correction and magnification correction.

Figure 4.3: HAADF images showing six defects used for quantifying atomic positions. Scale bars can be worked out by the distance between two nearest bright A-site spots of the bulk matrix, which is about 3.965Å.

Figure 4.4: Corrected A-site positions for six defects: a) the positions for each of the six defect images, each in a different colour, together with a symmetry markers for the proposed 2mm plane symmetry of the defect; b) averages for each position after averaging all symmetrically equivalent positions to generate each data point, error bars are 3σ to make them clearly visible.

Figure 4.5: Processing steps involved in creating the maps shown in Figure 4.6: the initial maps are created from a PCA analysed spectrum image using the first 20 components, these are then normalised by division by the carbon map shown to try to normalise them to the total signal entering the spectrometer. Finally, maps are cleaned up by the application of a low pass filter.

Figure 4.6: Quantitative imaging and electron energy loss elemental mapping of the nanorods in an end-on orientation; a) HAADF image formed by summing 46 drift-corrected short acquisitions of one area. b) – e) elemental maps created from a EELS-SI of one such nanorod: b) Fe map; c) Nd map; d) Ti map; e) RGB map created where red represents Fe, green represents Nd and blue represents Ti; f) O K-edge EELS spectra from the nanorod core, outside the nanorod core and a Nd_2O_3 spectrum for reference; g) MLLS fit coefficient map for the O-K edge shape for bulk perovskite; h) MLLS fit coefficient map for the O-K edge shape for the Nd_2O_3 edge shown in f).

Figure 4.7: a) Elemental maps for another defect with similar results as in Figure 4.6. b) elemental maps for a defect but overlapped with normal BFO crystal matrix. HAADF images presented in both a) and b) were acquired simultaneously with EEL-SI.

Figure 4.8: Side views of some different nanorod precipitates (in all cases nanorods are indicated by yellow arrows): a) and b) lower magnification MAADF images, showing strain around the precipitates; c)-f) HAADF images formed by repeat scanning, alignment and summation of multiple scans.

Figure 4.9: Quantitative imaging and electron energy loss elemental mapping of the nanorods in side-on orientation; a) HAADF image of one such nanorod formed by summing 27 drift-corrected short acquisitions, pairs of Nd atoms along the beam direction are indicated by yellow arrows. b)-e) elemental maps created from a EELS-SI of one such nanorod, the nanorod lies between the arrows in all maps: b) Fe map; c) Nd map; d) Ti map; e) RGB map created where red represents Fe, green represents Nd and blue represent Ti.

Figure 4.10: The initial model of nanorods with all the B-sites atoms 6 coordinated.

Figure 4.11: Regions of the supercell model used for plotting local DOS in Figure 4.12; blue: matrix region; red: nanorod region and green: (outside red): interface region.

Figure 4.12: Atomic structure models after DFT structural relaxations in end-on orientation and their correlated DOS; a) the model with five-coordinated Ti towards the Nd nanorod columns; b) is the model with six-coordinated Ti away from the Nd nanorod columns; c) DOS from model with five-coordinated Ti; d) DOS from model (b) with six-coordinated Ti.

Figure 4.13: HAADF image simulations for this model compared to real images: a) end-on image of a nanorod; b) simulation of a nanorod extending through the entire 40 cell thickness of the crystal; c) image of the overlap between a defect and perfect crystal; d) simulation of 10 unit cells of nanorod on the entrance surface followed by 30 unit cells of perfect perovskite $BiFeO_3$; e) image of another overlap between a nanorod and perfect crystal; f) simulation of 10 cells of perfect perovskite overlaying 20 cells of nanorod, followed by 10 more cells of perfect crystal; g) side-on view of a nanorod (detail from the same image as used in Figure 4.9a); h) simulation of an image of a nanorod lying right at the entrance surface of the crystal viewed along the a-axis (as shown in Figure 4.12), followed by perfect crystal, with a total thickness of 30 unit cells.

Figure 4.14: MAADF image of BNFT-12.5_3 sample with inserted HAADF image, showing the coexistence of end-on (marked with pink colour) and side-on (marked with yellow-green colour) views of the nanorods.

Figure 4.15: MAADF images of BNFT-10_3 sample, showing the coexistence of end-on (marked with pink colour) and side-on (marked with yellow-green colour) view of the nanorods, but the length of side-on defects are quite short; inserted are HAADF images showing the coexistence of side-on views of two orientations.

Figure 4.16: MAADF images showing the doping level effect on density and strain with samples of BNFT-10_3, a); BNFT-12.5_3 ,b); BNFT-15_10, c).

Figure 5.1: a) DF image with SAD pattern showing an area with two darker ribbons running cross the sample; b) HAADF image reveals the two darker ribbons are actually APBs consisting of terrace parts with varied length and steps, and the dark spots between the two ribbons in DF image are

corresponding the nanorods in between the two APBs. The half unit cell shifting cross the boundary is marked by the green lines; horizontal shift of one perovskite unit cell at the steps is indicated by blue lines.

Figure 5.2: Atomic resolution STEM images and EELS maps of the APB (terrace part) along the first projection; the colour scales are shown for the false colour images and the same scale was used for both HAADF and BF images. Insets of the simulated images are overlaid on the experimental images using exactly the same contrast scale. The EELS maps for individual images show the full contrast range, whereas the contrast has been enhanced to remove background intensity and thus to enhance visibility of the main atomic columns in the RGB image.

Figure 5.3: Elemental maps from two other areas showing the chemistry similarity of the APBs (terrace part).

Figure 5.4: HAADF image and EELS maps of the antiphase boundary along the second (perpendicular) projection. An inset of a simulated image is overlaid on the HAADF image using exactly the same contrast scale. The EELS maps for individual images show the full contrast range, whereas the contrast has been enhanced to remove background intensity and thus to enhance visibility of the main atomic columns in the RGB image.

Figure 5.5: QSTEM simulation results from different models. a) From a model with no oxygen in the unit occupies the position corresponding the very bright spot in BF image and very dark place in HAADF image. b) From a model with only one position in the unit is fully occupied by oxygen, which shows bright spot as circled, and the other one is half occupied by oxygen. c) From a model with both positions in the unit occupied by oxygen, resulting bright spots are circled as well. d) From the final model with 4 mrad-tilted angle. f) The same BF image in grey scale as was used in Figure 5.2 for the comparison with image (d). The blue parallelogram marks the two close pairs of oxygen with contrast difference between them.

Figure 5.6: 2D visions from the final model of APB (the terrace part) with purple represents Bi atoms, red represents oxygen atoms, light blue for Ti and brown for Fe. a) Top view of the model. b) Tilted side view of the model to show the alternative B-site occupancies of Ti/Fe on either side of the terrace.

Figure 5.7: HAADF image (left) with two steps and corresponding BF image (right); For further comparison, the lower step is magnified and displayed together with the simulation results.

Figure 5.8: Elemental maps from EELS of different areas as indicated by simultaneously recorded HAADF images (in green framed). Colour indications are the same as before: red for Fe, blue for Ti and green for HAADF.

Figure 5.9: Co-efficiency fitting maps corresponding to the O K-edge reference spectra as displayed below and Fe ELNEFS. (Green colour represents the spectrum from the perovskite and red represents the spectrum from the step).

Figure 5.10: Top view of the 3D structural model for APB (step part) with main feature of the step marked with bright green parallelogram.

Figure 5.11: a) out-of-plane lattice parameter dependence on distance from the boundary; b) local polarisation dependence on distance from the boundary.

Figure 5.12: The repeat units for the calculation of charge densities for terrace (a) and for step (b); purple for Bi, brown for Fe, light-blue for Ti and red for O.

List of Tables

Table 1.1: Point groups for the seven crystal systems.

Table 2.1: Aberration coefficients and their corresponding conventional names.

Table 3.1: Steps for simulations of STEM images of thick specimen.

Table 4.1: Averaged atomic positions for the defect after reduction to *2mm* symmetry.

Table 4.2: Typical Mapping parameters using in creating the maps.

Chapter 1 Introduction

Multiferroics (for a definition see section 1.1) have been an intriguing study field in recent years because of their fascinating phenomena in physics and wide ranging applications like high-sensitivity ac magnetic field sensors and electrically tunable microwave devices such as filters, oscillators and phase shifters (in which the ferri-, ferro- or antiferro-magnetic resonance is tuned electrically instead of magnetically). One of the most appealing aspects of multiferroics is the so-called magnetoelectric (ME) effect, which means ferroelectric polarization can be controlled by a magnetic field and, conversely, magnetization can be manipulated by an electric field. This effect could be exploited for the development of new devices including novel spintronics and spin valves with electric field tuneable functions, or even non-volatile magnetic storage bits which can combine the advantages of FeRAMs (ferroelectric random access memories) and MRAMs (magnetic random access memories). However, there are not many materials that exhibit a strong ME effect - almost all of them are antiferromagnetic or weak ferromagnets [Mariya 1960, Hill 2000]. Regarding the weak ferromagnetism, there are two mechanisms. One originates from anisotropic superexchange interactions, and materials with this type of weak ferromagnetism normally have higher Néel temperatures. The other is from single spin anisotropy energy and materials with this type of magnetism tend to have low Néel temperatures [Mariya 1960], which limits their applications. As for $BiFeO_3$ (BFO), it has the advantages desired by device designers with both Curie temperature (~830ºC) and Néel temperature (~370ºC) well above room temperature. Furthermore, the origin of ferroelectricity is different from that of the antiferromagnetism. The former is caused by the structural distortion introduced by the *6s* lone pair electrons of A-site Bi and the later is from the transition metal *d*-electrons on the B-site iron. From this aspect, we might be able to manipulate the ferroelectricity and magnetism separately by substituting A and/or B-site atoms. In this thesis, investigations to a series of Nd and Ti co-doped BFO samples on nanoscale structures were carried out. The detailed rationale for these studies will be discussed in more detail in this chapter (section 4), as well as in further detail in chapters 4 and 5. This thesis is structured in the following manner: this chapter will briefly review the current state of knowledge on multiferroics with specific reference to bismuth ferrite and other

perovskite multiferroics, and will serve as an introduction to the whole thesis. Chapter 2 will serve as giving an overview of transmission electron microscopy (TEM) and scanning transmission electron microscopy (STEM). Chapter 3 will detail the data analysis and computer simulation approaches used in the research described in the following two chapters. Chapter 4 will then detail the atomic scale structure and chemistry of nanorod precipitates in Ti, Nd doped bismuth ferrite, together with their dependence on material composition. Chapter 5 will detail the atomic scale structure, chemistry and dielectric effects of antiphase boundaries in the same material. Chapter 6 then summarises the conclusions of these studies and outlines the future work that should be carried out in this area.

As the first chapter of this thesis, we will start with the definition of multiferroics. In particular, we will discuss two primary ferroic order parameters of multiferroics: ferroelectricity and related properties, ferromagnetism and related properties. The coupling between ferroelectricity and (anti-)ferromagnetism is considered and, finally, the general view of physical properties for BFO and the motivation of this study with Nd and Ti co-doped BFO is presented.

1.1 Multiferroics

Multiferroics were defined by H. Schmid [Schmid 1994] as materials that exhibit more than one primary ferroic order parameter simultaneously (i.e. in a single phase) such as ferroelectricity, ferromagnetism, ferroelasticity and ferrotoroidicity. Today the term multiferroics has been expanded to include materials that exhibit any type of long range magnetic ordering, spontaneous electric polarization, ferroelasticity and/or ferrotoroidicity. Specifically, coupling between ferroelectric and (anti-)ferromagnetic order parameters would lead to magnetoelectric (ME) effects, in which the magnetization can be adjusted by an applied electric field and vice versa. The search for multiferroics with a strong ME effect is driven by the prospect of controlling the polarization by applied magnetic fields and spins by applied voltages, and using this to construct new forms of multifunctional devices.

1.2 General Properties of Multiferroics

1.2.1 Ferroelectricity

1.2.1.1 Crystal symmetry with respect to ferroelectricity

A 3-dimensional (3D) crystal structure can be obtained by the repetition of a unit cell. A unit cell is described by giving the symmetry of the structure, the lattice parameters, and the coordinates for each atom. According to the relationships between the axes and angles of the unit cells, crystal structures can be classified into seven different crystal systems: **triclinic, monoclinic, orthorhombic, tetragonal, trigonal, hexagonal, and cubic.** A crystallographic unit cell is very similar to a space lattice, which is a mathematical description of repeating units in solid materials, but with the highest symmetry of the system. However, for the space lattice, an absolute requirement is identical surroundings around every single lattice point. Considering the criteria for the space lattice and crystallographic unit cell, there are only 14 space lattices called Bravais lattices that can be used to describe the structure of a crystal. These 14 Bravais lattices can be classified into seven crystal systems too. In addition, each of the Bravais lattices can possess symmetry elements like centres of symmetry, mirror planes, rotation axes and points of inversion symmetry. Operations of these symmetry elements can be combined to form a group of symmetry operations termed as point group. The reasons for the nomenclature *point group* is that the symmetry elements of these operations all pass through a single point of the object and leave the appearance of the crystal structure unchanged. There are 32 point groups in total, and each one can be classified into one of the seven crystal systems (see Table 1.1). Considering the operations of the 32 point groups and translational symmetry operations (pure translations, screw axes and glide planes) of the 14 Bravais lattices, there are only 230 unique combinations for three-dimensional symmetry, and these combinations are known as the 230 space groups. As for the 32 point groups, they can be further classified into (a) crystals having a center of symmetry and (b) crystals which do not possess a center of symmetry. Crystals with a center of symmetry include the 11 point groups labeled as centrosymmetric in Table 1.1. Crystals with these point groups cannot show polarity. The remaining 21 point groups do not have a center of symmetry (i.e. they are non-centrosymmetric). A crystal having no center of symmetry may possess one or more crystallographically unique directional

axes. All non-centrosymmetric point groups, except the 432 point group, may show spontaneous polarization resulting in the emergence of the piezoelectric effect (polarization can be caused by an applied mechanical stress, and not just by an applied electric field) along unique direction axis. Out of the 20 point groups, ten point groups (including 1, 2, m, mm2, 4, 4mm, 3, 3m, 6, and 6mm) have only one unique direction axis, in the sense that it is not repeated by any symmetry element. Such groups

Table 1.1. Point groups for the seven crystal systems.

Crystal Structure	Point Groups	Centro-Symmetric	Non-centrosymmetric	
			Piezoelectric	Pyroelectric
Triclinic	$\bar{1}$, 1	$\bar{1}$,	1	1
Monoclinic	2, m, 2/m	2/m	2, m	2, m
Orthorhombic	222, mm2, mmm	mmm	222, mm2	mm2
Tetragonal	$\bar{4}$, 422, 4, 4mm, $\bar{4}$2m, 4/m, (4/m)mm	4/m, (4/m)mm	4, 422, $\bar{4}$, 4mm, $\bar{4}$2m	4, 4mm
Trigonal	$\bar{3}$, $\bar{3}$m, 3, 32, 3m	$\bar{3}$, $\bar{3}$m	3, 32, 3m	3, 3m
Hexagonal	6, 622, $\bar{6}$, 6mm, $\bar{6}$m2, 6/m, (6/m)mm	6/m, (6/m)mm	6, $\bar{6}$, 622, 6mm, $\bar{6}$m2	6, 6mm
Cubic	23, m$\bar{3}$, 432, $\bar{4}$3m, m$\bar{3}$m	m$\bar{3}$, m$\bar{3}$m	23, $\bar{4}$3m	------

are also called ten polar point groups as listed in red color in Table 1.1. The pyroelectric effect/pyroelectricity, which results in the appearance of spontaneous polarization even in the absence of an external electric field can only occur in crystals with symmetry described by one of the ten polar point groups.

A very closely related property to pyroelectricity is ferroelectricity. A ferroelectric crystal, like a pyroelectric crystal, also shows spontaneous polarization from an applied electric field but the direction of the polarization can be reversed by the applied electric field. Most of ferroelectric crystals have a transition temperature (Curie point) above which their symmetry changes to a higher symmetry, non-polar group and only below which the symmetry is reduced to one of the polar groups.

1.2.1.2 Curie temperature and phase transitions

All ferroelectric materials have a transition temperature called the Curie point (T_c). At a temperature $T > T_c$ the crystal does not exhibit ferroelectricity i.e. it is paraelectric, while for $T < T_c$ it is ferroelectric. On decreasing the temperature through the Curie point, a ferroelectric crystal undergoes a structural phase transition from a centrosymmetric non-polar, i.e. non-ferroelectric, structure to a non-centrosymmetic polar, i.e. ferroelectric, structure. If there is more than one ferroelectric phase, the temperature at which the crystal transforms from one ferroelectric phase to another is called the transition temperature. Near the Curie point or transition temperatures, thermodynamic properties including dielectric, elastic, optical, and thermal constants show anomalous behavior. A maximum in the dielectric constant (or relative permittivity) can only be observed at the Curie temperature due to the phase change from a paraelectric phase to a ferroelectric phase. The temperature dependence of the dielectric constant well above the Curie point ($T > T_c$) in ferroelectric crystals is governed by the Curie-Weiss law:

$$\varepsilon = \varepsilon_0 + \frac{C}{T - T_c} \tag{1.1}$$

where ε is the permittivity of the material, ε_0 is the permittivity of vacuum, C is the Curie constant and T_c is the Curie temperature. Figure 1.1 shows a schematic diagram of relative permittivity of $BaTiO_3$ changing with several phase transitions.

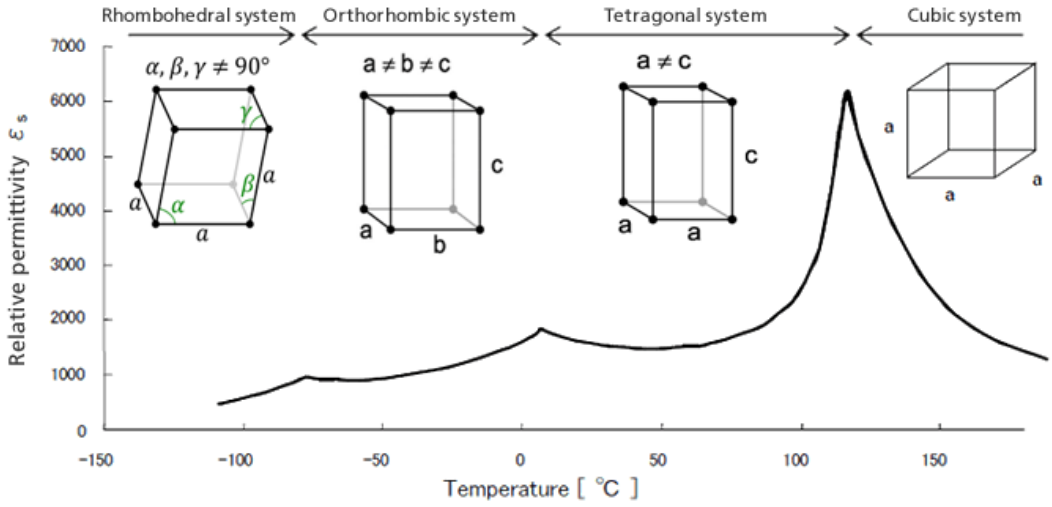

Figure 1.1. *A schematic diagram of relative permittivity of $BaTiO_3$ changes with the phase transitions (Adopted from http://www.murata.com/products/capacitor/design/).*

1.2.1.3 Domain and domain wall in ferroelectrics

Ferroelectric crystals possess microscopic regions with uniformly oriented spontaneous polarization called ferroelectric domains. Within a domain, all the electric dipoles are aligned in the same direction. A very strong field could lead to the reversal of the polarization in the domain, known as domain switching. A ferroelectric single crystal, when grown, might have multiple ferroelectric domains. The formation of ferroelectric domains is to minimize the electrostatic energy of depolarizing fields and the elastic energy that is associated with mechanical constraints to which the ferroelectric material is subjected as it is cooled through paraelectric–ferroelectric phase transition. Domains in a crystal will be separated by interfaces called domain walls. Domain walls are spatially extended regions of transition mediating the transfer of the order parameter from one domain to another. In comparison to domains, domain walls are not homogeneous and they can have their own symmetry and hence their own properties. A single domain can be obtained by domain wall motion, made possible by the application of an appropriate electric field. Characterization of domains and domain walls is very important when studying the material and its applications because the behavior of domains and domain walls is directly related to the switching characteristics of the multiferroics.

1.2.1.4 Hysteresis

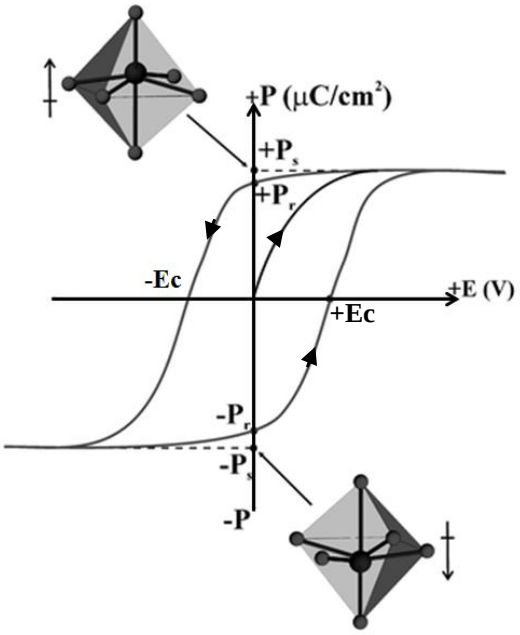

Figure 1.2. *A schematic diagram of Polarization vs. Electric Field (P-E) hysteresis loop for a typical ferroelectric crystal (after Ok 2006).*

As a ferroelectric crystal, the spontaneous alignment of atomic dipole moments can be reversed by an applied electric field, which is the most important characteristic of ferroelectric material. The polarization reversal can be observed from the single hysteresis loop. A typical single hysteresis loop is schematically shown in Figure 1.2. Initially, when the electric field is small, the polarization increases linearly with the field amplitude because the field is not strong enough to switch the domains with the unfavourably oriented direction of polarization. As the electric field strength is increased, these un-switched domains start to align in the positive direction, giving rise to a rapid non-linear increase in the polarization. At very high field levels, the polarization reaches a saturation value (P_s) and cannot be increased further. The value of the spontaneous polarization P_s is obtained by extrapolating the curve onto the polarization axes. The polarization does not fall to zero when the external field is removed. At zero external field, many of the domains still remain aligned in the positive direction, hence the crystal will show a remnant polarization P_r. The crystal cannot be completely depolarized until a field of a specific magnitude is applied in the negative direction. The external field needed to reduce the polarization to zero is called the

coercive field strength E_c. If the field is increased to a more negative value, the direction of polarization will be reversed.

1.2.2 Ferromagnetism

Similar to ferroelectricity, ferromagnetism arises from the spontaneous alignment of atomic magnetic dipole moments which gives a net magnetization. The driving force for ferromagnetism is the quantum mechanical exchange energy, which is minimized if all the electrons have the same spin orientation according to Stoner theory [Stoner 1933]. Many properties of ferromagnetic materials are analogous to those of ferroelectrics, but with the magnetization, **M**, corresponding to the electric polarization **P**; the magnetic field, **H**, corresponding to electric field, **E**; and the magnetic flux density, **B**, corresponding to electric displacement, **D**.

A ferromagnetic material will go through a phase transition from one that does not have a net magnetic moment (paramagnetic phase) to one that has a spontaneous magnetization even in the absence of an applied magnetic field (ferromagnetic phase) with temperature changes from high to low. The related temperature point is called Curie temperature, T_c, as well. With many ferromagnetic materials in the paramagnetic phase, the susceptibility of the material, χ, is governed by the Curie – Weiss law, namely,

$$\chi = \frac{C}{T - T_c} \tag{1.2}$$

However, in the immediate vicinity of the Curie point, the Curie-Weiss law fails to describe the susceptibility of many materials, since it is based on a mean-field approximation. If the phase transition is from paramagnetic to antiferromagnetic, the corresponding temperature point is called Neel temperature, $T_{N.}$

Apart from ferromagnetic and antiferromagnetic ordering, there are other types of magnetic ordering such as paramagnetic, ferrimagnetic or weak ferromagnetic ordering, as shown in Figure 1.3. Ferrimagnetic is like antiferromagnetic order with dipoles aligned antiparallel but some of the dipole moments are larger than others, so the material has a net magnetic moment. Weak ferromagnetic ordering is used to describe antiferromagnets with a small canting of the spins away from antiparallel alignment. This results in a small net magnetization, normally at low temperature.

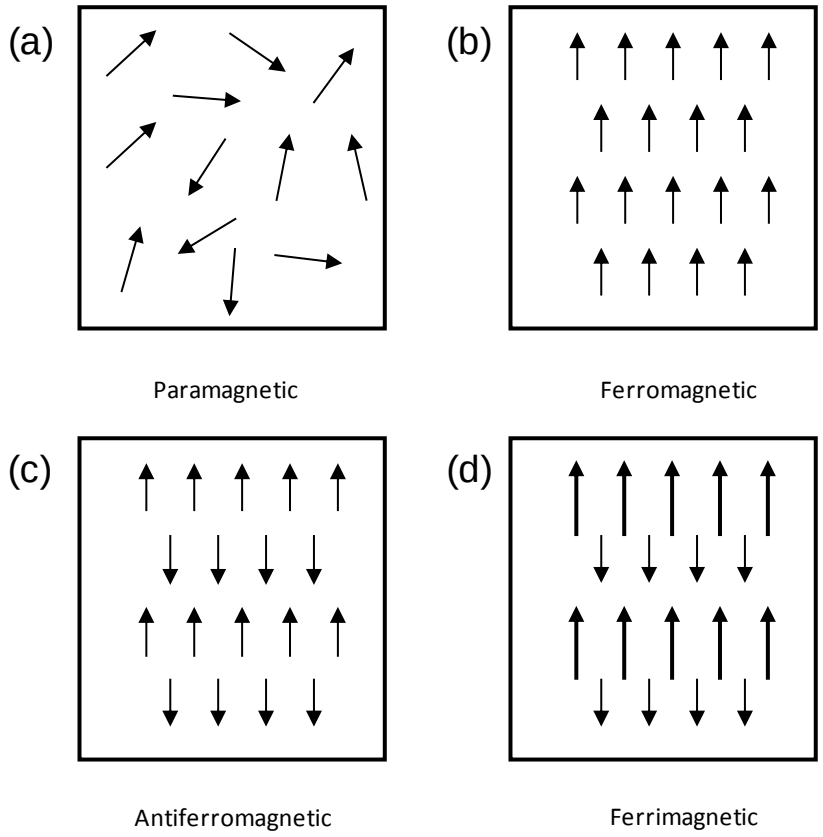

Figure 1.3. *Four types of magnetic dipole ordering in magnetic materials.*
(a) Paramagnetic; (b) Ferromagnetic; (c) Antiferromagnetic; (d) Ferrimagnetic.

Ferromagnetic materials have domains and normally do not show net magnetizations because the magnetizations of domains in the sample are oriented in different directions. When a magnetic field, **H**, is applied to the sample, the subsequent reorientation of domains will result in the net magnetization and flux density, **B**. In an analogous manner to a ferroelectric material, a hysteresis loop can be obtained with a ferromagnet by applying a magnetic field. A hysteresis loop (similar to Figure 1.2) starts with the unmagnetised state of the ferromagnetic material, and with the applied magnetic field increasing in the positive direction, the magnetization increases from zero to a saturation value, $\mathbf{M_s}$, due to the motion and growth of the magnetic domains. When this saturation point is reached, the magnetisation curve no longer retraces the original curve when **H** is reduced. This is because the irreversibility of the domain wall displacements. When the applied field **H** decreases to zero again, the sample still retains some magnetisation, known as remnant magnetisation, $\mathbf{M_r}$, due to the existence of some

domains still aligned in the original direction of the applied field. The reverse field required to reduce the corresponding magnetic induction, $\mathbf{B_r}$, to zero is termed as the coercivity, $\mathbf{H_c}$. As the field is continuously increased in the negative direction, the material will again become magnetically saturated but in the opposite direction, thus switching the magnetisation.

1.2.3 Magnetoelectric (ME) effect - coupling between ferroelectricity and (anti-) ferromagnetism

In multiferroics, coupling between (anti-) ferroelectricity and (anti-) ferromagnetism will lead to the ME effect which means magnetic (electric) polarization will be induced by applying an external electric (magnetic) field. The effects can be linear or/and non-linear with respect to the external fields. The effect can be obtained from the differentiation of the expansion of the free energy of a material [Fiebig 2005], leading to the polarization in the *i* direction can be represented by

$$P_i\left(\vec{E},\vec{H}\right) = \frac{\partial F}{\partial E_i} = P_i^S + \varepsilon_0\varepsilon_{ij}E_j + \alpha_{ij}H_j + \frac{1}{2}\beta_{ijk}H_jH_k + \gamma_{ijk}H_iE_j - \ \ldots \quad (1.3)$$

and to the magnetization in the *i* direction

$$M_i\left(\vec{E},\vec{H}\right) = \frac{\partial F}{\partial H_i} = M_i^S + \mu_0\mu_{ij}H_j + \alpha_{ij}E_i + \beta_{ijk}E_iH_j + \frac{1}{2}\gamma_{ijk}E_jE_k - \ \ldots \quad (1.4)$$

P_i^S and M_i^S are the spontaneous polarization and magnetization. $\vec{E}$ and $\vec{H}$ the electric and magnetic field, tensor $\hat{\alpha}$ corresponds to induction of polarization by a magnetic field or of magnetization by an electric field which is termed as the linear ME effect. High-order ME effects are defined by the tensors $\hat{\beta}$ and $\hat{\gamma}$. But most research is focused on the linear ME effect and simply use the word "ME effect" to mean the linear effect. Nevertheless, it is this prospective property that has driven the search for the materials with a ME to construct new forms of multiferroic devices. However, much of the early work, which tried to find materials with both ferroelectricity and ferromagnetism in one material, have proved this is not easy - almost every known experimental case is antiferromagnetic if it is ferroelectric; very few insulators are true ferromagnets [Anderson 1959]. Even with intensive study in recent years, there are still not many materials that can possess these two order parameters together. This can be understood

in terms of the following points: 1) The crystal symmetry factor: some crystal symmetries prohibit certain spontaneous orders developing [Schmid 2008]. 2) The electronic structure factor: to be ferroelectrics in perovskite-structure oxides with transition metals, the hybridization between the transition ions, which need to have empty *d* shells, with O 2*p* ions is essential. But, the existence of magnetic moment, and the consequent existence of magnetic ordering, requires the *d*-orbital to be partially occupied [Hill 2000]. Thus, these two order parameters turned out to be mutually exclusive. In addition, even if these two orders do coexist, like in BFO (with weak ferromagnetism of mainly antiferromagnetic crystals), the coupling between them is not strong enough to be usable due to the fact that the mechanisms of ferroelectricity and magnetism are quite different and effectively decoupled [Katsufuji 2001, Kimura 2003]. In BFO, the ferroelectricity is largely derived from the structural distortion of magnetic oxides induced by the stereochemically active 6*s* lone pair electrons of A-site Bi, while the magnetism is from the antisymmetric superexchange including the spin-orbital coupling with O anions from B-site transition-metal ions [Moriya 1960] which results in the weak ferromagnetism or canted ferromagnetism in this antiferromagnetic material. Thus interactions between the ferroelectric and antiferromagnetic order are generally very weak. Nevertheless, due to its higher phase transition temperature, BFO is still considered by many workers as a very good candidate for the design of future novel devices.

1.3 Properties of BFO

Since a large class of ferroelectric crystals including BFO is made up of perovskite-like structure, we will talk about perovskite structure first, and then specifically about the physical properties of BFO.

1.3.1 Perovskites – ABO_3 corner sharing octahedra

Perovskites take their name from the calcium titanium oxide ($CaTiO_3$) compound, which was first discovered in the Ural Mountains of Russia by Gustav Rose in 1839. A typical perovskite structure ABO_3 with cubic unit cell is shown in Figure 1.4(a), containing corner-sharing octahedra of O^{2-} ions. Inside each octahedron is a cation B^{b+} where 'b' varies from 3 to 6. The space between the octahedra is occupied by the A^{a+} ions where 'a' varies from 1 to 3. In the ideal cubic unit cell, 12-coordinated A-

site cations sit on the corners of the cube, octahedral O ions on the faces, and the B ion is in the center of the octahedral cage, see Figure 1.4(b). Due to the flexibility of the corner-sharing octahedra, the perovskite structure can be easily distorted to accommodate a wide range of valence states on both the A- and B- sites by expanding, contracting the lattice or by rotating the bond angles. The resulting symmetry of distorted perovskite could be tetragonal, orthorhombic, rhombohedral or monoclinic.

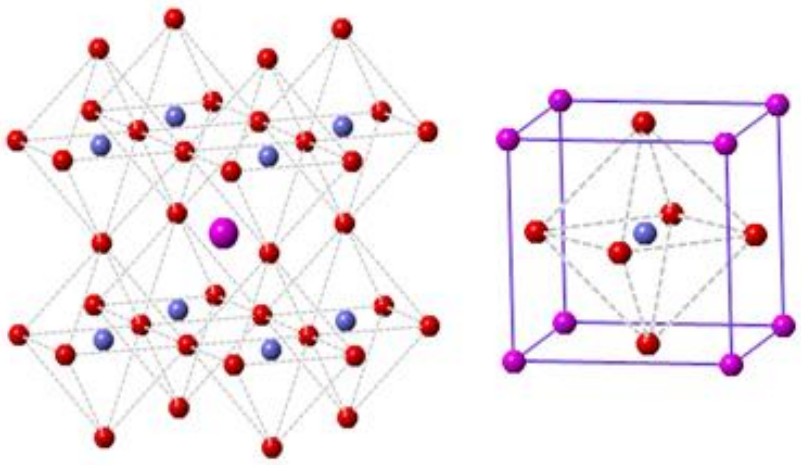

Figure 1.4. *(a) 3D of corner sharing octahedra of O^{2-} ions (left) (b) A cubic ABO_3 perovskite-type unit cell (right). [Red for O, magenta for A-site, slateblue for B-site].*

1.3.2 Properties of $BiFeO_3$ (BFO)

At room temperature, BFO has a rhombohedrally distorted perovskite-like structure with *R3c* symmetry. A schematic hexagonal structure with a rhombohedral unit cell (consisting of two distorted perovskite unit cells connected along their body diagonal) is shown in Figure 1.5. The perovskite-like unit cell has a parameter of $a_{pc} \approx$ 3.96Å, $\alpha_{pc} \approx$ 89.3-89.4˚ (pc = pseudocubic) with ferroelectric polarization along [111] direction of the pseudocubic unit or along the [001] direction of the hexagon if the structure is described in hexagonal unit [Lebeugle 2008]. The electric polarization is induced by the structural distortion caused by the stereochemically active lone-pair orbital of $6s^2$ of Bi^{3+}. The FeO_6 octahedra are rotated in anti-phase around the same $[111]_{pc}$ axis by 13.8°, with the Fe cation shifted along the same axis away from the centre of an oxygen octahedron [Zavaliche 2006]. Below the Curie temperature (Tc ≈ 830°C), BFO is ferroelectric [Teague 1973-1974]. Neutron diffraction measurements [Kiselev 1963] revealed that BFO is antiferromagnetic (AFM) below Neel temperature

($T_N \approx 370$ºC). The magnetic structure is of **G**-type with each Fe^{3+} magnetic ion surrounded by six Fe^{3+} nearest neighbours with anti-parallel magnetic moments. High resolution neutron diffraction studies [Sosnowska 1982, 1992] and line-shape analysis of nuclear magnetic resonance spectra [Zalesskii 2000] have confirmed that this G-type AFM is modified by a long-range cycloidal spiral incommensurate modulation in the $[110]_h$ (where h=hexagonal) direction with a long period, $\lambda = 620$Å within a $(110)_h$ spin rotation plane. Although BFO should exhibit weak ferromagnetism due to an antisymmetric superexchange with spin-orbital interactions [Dzyaloshinsky 1958, Moriya 1960], this canted magnetism is actually completely averaged out by the spin cycloidal structure. Thus, it is difficult to observe the linear ME effect in BFO, although its crystal symmetry R3c allows the appearance of the linear ME effect. Indeed, only the

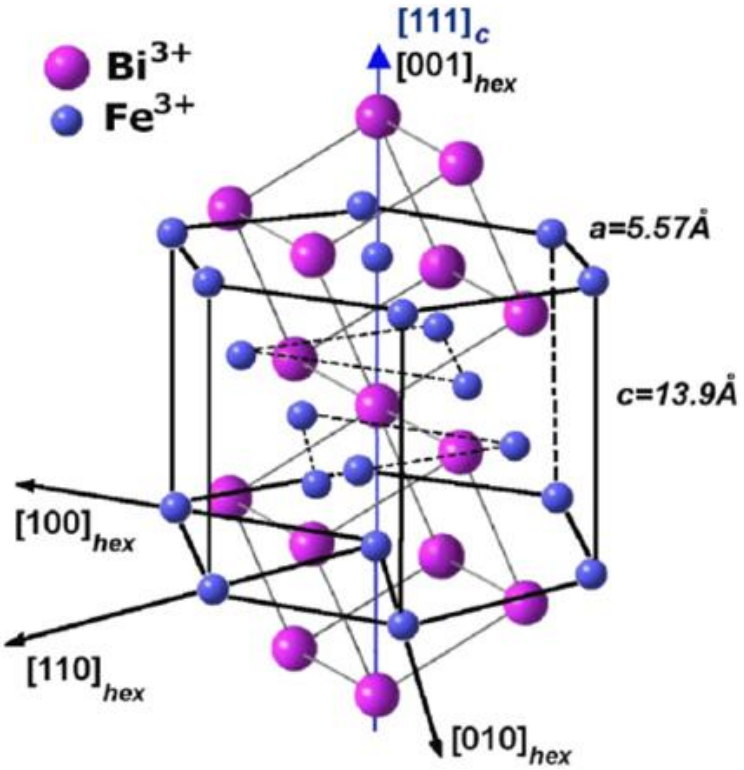

Figure 1.5. *A schematic hexagonal structure of BFO with pseudocubic unit cell (doubled perovskite unit cell) [Lazenca 2012]. The polarisation axis of Fe cations is along the pseudocubic <111> direction and the long-range cycloidal spiral incommensurate modulation is along the [110] of hexagonal with a period of λ = 620Å. For clarity, oxygen is not displayed.*

quadratic effect has been observed [Tabarez-Munoz 1985]. However, as the magnetoelectric coupling is determined by the structure and magnetic symmetry of a crystal [Neaton 2005, Hill 2000, Schmid 2008, Ederer 2005], small modifications might alter, eliminate or allow magnetoelectric effects. The linear effect may be recovered if the spiral is 'unwound' by applying large magnetic fields of 20T [Popov 1993, Kadomtseva 1995, Popov 2001], by attempting to introduce thin-film epitaxial constraints [Wang 2003, Bai 2005, Holcomb 2010] or by chemical substitutions [Yuan 2006, Hu 2009, Levin 2010].

1.4 Motivation of This Study

As we know, the lead zirconate titanate (PZT) based family of ferroelectric materials has been widely used in applications such as ultrasound transducers and other sensors, actuators and data storage. However, due to the toxicity of lead and the resulting EU legislation mandating the reduction or elimination of lead in many applications, it is desirable to find new materials to replace PZT-based materials in their different applications. Thus BFO has drawn tremendous interest from researchers in recent years, both for the multiferroic properties and their applications, outlined above, as well as for use as a basis for lead-free ferroelectric and piezoelectric ceramics. Polycrystalline (ceramic) and thin film studies have provided a great opportunity for understanding the fundamental properties of BFO as they are easier to make and offer a larger variety of easily achievable compositional modifications than single crystals. This is because subtle changes in atomic composition can induce distortion of the perovskite cell that might have dramatic impacts on the properties of the material such as structural evolution, transport properties, magnetic properties and polarization. Within last decade, huge progress has been made in the understanding of both bulk and thin film BFO. Epitaxial thin film with large polarisation has been reported by Wang *et al.*[Wang 2003]. This large polarisation was originally thought to arise from a secondary phase, but later on it was confirmed by the measurement of high quality single crystal made by Lebeugle *et al.* [Lebeugle 2008] that such large polarisation actually represented the intrinsic polarization of BFO. With "strain engineering", large spontaneous polarizations caused by a transformation to a compressive-strain-induced tetragonally-distorted perovskite phase with a large *c/a* ratio of ~1.24, also called "T-phase", have been reported in

epitaxial films grown on the $LaAlO_3$ substrate [Zeches 2009, Zhang 2011]. Further theoretical study through DFT calculation [Hatt 2010] found out this highly strained "T-phase" structure actually has five coordinated Fe ions instead of six coordination in the bulk rhombohedral BFO phase. On the other hand, as the FE in BFO is directly associated with its structure, chemical modification becomes a popular method to investigate its FE properties. The effect of partial "isovalent" rare-earth (RE) substitution to A-site Bi^{3+} on thin films by Kan *et al.* with Sm, Gd and Dy [Kan 2010], and on ceramics by Karami and coworkers with La, Nd, Sm and Gd [Karami 2009, Levin 2010] has been investigated independently. All these studies have revealed a compositionally-driven structural change from rhombohedral (ferroelectric) to orthorhombic (antiferroelectric) with substantially improved electromechanical and magnetic properties. Within these studies, they have also observed a $PbZrO_3$-like (PZ-like) phase as a bridging phase of an antipolar order at the morphotropic phase boundary with Nd or Sm doped BFO [Karimi 2009, Borisevich 2012]. Using electron diffraction with electron transmission microscope (TEM), Karami *et al.* reported this unusual PZ-like phase is a derivative of $PbZrO_3$ with similar A-site displacement but with a further cell doubling along the c-axis, resulting the final cell parameters of $\sqrt{2}a_c \times 2\sqrt{2}a_c \times 4a_c$ (a_c is the cell parameter of the primitive perovskite). Figure 1.6 shows a preliminary phase diagram regarding Nd^{3+} substitution to A-site Bi^{3+} of BFO, derived using a combination of XRD (X-ray diffraction), differential scanning calorimetry (DSC), Raman, and TEM data [Karami 2009]. No trace of second phase within the PZ-like structure has been observed from the XRD data with 15% Nd doped BFO. However, preliminary electrical data shows the conductivity was too high to obtain radio-frequency measurements, which is quiet common with BFO materials. It has been reported that the high conductivity could be caused by the charge defects (e.g. oxygen vacancies and Bi^{3+} vacancies) or the polaron hopping between Fe^{2+} and Fe^{3+} [Yu 2008, Cui 2010]. In this case, Ti^{4+} was used as a donor dopant on the B-site with 15% Nd doped BFO to reduce the conductivity, which turned out to be very successful [Kalantari 2011]. More interestingly, during their investigation, they found T_C shows a non-linear trend with increasing Ti concentration (Ti<15%) while T_N still decreases linearly although no secondary phase has been observed with XRD. However, electron diffraction with 10% Ti doped $Bi_{0.85}Nd_{0.15}FeO_3$ did show an incommensurate structure

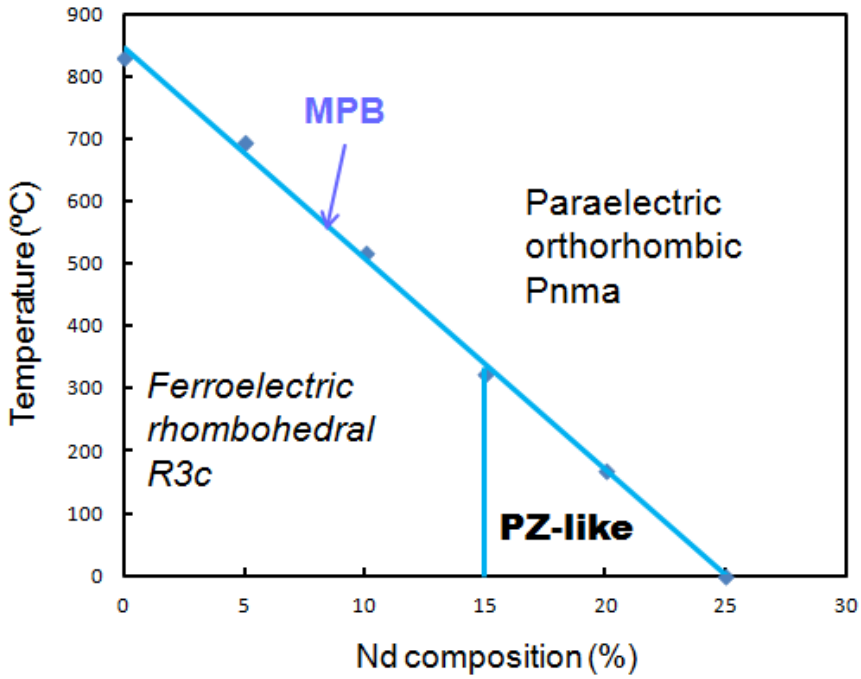

Figure 1.6. *Preliminary phase diagram for $Bi_{1-x}NdxFeO3$ derived using a combination of XRD, DSC, Raman, and TEM data [Karami 2009].*

which is consistent with the broadened peaks of XRD. This phenomenon could indicate a more complicated process may be going on with the effect of Ti doping as the concentration increases.

For thorough understanding of materials with fundamental physics, electron microscopy has played an important role, especially when it is down to microstructure or even nanostructure. Within recent studies related to BFO, this has been exemplified by the discrimination of T-phase from the bulk-like rhombohedral phase [Zeches 2009, Zhang 2011]; characterization of the structural evolution at the morphotropic phase boundary which revealed a $PbZrO_3$-like phase as a bridging phase for the ferroelectric-antiferroelectric phase transition [Karimi 2009, Borisevich 2012]. Using atomic resolution transmission electron microscopy, detailed analysis of octahedral tilt and polarization across a domain wall in a BFO film [Borisevich 2010] and polarisation and electric fields across the interfaces of a BFO thin film [Chang 2011] have also been reported. In the present study, atomic resolution high angle annular dark field (HAADF) imaging together with spectroscopy in scanning transmission electron microscope (STEM) is employed to investigate a series of BFO ceramic co-doped with Nd and Ti as

part of the work with Kalantari and coworkers and hopefully to give a direct insight into the properties of defects in nanostructure and their impact on the properties of BFO and eventually give an explanation for the decrease of Curie temperature nonlinearly with the increase of doping level reported by Kalantari *et al.* [Kalantari 2011].

References:

http://www.murata.com/products/capacitor/design/faq/mlcc/property/06_more.html

Anderson P. W., **(1959)** New approach to the theory of superexchange interactions, Phys. Rev. **115**, 2-13.

Bai F. *et al.*, **(2005)** Destruction of spin cycloid in $(111)_c$-oriented $BiFeO_3$ thin films by epitaxial constraint: Enhanced polarization and release of latent magnetization, Appl. Phys. Lett.**86**, 032511.

Borisevich A. Y., Ovchinnikov O. S., Chang, H. J., Oxley, M. P., Yu P., Seidel J, Eliseev E. A., Morozovska AN., Ramesh R., Pennycook S. J., Kalinin S. V., **(2010)** Mapping Octahedral Tilts and Polarization Across a Domain Wall in BiFeO3 from Z-Contrast Scanning Transmission Electron Microscopy Image Atomic Column Shape Analysis, Acsnano **4**(10), 6071.

Borisevich A. Y., Eliseev E. A., Morozovska A. N., Cheng C. J., Lin J. Y., Chu Y. H., Kan D , Takeuchi I., Nagarajan V., Kalinin S. V., **(2012)** Atomic-scale evolution of modulated phases at the ferroelectric-antiferroelectric morphotropic phase boundary controlled by flexoelectric interaction, Nat. Commun. **3,** 775.

Cui Y. F., Zhao Y. G., Luo L. B., Yang J. J., Chang H., Zhu M. H., Xie D., Ren T. L., **(2010)** Dielectric, magnetic, and magnetoelectric properties of La and Ti codoped $BiFeO_3$, Appl. Phys. Lett., **97,** 222904.

Dzyaloshinsky I., **(1958)** A thermodynamic theory of "weak" ferromagnetism of antiferromagnetics, J. Phys. Chem. Solids Pergamon Press. Vol. **4**, 241-255.

Ederer C. and Spaldin N. A., **(2005)** Weak ferromagnetism and magnetoelectric coupling in bismuth ferrite, Phys. Rev. B **71**, 060401(R).

Fiebig M., **(2005)**, Revival of the magnetoelectric effect, J. Phys. D: Appl. Phys. **38**, 123-152.

Hatt A. J. and Spaldin N.A., **(2010)** Strain-induced isosymmetric phase transition in $BiFeO_3$, Phys. Rev. B **81**, 054109.

Hill N. A., **(2000)** Why are there so few magnetic ferroelectrics?, J. Phs. Chem. B, **104**, 6694-6709.

Holcomb M. B., Martin L. W., Scholl A., He Q., Yu P., Yang C. H., Yang S. Y., Glans P. A., Valvidares M., Huijben M., Kortright J. B., Guo J., Chu Y. H., Ramesh R., **(2010)** Probing the evolution of antiferromagnetism in multiferroics, Phys. Rev. B **81**, 134406.

Hu Z., Li M. Y., Yu B. F., Pei L., Liu J., Wang J., Zhao X. Z., **(2009)**, Enhanced multiferroic properties of BiFeO3 thin films by Nd and high-valence Mo co-doping, J. Phys. D: Appl. Phys. **42**, 185010.

Jiang A. Q., Wang C., Jin K. J., Liu X. B., Scott J. F., Hwang C. S., Tang T. A., Bin LuH., Yang G. Z., **(2011)** A resistive memory in semiconducting BiFeO3 thin-film capacitors, Adv. Mater. **23**, 1277-1281.

Kadomtseva A. M., Popov Yu. F., Vorob'ev G. P., and Zvezdin A. K, **(1995)** Spin-density-wave and field-induced phase-transitions in magnetoelectric antiferromagnets, Physica B **211**, 327-330.

Kalantari K., Sterianou I., Karimi S., Ferrarelli, M. C., Miao S., Sinclair D. C., Reaney I. M., **(2011)** Ti-doping to reduce conductivity in $Bi_{0.85}Nd_{0.15}FeO_3$ ceramics, Adv. Func. Mater. **21**, 3737-3743.

Kan D., Palova L., Anbusathaiah V., Cheng C. J., Fujino S., Nagarajan V., Rabe K. M., Takeuchi I., **(2010)** Universal behavior and electric-field-induced structural transition in rare-earth-substituted $BiFeO_3$, Adv. Func. Mater., **20,** 1108.

Ok K. M., Chi E. O., and Halasyamani P. S., **(2006)** Bulk characterization methods for non-centrosymmetric materials: second-harmonic generation, piezoelectricity, pyroelectricity, and ferroelectricity, Chem. Soc. Rev. **35**, 710–717.

Karimi S., Reaney I. M., Levin I. and Sterianou I., **(2009)** Nd-doped $BiFeO_3$ ceramics with antipolar order, Appl. Phys. Lett. **94,** 112903.

Katsufuji T., Mori S. , Masaki M., Moritomo Y., Yamamoto N., Takagi H., **(2001)** Dielectric and magnetic anomalies and spin frustration in hexagonal RMnO3 (R = Y, Yb, and Lu), Phys. Rew. B **64**,104419.

Kimura T., Kawamoto S., Yamada I., Azuma M., Takano M., Tokura Y., **(2003)** Magnetocapacitance effect in multiferroic $BiMnO_3$, Phys. Rev. B **67**, 180401.

Kiselev S. V., Ozerov R.P., and Zhdanov G. S., **(1963)**, Sov. Phys. Dokl. **7,** 742-4.

Lazenka V. V., Zhang G., Vanacken J., Makoed I. I., Ravinski A. F. and Moshchalkov V. V., **(2012)** Structural transformation andmagnetoelectric behaviour in $Bi_{1-x}Gd_xFeO_3$ multiferroics, J. Phys. D: Appl. Phys., **45,** 125002.

Lebeugle D., Colson D., Forget A., Viret M., Bataille A. M., Gukasov A., **(2008)** Electric-field-induced spin flop in $BiFeO_3$ single crystal at room temperature, Phys. Rev. Lett. **100**(22), 227602.

Levin I., Karimi S., Provenzano V., Dennis C. L., Wu H., Comyn T. P., Stevenson T. J., Smith, R. I., Reaney I. M., **(2010)** Reorientation of magnetic dipoles at the antiferroelectric-paraelectric phase transition of $Bi_{1-x}Nd_xFeO_3$ ($0.15 <= x <= 0.25$), Phys. Rev. B., **81,** (2), 020103.

Moriya T., **(1960)** Anisotropic Superexchange Interaction and Weak Ferromagnetism, Phys. Rev. **120**, 91.

Neaton J. B., Ederer C., Waghmare U. V., Spaldin N. A., Rabe K. M., **(2005)** First-principles study of spontaneous polarization in multiferroic BiFeO3, Phys. Rev. B **71**, 014113.

Popov Yu. F., Kadomteseva A. M, Drotov S. S., Belov D. V., Vorob'ev, G. P., Makhov P. N., and Zvezdin A. K., **(2001)**, Features of the magnetoelectric properties of $BiFeO_3$ in high magnetic fields, Low Temp. Phys. **27**, 478.

Popov Yu. F., Zvezdin A. K., Vorob'ev G.P., Kadomtseva A. M., Murashev V. A., and Rakov D. N., (1993) Linear magnetoelectric effect and phase transitions in bismuth ferrite, $BiFeO_3$, JETP Lett. 57, 69.

Schmid H., **(1994)** Multi-ferroic magnetoelectrics, Ferroelectrics **162**, 665-685.

Schmid H., **(2008)**, Some symmetry aspects of ferroics and single phase multiferroics, J. Phys.: Condens. Matter **20**, 434201.

Sosnowska I., Peterlinneumaier T., Steichele E., **(1982)** Spiral magnetic-ordering in bismuth ferrite, J. Phys. C: Solid State Phys. **15 (23)**, 4835-4846.

Sosnowska I., Loewenhaupt M., David W., Ibberson R. M., **(1992)** Investigation of the unusual magnetic spiral arrangement in $BiFeO_3$, Physica B - Condensed Matter, **180**, 117–118.

Stoner, E. C., **(1933)** Atomic moments in ferromagnetic metals and alloys with non-ferromagnetic elements.Philos. Mag. **15**, 1080.

Tabarez-Munoz C., Rivera J. P., Bezinges A., Monnier A., Schmid H., **(1985)**, Measurement of the quadratic magnetoelectric effect on single crystalline $BiFeO_3$, Jpn. J. Appl. Phys **24**, 1051–1053.

Teague J. R., Gerson R and James W. J., **(1970)**, Solid State Commun. **8**, 1973-74.

Wang J., Neaton J. B., Zheng H., Nagarajan V., Ogale S. B., Liu B., Viehland D., Vaithyanathan V., Schlom D. G., Waghmare U. V., Spaldin N. A., Rabe K. M., Wuttig M., Ramesh R., **(2003)** Epitaxial $BiFeO_3$ Multiferroic Thin Film Heterostructures, Science **299**, 1719.

Yu B.F., Li M., Wang J., Pei L., Guo D., Zhao X., **(2008)** Effects of ion doping at different sites on electrical properties of multiferroic $BiFeO_3$ ceramics, J. Phys. D: Appl. Phys. **41** 185401.

Yuan G.L., Or SW, **(2006)** Multiferroicity in polarized single-phase $Bi_{0.875}Sm_{0.125}FeO_3$ ceramics, J Appl Phys **100**, 024109.

Yuan G. L., Or SW, **(2006)** Structural transformation and ferroelectromagnetic behavior in single-phase $Bi_{1-x}Nd_xFeO_3$ multiferroic ceramics, Appl. Phys. Lett. **89**, 052905.

Zalesskii A., Zvezdin A., Frolov A., and Bush A., **(2000)** Fe-57 NMR study of a spatially modulated magnetic structure in $BiFeO_3$, JETP Lett. **71 (11)**, 465-468.

Zavaliche F., Yang S. Y., Zhao T., Chu Y. H., Cruz M. P., Eom C. B. and Ramesh R., **(2006)** Multiferroic $BiFeO_3$ films: domain structure and polarization dynamics, Phase Transit. **79** (20), 991-1017.

Zhang J. X., He Q., Trassin M., Luo W., Yi D., Rossell M. D., Yu P., You L., Wang C.H., Kuo C. Y., Heron J. T., Hu Z., Zeches R. J., Lin H. J., Tanaka A., Chen C. T., Tjeng L. H., Chu Y. H., and Ramesh R., **(2011)** Microscopic origin of the giant ferroelectric polarization in tetragonal-like $BiFeO_3$, Phys. Rev. Lett. **107,** 147602.

Chapter 2 Instrumentation and Sample Preparation

Since the invention of the transmission electron microscope (TEM) in the 1930s, the resolution of the TEM was limited by spherical and chromatic aberrations to about d=100λ (λ is the wavelength of electrons) for about 70 years. The motivation to realise ultrahigh resolution TEM has been driven by the desire to resolve individual atomic column spacings in a variety of crystal orientations, and the development of quantitative image analysis methods where the precision of measurement is limited by the resolution [Nellist 1998]. Non-periodic atomic structures in materials - such as interfaces, dislocations and other defects, which play important roles in the properties of materials – can also only be visualized by means of electron microscopes with atomic resolution [Rose 2005]. With the development of aberration correctors and computer controlled lenses, TEM has become an even more powerful analytical tool which enables studies in condensed-matter physics and materials science to be performed at atomic resolution. New aberration corrected scanning TEMs (STEMs) equipped with high-resolution electron-energy-loss (EEL) spectrometers have made possible not only the atomic scale analysis of the structure, but also of the elemental composition and chemical bonding. Since this chapter serves to outline the principles and practice concerning the instrumentation and sample preparation for the whole thesis, I will introduce some basic background knowledge of TEM/STEM and techniques used for our work. First of all, in section 2.1, I will give a brief overview of the two instruments used in this work – the FEI Tecnai T20 TEM and the Nion UltraSTEM 100 (SuperSTEM2). After this, the properties of electromagnetic lens and their related principal aberrations are discussed. Naturally this discussion will lead to the correlation between these aberrations and image resolution. The use of Ronchigrams will be described in this section as an effective way to diagnose spherical aberration and the other low order aberrations, which are the main limitation on the resolution achievable in STEM. The following section 2.2 will mainly focus on the imaging techniques, which have been used through the experiments, including diffraction-contrast bright field (BF) and dark field (DF) imaging in TEM, including selected area diffraction, together with high angle annular dark field (HAADF) and BF imaging in atomic-resolution STEM. Section 2.3 is an overview of

EEL spectroscopy. In this section, a brief introduction of beam-specimen interactions will be described including a discussion of elastic and inelastic scattering, which serves as a basic background for this whole section. As the spectrometer is an essential tool to record an EEL spectrum (EELS) for chemical analysis, therefore, the principal features and construction of the EEL spectrometer are outlined. Once good quality spectra are recorded, useful information like elemental distribution and chemical bonding can be extracted, therefore further details of EEL spectra and spectrum imaging are given, including some details of the processing required to extract quantitative data from spectra and spectrum images. Finally, some details of sample preparation are described in section 2.4.

2.1 Overview of The Microscopes Used in This Work

Conventional characterisation of samples was performed using a conventional FEI Tecnai T20 transmission electron microscope, prior to any scanning TEM investigations. The FEI Tecnai T20 at the University of Glasgow is a relatively modern type of conventional TEM (CTEM) without scanning TEM (STEM) capability. The major difference between CTEM and STEM is that CTEM is a wide-beam technique, in which a close-to-parallel electron beam is applied to the whole area of interest and the image is collected in parallel, formed by the objective lens after the thin specimen. In contrast to this, STEM uses a fine focused beam, to address small areas of the sample in series as the probe is scanned across the specimen in a raster pattern to form a pixellated image. Image resolution in CTEM is mainly determined by the imperfections or aberrations in the objective lens, whilst the resolution of scanned image in STEM is determined mostly by the beam profile generated by the probe-forming lens(es), which is also limited by aberrations.

2.1.1 The FEI Tecnai T20

A schematic structure of FEI Tecnai T20 TEM in Glasgow is illustrated in Figure 2.1. A principal ray diagram corresponding to some main components to form a bright field image is shown in Figure 2.2. This FEI Tecnai T20, operated at 200 keV, is equipped with a thermionic source - LaB_6 filament - to produce electrons when heated. Compared with tungsten filaments, which are also frequently fitted to conventional TEMs, LaB_6 filaments gives much higher current density than tungsten. The brightness

is typically 10 times that of tungsten filaments but 1000 of times less than that of field emission sources. Increased coherency and longer life are other advantages of LaB_6 over tungsten filaments [Williams & Carter 1996]. The electrons emitted from the filament will be focused into a cross-over acting as the electron source for the optics of the microscope. Following the electron source is the illumination system which consists of two condenser lenses (C1, C2) and a set of condenser apertures beneath the C2 lens. The first lens, C1, is used to form a demagnified image of the electron source and thus the spot size. The C2 lens determines the illumination mode of the beam to be parallel or convergent on the sample by changing C2 to be (over) under-focused or focused and how strongly the beam is focused onto the specimen. As a consequence it varies the intensity of the beam on the viewing screen. Figure 2.2 shows a principal ray diagram of how a parallel beam is formed by the condenser lenses and eventually the formation of a bright field image. Further choice of the illumination conditions is provided by the aperture strip, which lies below the C2 lens. Selection of a smaller aperture provides a beam with higher spatial coherence but with decreased current density at the sample.

The magnification system of the microscope consists of a set of five lenses and two sets of apertures: the objective, diffraction, intermediate, projector1 and projector2 lenses and objective and selected-area apertures. In this Tecnai T20, the so-called "Supertwin" objective lens is deployed, which gives the second highest resolution (C_s=1.2mm) of the three objective lenses available from FEI and gives a compromise between resolution and allowing enough space for tilting the specimen (about ±40/30° (α/β) is available in the lens for a standard FEI double tilt holder). The setting of the twin objective lens also determines the optical illumination mode to be microprobe (parallel illumination) or nanoprobe (convergence beam). The "Supertwin" objective lens will form a diffraction pattern at the back focal plane or an inverted initial image at the first intermediate image plane (see Figure 2.2). Before the lower objective lens, an objective aperture mechanism is installed close to the back focal plane of the objective lens allowing the selection of a variety of apertures in order to control the image contrast. After the lower objective lens, a selected-area aperture mechanism is installed at the first intermediate image plane formed by the objective lens, and a diffraction lens is inserted between the selected area aperture and the intermediate lens to image the diffraction pattern and to enable the magnification to be varied. The intermediate lens after the

diffraction lens is for magnifying the first intermediate image, which is formed just in front of this lens, or the first diffraction pattern, which is formed in the back focal plane of the objective lens. Following the intermediate lens are the two projector lenses which are used to magnify the second intermediate image or the diffraction pattern formed by the intermediate lens, and project this onto the viewing screen or camera system. Within the magnification system, the objective lens (for focusing the image) and the diffraction lens (for focusing the diffraction pattern) are the only lenses that are controlled directly by the operator. The rest of the individual lenses are not directly controllable by the operator, but instead there are a number of different pre-programmed magnification settings for each image and diffraction mode.

In order to get a high acquisition rate of images and diffraction patterns, a SIS Megaview III CCD camera is installed at the 35mm camera port, and also provides a wide field of view ideal for low magnification imaging or imaging of low camera length diffraction pattern. With this camera, areas of suitable crystallographic orientation for high resolution STEM (HRSTEM) studies were recorded with a wide range of magnifications from high magnifications of >100 kx of the precise areas of interest, all the way down to ~100 x to show approximately the locations of the areas of interest on the whole sample. These micrographs acted like a road map and enabled us to find the areas of interest easily in SuperSTEM2, since SuperSTEM2 is ideally suited for high magnification, high resolution studies, and not so convenient for searching at low magnifications for areas of interest. Below the viewing screen, a Gatan Image Filter (GIF) was installed. This allows energy-filtered TEM (EFTEM) to be performed, which is useful for larger area chemical mapping, and spot analysis by EELS. These capabilities were, however, not extensively used in the present work since the principal features of interest were on the atomic scale and below the resolution of conventional EFTEM imaging.

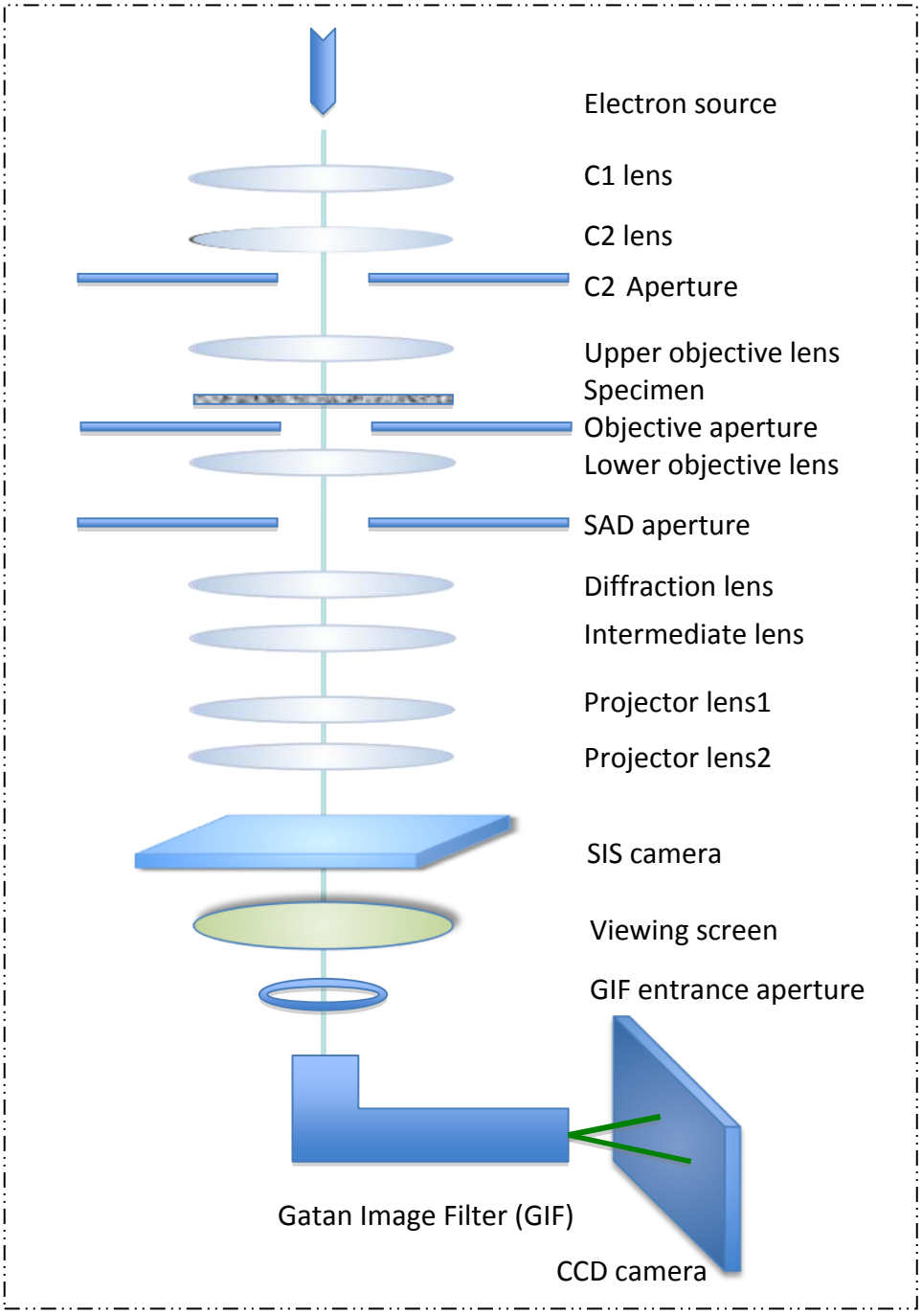

Figure 2.1. *A schematic diagram of FEI Tecnai T20 column consisting of illumination system (electron source, C1, C2/ C2 aperture), magnification system(objective lens, diffraction lens, intermediate lens and projector lenses, and objective, selected area apertures), SIS camera and GIF.*

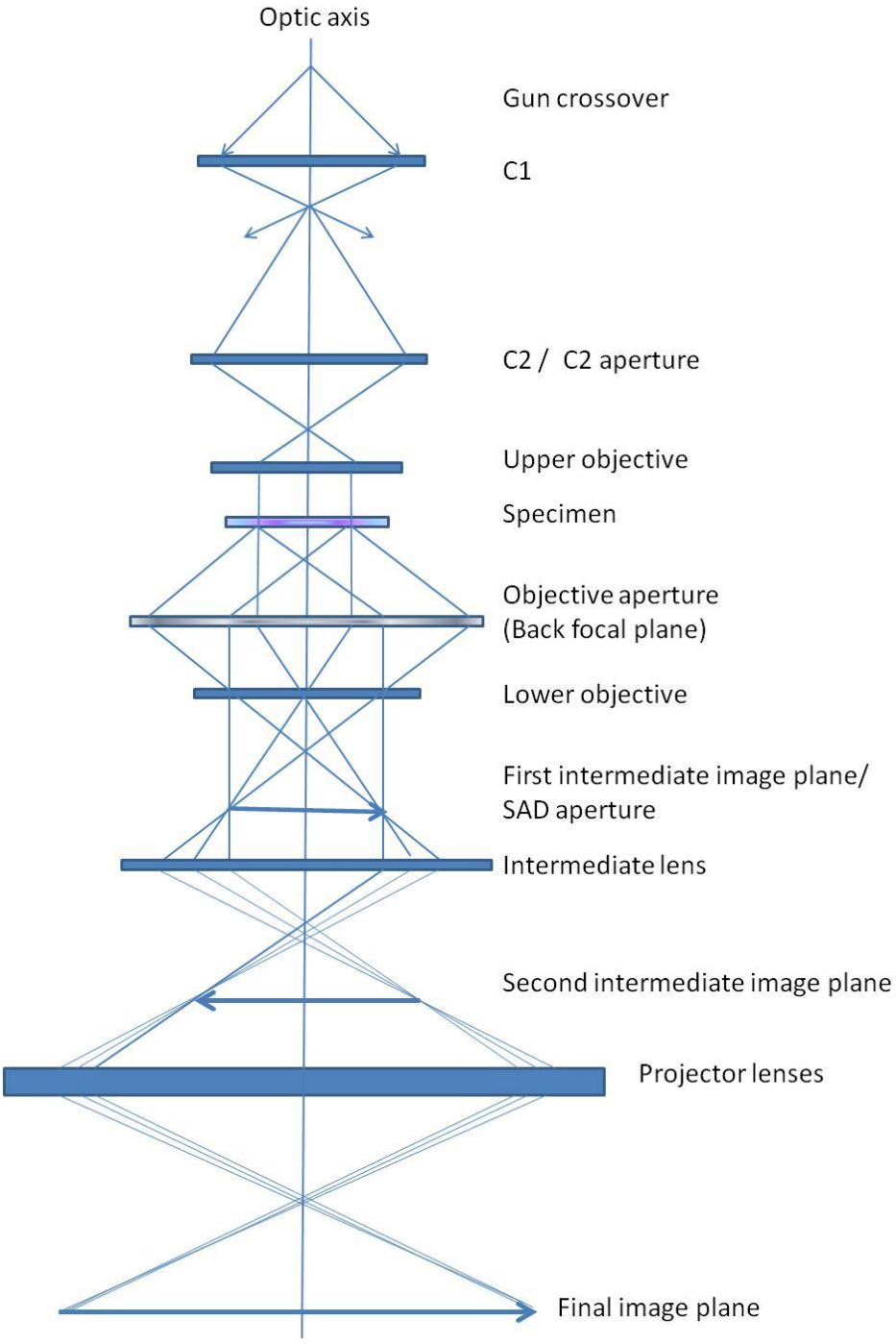

Figure 2.2. *A principal ray diagram of FEI T20 showing the specimen being illuminated by a parallel beam and a bright-field image will be formed as the final image. For forming a selected area diffraction, the objective aperture need to be taken out and the selected area aperture to be inserted. Instead of an image, a diffraction pattern will be formed at the first intermediate image plane. In the end, a selected area diffraction will be projected on to the final image plane.*

2.1.2 SuperSTEM2

SuperSTEM2 is a Nion Ultrastem^{TM} 100 (Nion Inc., Kirkland, WA, USA) – fuller details of this microscope can be found in Krivanek (2008). Here I merely summarise some of the main features of this microscope of particular relevance to the work presented in this thesis. Figure 2.3(a) shows an on-site picture of SuperSTEM2 and a schematic diagram of the column. A corresponding principal ray diagram is shown in Figure 2.3(b). A 100 kV VG (Vacuum Generators – company now defunct) cold field emission gun (CFEG) is used as the electron source with an energy spread of just 0.3 eV FWHM. After the electron source, a three condenser lens system is used, instead of the two lens system in CTEM, in order to give greater flexibility for achieving a variable illumination semi-angle, from <1mrad to >40mrad and an adjustable beam current at the same time. The main column starts with a quadrupole-octupole C_3/C_5 aberration corrector with full correction up to six-fold astigmatism $C_{5,6}$, which is then followed by a quadrupole triplet called the quadrupole lens module (QLM) for coupling the corrector electron-optically to the objective lenses (OL). The OL consists of a lower OL winding module, sample stage/OL polepiece module, and an upper OL winding module. After the OL, a four - round - projector - lens system is installed, which again gives a better flexibility of forming diffraction patterns with a wide range of camera lengths, and CTEM images. In order to collect signals effectively, a complicated detector module is placed after the projector system including: a high-angle annular dark-field (HAADF) detector, a pneumatically controlled beam stop that can be inserted when recording diffraction patterns, a medium angle annular dark-field (MAADF) detector, a bright field (BF) detector, a quadrupole-octupole coupling module (QOCM) for optimised coupling of inelastically scattered electrons into the electron energy loss spectrometer, a fast read-out CCD camera which is retractable and fibre-optically coupled, and finally a Gatan Enfina electron energy-loss spectrometer.

In addition to the modular design that enhances the flexibility of the instrument, other advantages of this instrument include:

1) Each module of the Nion column has integral double μ-metal magnetic shielding which reduces the sensitivity of the whole system to stray magnetic field and localized AC fields.

2) All the round lenses used in SuperSTEM2 have double windings which means lenses are supplied by two independent power supplies so that the power dissipation and thus internal heating is held constant at all magnetic excitation settings, thus stabilises the thermal drift that could otherwise affect microscope stability for tens of minutes after any change of lens settings.

3) The QOCM before the Gatan Enfina EEL spectrometer overcomes the known limitations of the Gatan Enfina such as no electrically adjustable second-order spectrum aberration correction and no third-order aberration adjustment or correction, and therefore significantly improves the quality of the EELS data.

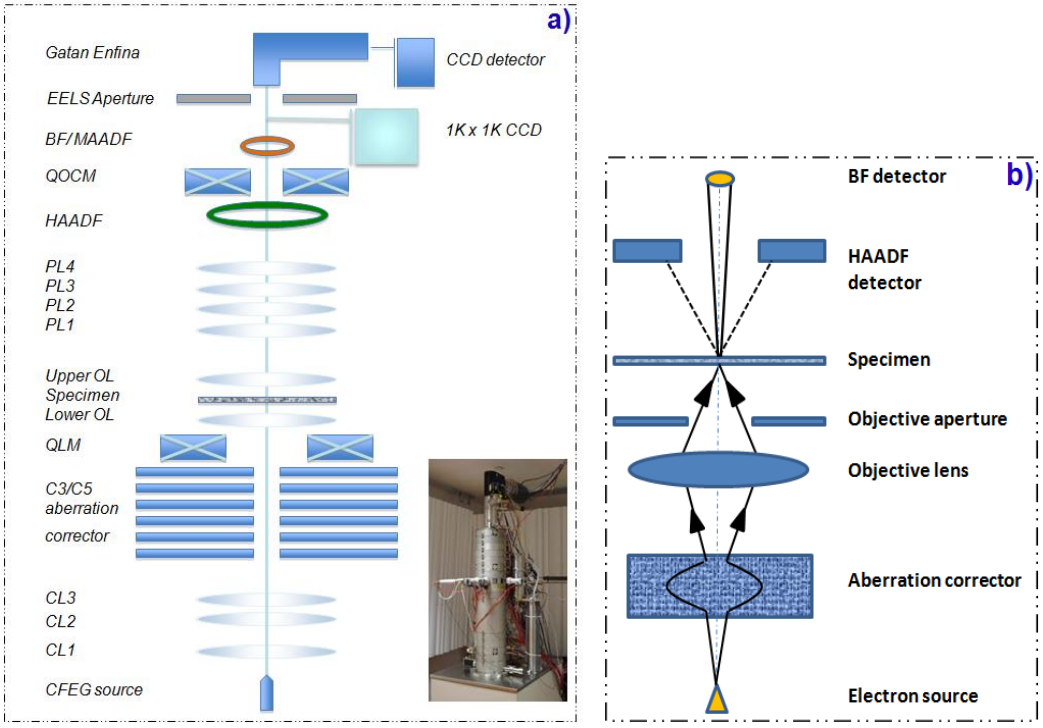

Figure 2.3. *a) A schematic diagram of main components of the column of Nion UltraSTEM 100 with an on-site picture of SuperSTEM2 (inset). The cold FEG emitter operated at 100KV with 0.3 eV energy spread; C_5 Nion QO corrector with full correction up to six-fold astigmatism $C_{5,6}$; Flexible post-specimen optics gives the advantage of large EELS collection angles and flexible imaging detector setup; QOCM couples the inelastically scattered electrons into Enfina EELS spectrometer and corrects the higher order aberrations of the spectrometer. b) A principal ray diagram of SuperSTEM2 showing electrons are formed into a fine probe and is focused on the specimen after the aberration corrector.*

4) Ultrastable x, y, z sample stage with multi-holder in-vacuum magazine for convenient loading and sample exchange.
5) The construction of the whole column gives a resolution in the image controlled by the size of the probe formed by the pre-specimen lenses, and only limited by their aberrations and the aperture. In view of the sub-Ångström probe size given by this, the spatial resolution for EELS mapping is not limited by probe size, but by the physics of the EELS excitation itself, and the details of the collection angle used at the spectrometer only.

In summary, the design of the SuperSTEM2 with an integrated aberration corrector has greatly improved the image resolution to routinely sub-Ångström scales and increased the current available in a given-sized atomic scale probe by about 10 times, compared to one without aberration corrector. With this dedicated design, atomic-resolution imaging, together with elemental mapping from EELS is routinely achievable.

2.1.3 Electron lenses and aberrations

As has been made clear above, both microscopes used many electron lenses to control the path of the electrons. Using electron lenses is based on the concept that electrons can either be deflected by an electric field due to their electrostatic charge or deflected by an applied magnetic field as the moving electron beam can be treated as an electric current in a wire. Taking the advantages of these characters, two types of electron lenses – either electrostatic or electromagnetic can be used to focus the electrons in an analogous manner to the convex lens of light optics. In modern electron microscopes, electromagnetic lenses are preferred since this type of lenses does not require high-voltage insulation and have lower aberrations and better stability than electrostatic lenses, which were used in some early electron microscopes [Egerton 2005].

2.1.3.1 Electromagnetic lenses

Electromagnetic lenses are normally composed of polepieces. A schematic section of a polepiece is shown in Figure 2.4. The polepiece is cylindering symmetrically formed from magnetic alloy (called magnetic circuit) that has a hole drilled through it (called the bore) and wound coils (usually made of copper) surrounding the polepiece, through which a current is passed, thus generating a magnetic

field in the magnetic circuit. Where the circuit is interrupted (the gap) the magnetic field goes out into the vacuum thus the bore of the polepiece and creates the lens field for focusing the electron beam. The strength of the magnetic field and thus the lens field is proportional to the current passing through the lens coils. A water-cooling system is an essential part to remove the excess heat from the electrical resistance of the windings which would otherwise damage them and the microscope. When an electron with charge e enters a magnetic field it will experience a Lorentz force **F**:

$$\mathbf{F} = -e\,(\boldsymbol{\upsilon} \times \mathbf{B}) \qquad (2.1)$$

where $\boldsymbol{\upsilon}$ is the electron velocity and **B** is the magnetic field strength. The direction of the force is determined by the direction of both $\boldsymbol{\upsilon}$ and **B** and is perpendicular to both of them. The magnitude of **F** is given by $F = e\upsilon B\sin(\alpha)$, where α is the angle between $\boldsymbol{\upsilon}$ and **B** at any instant. The field **B** changes continuously along the bore, and so the force **F** varies as the electron passes through the field. Electrons passing through the lens along the optic axis will experience no force since α is zero, and off-axial electrons will spiral along a helical trajectory about the optic axis with diminishing radius. This can be easily understood by considering the magnetic field **B** can be separated into two components: axial and radial. The major effect of the radial component to the off-axis electrons would be spherical aberration, which will be discussed in the following section. The strength of the magnetic field in the lens controls the path of the electrons and, therefore, the focal length of the lens. The stronger the magnetic field, the shorter the focal length of the lens is. For high-resolution, it is essential to keep the focal length of the objective lens short to minimise the spherical aberration, which will be discussed in the following section.

Other types of lenses that may be used in a electron microscope are multipole lenses like quadrupole, hexapole or quadrupole-octupole lenses. The most important difference between multipole lenses and rotationally symmetric (round) lenses is that in the former the field is mostly perpendicular to the beam while the latter produces a field largely parallel to the beam. Multipole lenses are mainly used to correct or compensate for aberrations induced by the rotationally symmetric electromagnetic lenses (round lens) and parasitic aberrations caused by the imperfections in the manufacture of the lenses.

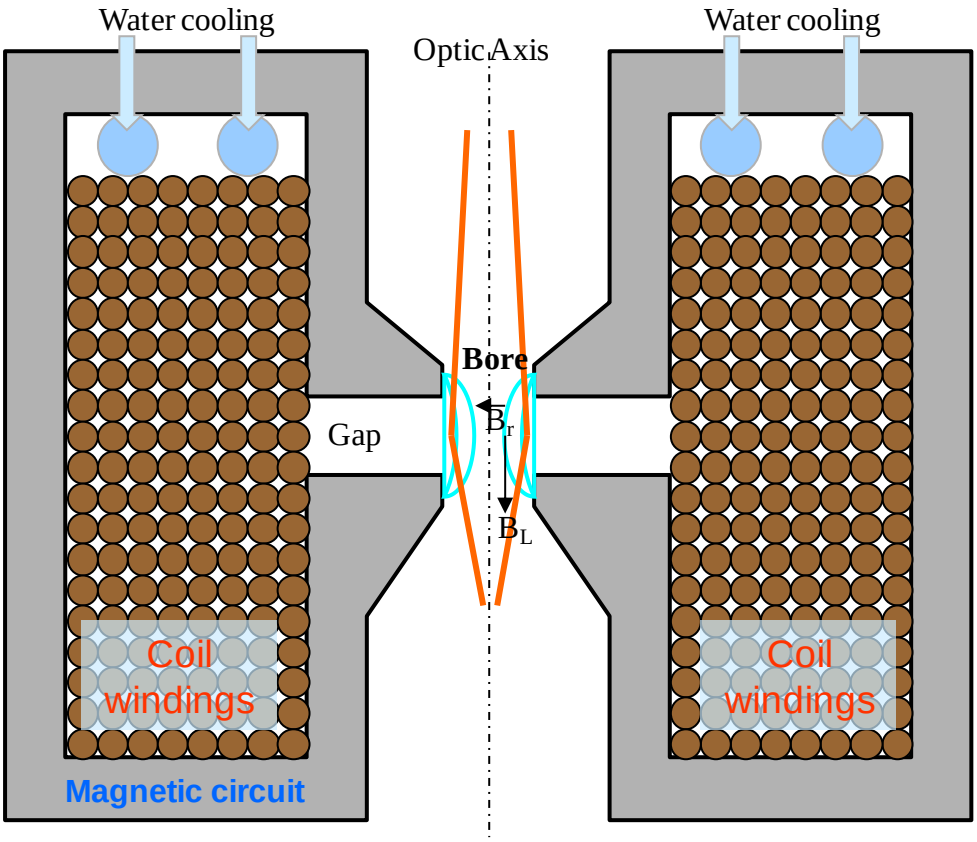

Figure 2.4. *A schematic section of a polepiece showing its structure and two paths of the electron ray due the radial component* $\boldsymbol{B_r}$ *of the magnetic field.*

2.1.3.2 Defects of electromagnetic lenses - aberrations

Due to the nature of round lenses, spherical aberration is unavoidable [Scherzer 1936]. Aberrations from lenses are critical for a microscope as they limit the spatial resolution of the image by transforming point foci to disks of least confusion at given focus values. Aberrations from magnetic lenses can be categorized to geometric/monochromatic aberrations and chromatic aberrations.

2.1.3.2.1 Geometric aberrations

Geometric aberrations include spherical aberration (Cs), axial astigmatism, coma, field curvature and distortions (e.g. pincushion distortion, barrel distortion and spiral distortion). Amongst these aberrations, the most important are spherical aberration, axial astigmatism and coma. **Spherical aberration** as shown in Figure 2.5 is that off-axis rays with larger angle α to the optic axis are not brought to the same focus

point F in the Gaussian image plane as those paraxial rays. Off-axis rays will be displaced radially from the optic axis as they reach the Gaussian image plane. Therefore, a point will be imaged by the lens as a blurred disk. The effect of the spherical aberration can be expressed by the radius of the disk in formula (2.2):

$$r_s \approx C_s \alpha^3 \qquad (2.2)$$

where C_s is known as the coefficient of spherical aberration of the lens. Due to the physical properties of the magnetic field in round lenses, spherical aberration cannot be eliminated through careful design of the lens polepieces. However, it can be minimised by using a strong lens (short focal length) or by using an aperture in the column to limit the maximum angular deviation α to minimize its effect.

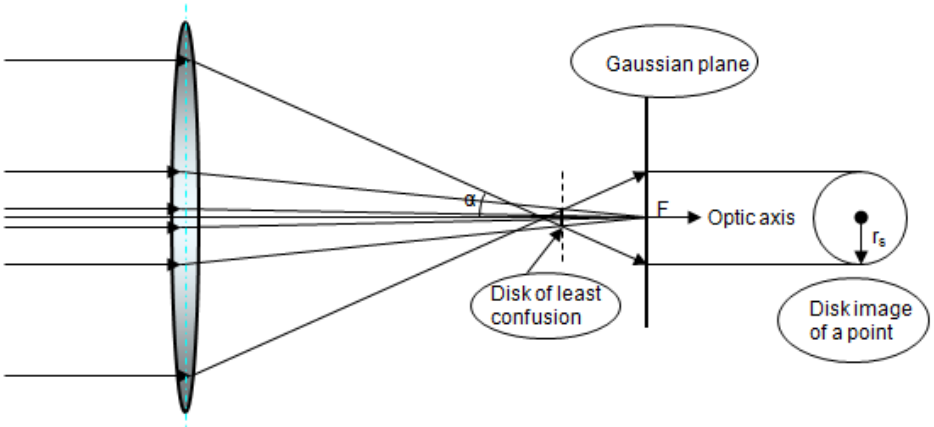

Figure 2.5. *A schematic diagram showing spherical aberration - a point object is imaged as a disk with radius $r_s \approx C_s \alpha^3$ due to spherical aberration that causes the off-axis rays are not focused at the same point F as those paraxial rays.*

Axial astigmatism is caused by one or more of the following reasons: 1) inhomogeneities in the polepiece material of the lens; 2) geometrical defects in the manufacture of the 'cylindrical' bore of the lens; 3) the build-up of contamination on the bore of the pole-piece and on the apertures. These potential "defects" will result in a magnetic field which is no longer axially symmetric. For example, in Figure 2.6, the magnetic field, B_z, is less powerful in the x-direction than in the normal y-direction. In this case, electrons originating from a point object on the optic axis may start at equal angles to the z-axis but those rays travelling in the x-z and y-z planes will be focused at different points, F_x and F_y, along the z-axis, respectively. Due to astigmatism, points will be focused by the lens as ellipses with the long axis always normal to the plane within

which electrons travel rather than disks. The best compromise is achieved at point F, at which the smallest radius disc is found – the disc of least confusion. Axial astigmatism can be corrected by a quadrupole lens which is usually referred to as a stigmator. By using a stigmator, the focal length in the x-z and y-z planes can be made equal thus the two foci F_x and F_y are brought together to a single point.

Coma is related primarily to rays, which originate from an object point slightly off the optic axis. All the rays that travel parallel to the optic axis or through the centre of the lens will still be brought to a point focused on the optic axis but rays which travel through the peripheral field of the lens with an incident angle will be focused at different points (see Figure 2.7). This results in an off-axis image which is comet-shaped. Coma aberration can be avoided by correct alignment of the beam to travel along the optic axis of the objective lens.

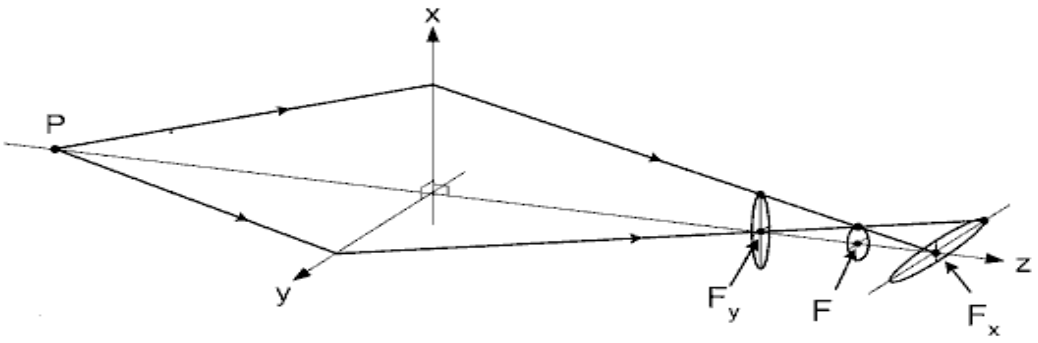

Figure 2.6. *Schematic diagram of axial astigmatism [Egerton 2005]. Rays leaving an axial image point, focused by a lens (with axial astigmatism) into ellipses centred around F_x if they travel in x-z plane or F_y if they travel in y-z plane, with long axis normal to the plane they travel, or into a circle of smallest radius - the disc of least confusion.*

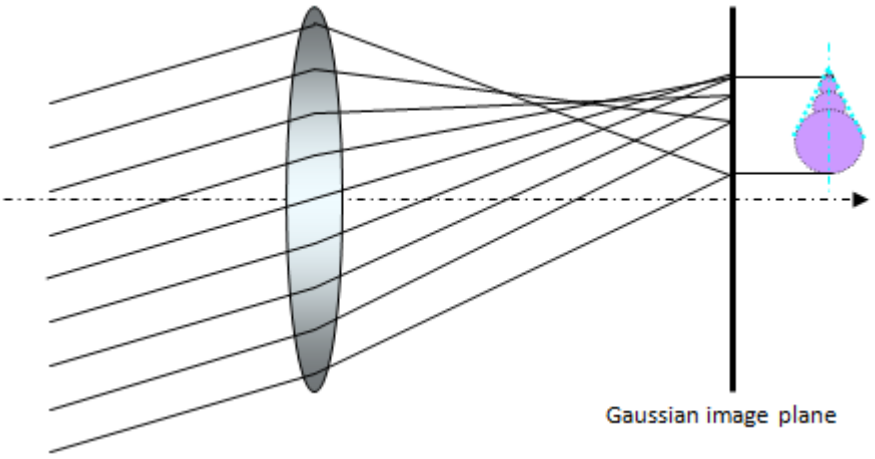

Figure 2.7. *Schematic diagram of coma aberration which causes an off-axis object point imaged as comet shaped. Rays travel through the peripheral field of the lens with an incident angle are focused at different point from those travel parallel to the optic axis or through the centre.*

Considering the wave nature of electrons, all the geometric aberrations can be expressed by the wave aberration function, which is defined as the phase difference between the perfect spherical wavefront and the actual wavefront for a given lens. In practice, the wave aberration function can be expressed in polynomial form by equation (2.3) [Hawkes & Kasper 1996, Krivanek 1999], where α is the convergence angle, ϕ is the azimuthal angle with $\theta_x=\alpha\cos(\phi)$ and $\theta_y=\alpha\sin(\phi)$ and $2\pi/\lambda$ is the incident electron wavevector:

$$\begin{aligned}\chi(\theta_x,\theta_y) = \frac{2\pi}{\lambda}[&C_{1,0}(\theta_x^2+\theta_y^2)/2 + C_{1,2a}(\theta_x^2-\theta_y^2)/2 + C_{1,2b}\theta_x\theta_y + C_{2,1a}\theta_x(\theta_x^2+\theta_y^2)/3 \\ &+ C_{2,1b}\theta_y(\theta_x^2+\theta_y^2)/3 + C_{2,3a}\theta_x(\theta_x^2-3\theta_y^2)/3 + C_{2,3b}\theta_y(3\theta_x^2-\theta_y^2)/3 \\ &+ C_{3,0}(\theta_x^2+\theta_y^2)^2/4 + C_{3,2a}(\theta_x^4-\theta_y^4)/4 + C_{3,2b}\theta_x\theta_y(\theta_x^2+\theta_y^2)/2 \\ &+ C_{3,4a}(\theta_x^4-6\theta_x^2\theta_y^2+\theta_y^2)/4 + C_{3,4b}(\theta_x^3\theta_y-\theta_x\theta_y^3)+\ldots]\end{aligned} \tag{2.3}$$

In equation 2.3, aberration coefficients are denoted by $C_{n,m}$ where C denotes an axial aberration, n is the order of the aberrations and $2\pi/m$ denotes the smallest rotational angle that results in the same phase shift (for $m \geq 1$). Note m=0 is used for cylindrically symmetric aberrations. Moreover, the suffixes a and b refer to 2 mutually orthogonal contributions to the same aberration that arise for all non-cylindrically symmetric aberrations. The $\theta_x^2 + \theta_y^2$ term is equal to α^2 and highlights the rotationally symmetric

nature of the C_1, C_3 and C_5 aberrations. For comparison, table 2.1 shows a list of all of the aberration coefficients up to, and including, fifth order with corresponding conventional names. Please note, there are other conventions in use for the definition of the aberration coefficients in the power series expansion, which were not used in this work [Hawkes 1989, Uhlemann 1998].

Table 2.1 Aberration coefficients and their corresponding conventional names

Aberration Coefficients		Conventional Name	Azimuthal symmetry
C_{01}	C_{01a}	x Image Shift	1-fold
	C_{01b}	y Image Shift	
C_{10}		Defocus	Circular
C_{12}		2-fold Astigmatism	2-fold
C_{21}		Coma	1-fold
C_{23}		3-fold Astigmatism	3-fold
C_{30}		(3^{rd} order) Spherical Aberration	Circular
C_{32}		2-fold Astigmatism of C_s (or 3^{rd} order 2-fold Astigmatism)	2-fold
C_{34}		4-fold Astigmatism of C_s	4-fold
C_{41}		4^{th} order Coma	1-fold
C_{43}		4^{th} order 3-fold Astigmatism	3-fold
C_{45}		5-fold Astigmatism	5-fold
C_{50}		5^{th} order Spherical Aberration	Circular
C_{52}		2-fold Astigmatism of C_5	2-fold
C_{54}		4-fold Astigmatism of C_5	4-fold
C_{56}		6-fold Astigmatism of C_5	6-fold

2.1.3.2.2 Chromatic aberration

Chromatic aberration (see Figure 2.8) arises principally because of the energy spread in the electrons emitted from the electron source (like light with different wavelengths), as well as instability of the gun acceleration voltage and lens current fluctuations. There may also be chromatic aberration effects in the post specimen lenses for electrons that have experienced inelastic interactions with the sample. Due to chromatic aberration, electrons with lower energy will be deflected more strongly by the field, resulting in a higher focusing power and thus a shorter focal length. Consequently, chromatic aberration results in electrons with a range of energies being focused in

different planes. For example, electrons emerging from the specimen with no loss of energy are less strongly focused than those that suffered from energy loss in the specimen. The effect of chromatic aberration on image resolution will be discussed in section 2.1.4.2.

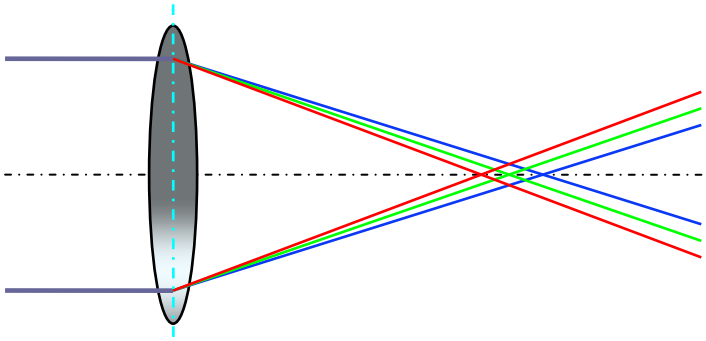

Figure 2.8. *A schematic diagram showing electrons with different energies being focused at different planes due to chromatic aberration.*

2.1.4 Image resolution and aberration correction

Since the invention of the first electron microscope by Knoll and Ruska in 1932, the development of electron microscopes has always been driven by efforts to improve imaging resolution. According to the Rayleigh criterion, which defines the smallest resolvable distance between two points scatterers, resulting a central drop of the signal down to 75% of the maximum signal, the theoretical limit for point-to-point image resolution *d* can be calculated by formula (2.4) at a given wavelength λ and convergence semi-angle α (see Figure 2.9),

$$d_d = 1.22\lambda / \alpha \qquad (2.4)$$

which is also known as diffraction-limited resolution. Thus, the image resolution can be improved by increasing the acceleration voltage and/or by reducing the aperture size. However, there is a knock-on threshold, above which atoms may be displaced from their lattice sites by inelastic interactions with electrons, which limits the useable acceleration voltage for any given material. Reducing the aperture size will eventually increases the diffraction effect, which again will suppress the improvement of resolution [Rose 2005]. Although, in a "perfect" imaging system, the resolution should only be limited by the diffraction, in reality, spherical aberrations and chromatic aberrations are unavoidable to

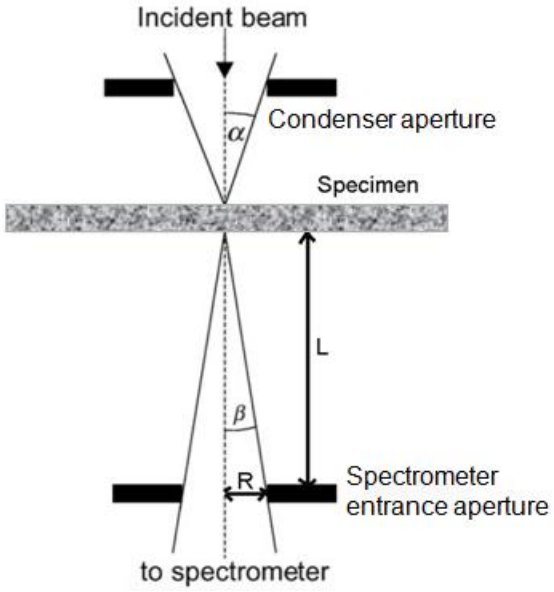

Figure 2.9. *A schematic diagram of a focused beam on the specimen in CTEM showing the definition of convergence semi-angle α, which is determined by the condenser lens and condenser aperture and collection semi-angle β, which is determined by the spectrometer entrance aperture.*

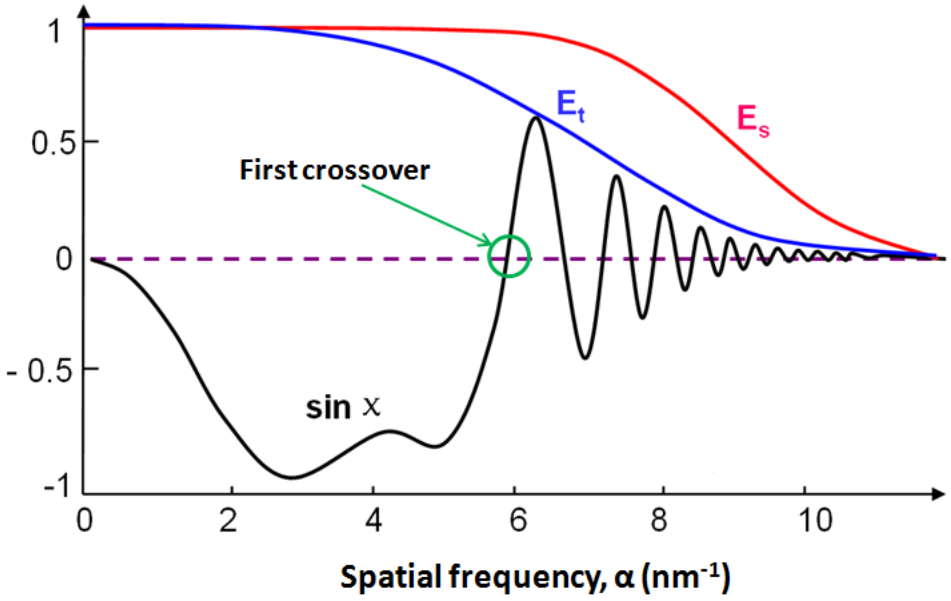

Figure 2.10. *A schematic plot of sinχ(α) versus α showing the contrast transfer as a function of spatial frequency with uncorrected TEM. The first crossover indicating the maximum allowable spatial frequency for intuitive image interpretation. E_s is the envelope of spatial coherence of the source and E_t is the chromatic aberration envelope.*

rotationally symmetric electromagnetic lenses [Scherzer 1936], which put additional limits on the image resolution. Achieving optimum performance of a microscope is a balance between aberrations and diffraction. With simple geometric optics approach (square root of the sum of the squares of each contributor), this balance could be achieved by finding an optimum value of convergence semi-angle α. With a more rigorous wave optical treatment, this balance is essentially guided by the contrast transfer function (CTF), which is applicable for coherent imaging e.g. HRTEM and BF STEM imaging, or by the optical transfer function (OTF) which is applicable for incoherent imaging e.g. HAADF imaging. With coherent imaging, the CTF is defined by $sin\chi(\alpha)$ with $\chi(\alpha)$ defined as the aberration function. A plot of $sin\chi(\alpha)$ against α in Figure 2.10 shows the contrast transfer as a function of spatial frequency within the image [Hall 1953]. It shows maxima whenever the aberration function $\chi(\alpha)$ assumes values of $\pm m\frac{\pi}{2}$ (m is an odd number) and zero contrast when $\chi(\alpha)$ is $\pm n\pi$ (n is integral). Specific frequency components above a certain value can be removed by using an aperture, and to achieve a simple and interpretable image contrast with all spatial frequency components having the same sign, the aperture needs to be placed at the first crossover (first zero contrast point) of CTF at Scherzer defocus. Therefore, the CTF gives an indication of the maximum allowable frequency to ensure intuitive image interpretation. In practice, the oscillations of $\chi(\alpha)$ in CTF are modified by the spatial coherence of the source E_s and by chromatic aberration effects E_t which can be described by an envelope function. The effect of the envelope function is to impose a virtual aperture in the back focal plane of the objective lens resulting in damping of higher spatial frequencies that might normally pass through higher-order windows. This cut-off imposes an ultimate resolution limit on the microscope, which is called the "information limit". In the case of incoherent imaging, as widely used in STEM, the OTF is defined as the Fourier Transform of the STEM probe intensity function. Generally it is a positive, monotonically decaying function but with a doubled spatial frequency range, compared with the CTF for the same lens parameters [Nellist 2011]. This means that the aperture radius can almost be as twice large as that for coherent imaging, meaning that a higher spatial resolution can be readily achieved for incoherent imaging.

2.1.4.1 Spherical aberration limited image resolution

In a STEM, the image resolution is limited by the probe size formed by the pre-specimen lenses of the microscope. In a simple geometric optic approach, there are three factors that contribute to the probe size: the effect of a finite source size (the 'gun'), the aberrations induced by rotationally symmetric lens (the spherical aberration (C_s or C_{n0}) term), and the diffraction limit. Contributions from these factors can be expressed by formula (2.5):

$$d = (d_s^2 + d_d^2 + d_{sph}^2)^{1/2} = [(\frac{4I_{probe}}{\pi^2 B\alpha^2})^2 + (0.61\frac{\lambda}{\alpha})^2 + (A_n C_{n0}\alpha^n)^2]^{\frac{1}{2}} \qquad (2.5)$$

where B is the brightness of the source, α is the convergence semi-angle and λ is the electron wavelength. A_n is a numerical constant, which for the third order case, A_3, is 1/4; as the order of aberration increases it is normally taken as unity. C_{n0} is defined as the spherical aberration coefficient (e.g. for C_{30}). By choosing an appropriate demagnification of the source to set d_s to the required value for a given current I_{probe}, the minimum probe size with an optimum probe angle, α_{opt}, can be obtained. The ultimate probe size is determined by the optimized value of α_{opt}. For a conventional TEM without aberration correction in the STEM mode, this value is typically restricted to the order of 10 mrad due to unavoidable aberrations of the round electron lenses, resulting in the resolution of about 100 times the electron wavelength. With aberration correction, this α_{opt} value could be several times bigger. While the geometric approach suits a larger probe where the source size term dominates, it consistently overestimates the size of the probe and underestimates the size of the optimum convergence semi-angle for high resolution STEM imaging. Nevertheless, it can be taken as a guide on how to optimise performance. A wave-optical treatment can give a more realistic solution by considering more details with variation of these parameters. According to wave-optical theory and based on Scherzer aberration function $\chi(\alpha) = \frac{2\pi}{\lambda}\left(\frac{1}{4}C_s\alpha^4 + \frac{1}{2}\Delta f\alpha^2\right)$ [Scherzer 1949] with maximum allowable phase shift of π/2 across the objective lens, if considering the spherical aberration only up to 3rd order, then the minimum attainable probe size at given optimized α is [Scherzer 1949]:

$$d_3 = 0.43(C_{30}\lambda^3)^{1/4} \quad \text{with} \quad \alpha = \left(\frac{4\lambda}{C_{30}}\right)^{1/4} = 1.41\left(\frac{\lambda}{C_{30}}\right)^{1/4} \tag{2.6}$$

which for 100 kV (λ=3.7pm) and C_{30} = 1.0 mm gives a minimum probe size of 2.0 Å with α_{opt} about 15.5 mrad and for 200 kV (λ = 2.5 pm) with C_{30} = 0.5 mm is 1.2 Å. For the same instrument with C_3-corrector (C_3 fully corrected), the probe size is limited by C_5 which gives

$$d_5 = 0.43(C_{50}\lambda^5)^{1/6} \quad \text{with} \quad \alpha = \left(\frac{4\lambda}{C_{50}}\right)^{1/6} = 1.41\left(\frac{\lambda}{C_{50}}\right)^{1/6} \tag{2.7}$$

For 100 kV and C_5 = 100 mm is 0.87Å with α_{opt} about 32mrad and for 200kV and C_{50} = 5 mm is about 0.38Å. Thus the resolution is improved by a factor of about 2 for 100 kV STEM. With aberration correction, even the resolution at lower accelerating voltages (100 kV) can still be better than that at higher accelerating voltages (at 200 kV) without correction. With spherical aberration correction, there is no need to use very high acceleration voltage or to make a further reduction of the geometrical pole-piece dimensions of objective lenses to reduce the spherical aberration for the improvement of resolution [Haider 1998].

2.1.4.2 Chromatic aberration limited image resolution

Just like spherical aberration, chromatic aberration is another major problem that needs to be tackled in order to improve the resolution of electron microscope especially for lower acceleration voltages because chromatic aberration effects increase as the accelerating voltage decreases. Another benefit of chromatic aberration correction in the post specimen lenses would be for spectrum imaging, which uses inelastically scattered electrons to reveal information about chemical composition of the specimen on the sub-nanometer scale or even atomic scale. Chromatic aberration limited resolution can be defined as [Zach 2009]:

$$d_c = B * \sqrt{\lambda * \frac{\Delta E}{E} * C_c} \tag{2.8}$$

where B is the numerical values of the order of 1, λ is the electron wavelength, E and ΔE are the mean energy and energy width of the primary beam, respectively, and C_c is the chromatic aberration coefficients. Formula (2.8) shows us clearly that resolution could be improved by:

- ✓ increasing the acceleration voltage V which defines λ but not always feasible because of the beam damage effect
- ✓ reducing the chromatic aberration coefficient C_c
- ✓ minimising the energy spread of the electron beam ΔE/E

The use of cold field emission and Schottky electron sources together with the improved stability of high voltage and lens power supplies would reduce the influence of chromatic aberration considerably. A monochromator could be used to reduce the energy-spread ΔE of the incident electron beam to 0.1 eV and an energy filter could also be helpful to reduce the beam broadening after the beam being scattered by the specimen. However, chromatic aberration is not as important as spherical aberration with STEM HAADF imaging at high resolution. This is because, in STEM, chromatic aberration puts an overall weakening of contrast transfer without actually cutting any spatial frequencies out. [Nellist 1998, Dellby 2001]. The phase difference due to chromatic aberration is independent of defocus changes, which are used to compensate for C_s. Thus, the effects of chromatic aberration become less important and negligible than spherical aberration. But chromatic aberration correction will still be very useful for improving the spatial resolution for electron energy loss spectrum analysis and becomes more important for low voltage STEM.

2.1.4.3 Diagnosis of spherical aberration – the electron Ronchigram

After Scherzer had realised that spherical and chromatic aberrations are unavoidable for round lenses, he proposed non-rotationally symmetric multipole lenses [Scherzer 1947] to correct chromatic and spherical aberrations. But his attempts at a practical realisation of this were unsuccessful due to the extraordinary complexity of aligning the instrument by hand including the corrector system, together with electrical instabilities in the power supplies. This use of the electron Ronchigram together with new computer technology have provided a convenient route for the diagnosis of spherical aberration, and thus have made aligning a STEM a practical proposition [Dellby 2001, Krivanek 1999]. The electron Ronchigram is very useful in diagnosis of spherical aberration and optimum objective aperture size.

Figure 2.11 shows a typical electron Ronchigram simulated by computer with an amorphous sample in STEM with spherical aberration present. Similar features are

readily seen experimentally. In the simulation, the specimen was placed at a position giving a small but finite defocus, in order to see the aberrations of the uncorrected lens easily. The very centre of this image is a normal shadow image of the specimen at rather high magnification, known as "sweet spot" as marked by a green circle. The size of the "sweet spot" can be used as a guidance of the optimum objective aperture size to exclude rays distorted by spherical aberration and other uncorrected aberrations whilst maintaining the largest possible probe convergence angle, and thus optimises the probe size. Within this region, the spatial information of the sample is delivered faithfully with no distortion due to spherical aberration. Beyond this region, there are two characteristic rings caused by the spherical aberration from objective lens. The inner one is streaked out in the radial direction, which is called the **ring of infinite radial magnification**. The outer one is a ring formed by high angle rays, where everything is streaked out into a circular pattern and is called the **ring of infinite azimuthal magnification**. Other aberrations might cause the Ronchigram to be not be circularly symmetric, for instance, astigmatism will cause the rings to be elliptical. Therefore, in order to get a good STEM image, the Ronchigram must be as round as possible and the details of the Ronchigram are a powerful and useful guide in optimising lens, stigmator and corrector settings to minimise aberrations. This adjustment may be done by a skilled operator, or automatically, by suitable software.

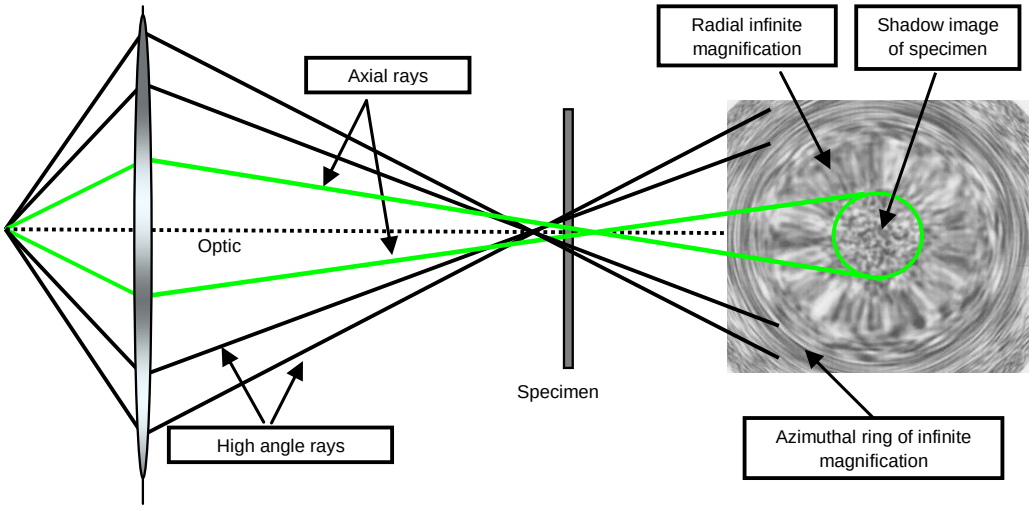

Figure 2.11. *A typical electron Ronchigram with two characteristic rings of infinite magnification appear around the sample shadow image showing spherical aberration.*

2.2 Imaging

2.2.1 Image contrast

For photography, *contrast* is the difference in visual properties that makes an object (or its representation in an image) distinguishable from other objects and the background. Increasing contrast can help to improve the image resolution. With TEM image, contrast is defined as the variation of electron intensities between neighbouring regions. The contrast of BF images in CTEM is dominated by diffraction contrast or phase contrast, depending on the size and location of the objective aperture, and sometimes with mass-thickness contrast present. Contrast from conventional dark field (DF) imaging or medium angle annular dark field imaging (MAADF) in STEM is very similar to that of conventional BF imaging. "Z-contrast" from Rutherford-like scattering is strongly dependent upon the atomic number and is well-known as the principal source of contrast in HAADF images. Contrast from HAADF imaging is therefore more mass-thickness dependent than that from BF, DF and MAADF imaging.

2.2.2 Bright-field and dark-field diffraction contrast imaging – coherent imaging

A bright-field (BF) image is formed by selecting the direct beam (undiffracted electrons) travel through the objective aperture with small angle (5~20 mrad) and a dark-field (DF) image can be formed either by shifting the objective aperture to the selected Bragg-diffraction spot or (preferably) by tilting the incident beam so that one of the diffracted beams is on axis to form the image. The method of tilting the illumination has the advantage that off-axis aberrations are avoided. BF and DF are two common techniques used for imaging with **CTEM**. In contrast to high angle angular dark field (HAADF) imaging with **STEM,** which is an incoherent imaging technique as will be discussed in the following section, BF and DF imaging are coherent. Image contrast for BF and DF images of crystalline materials is dominated by diffraction contrast, at least for thin specimens (less than 100 – 200 nm). Figure 2.12 schematically shows how to form BF and DF images. Generally BF imaging is a quick and useful method for specimen inspection, imaging the size and morphology of nanostructures. But when imaging defects such as dislocations, phase boundaries, precipitates, stacking faults, and

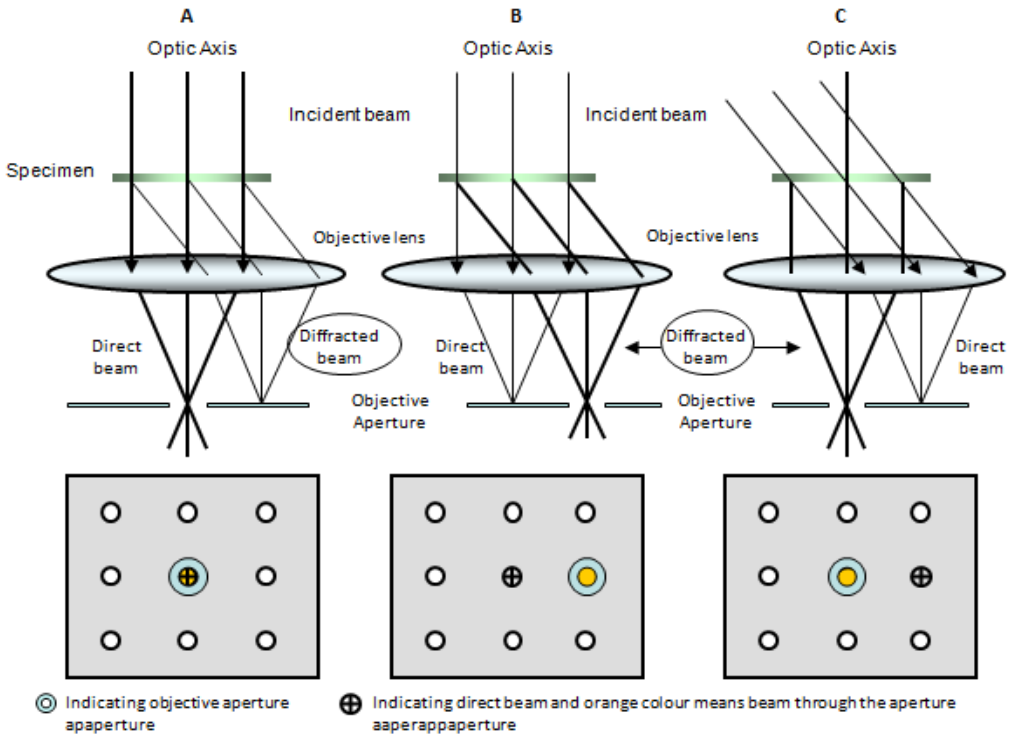

Figure 2.12. *Ray diagrams showing how to form BF and DF images. A) a BF image formed from direct beam. B) a DF image formed from a specific diffracted beam by displacing the objective aperture. C) a DF image formed by tilting the incident beam so that the scattered beam is on axis. The area selected by the objective aperture is shown on the viewing screen below each ray diagram. (Adapted from Williams & Carter 1996).*

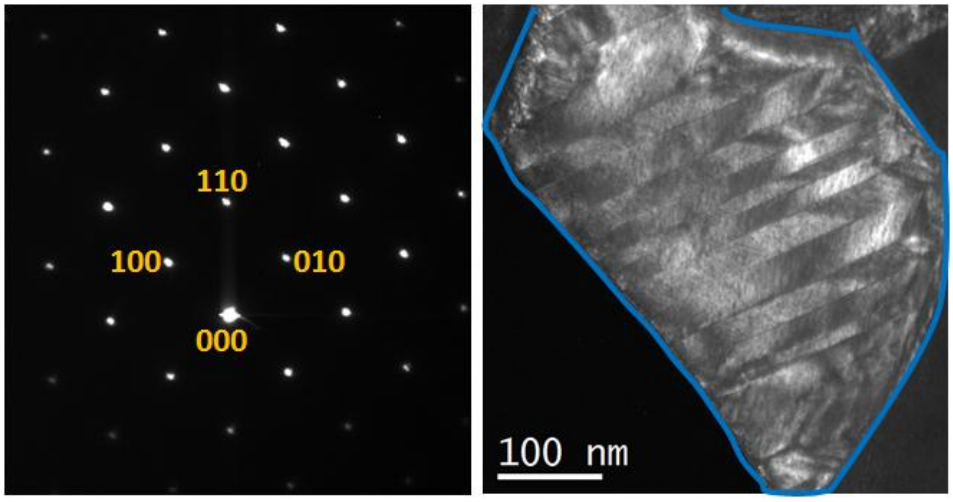

Figure 2.13. *A SAD pattern showing [001] orientation and its related DF image showing the grain boundaries clearly as marked by the light blue line ($BiFeO_3$ co-doped with 10% Nd, 3% Ti).*

defect clusters, DF imaging can often be more useful though sometimes need to be combined with BF imaging. In order to interpret either bright or dark field images, they need to be coupled with crystallographic information from selected-area diffraction (SAD). To form a SAD pattern, a selected area aperture, which is located below the specimen in the first image plane (see Figure 2.2), is inserted to define the area to be investigated, then the condenser lens settings are changed to provide a broad, parallel electron beam to form the diffraction pattern consisting of sharp diffraction spots. By choosing specific diffraction spots in a diffraction pattern for use in the formation of dark field images, specific features in a crystal, or secondary phases with different crystal structures or orientations associated with those diffraction spots can be defined and characterised. Within our study, SAD is essential for choosing grains of interest – which in our case means of specific crystallographic orientations. Figure 2.13 shows a SAD pattern and its related DF image of the grain we studied indicating the grain orientation is [001] along the beam direction.

2.2.3 High angle annular dark field (HAADF) imaging with STEM – incoherent imaging

HAADF images are formed by collecting those electrons (mostly from Rutherford scattered electrons) scattered to high angle with an ADF detector, as proposed by Howie (1979) in STEM. Figure 2.14 schematically shows the relative positions of different detectors, which can be used for imaging. When the inner angle of the HAADF detector exceeds a critical value, normally over 40 mrads, thermal diffuse scattering (TDS) resulting from the thermal lattice vibration (approximately equivalent to Rutherford scattering) will progressively dominate over coherent elastic scattering from the specimen [Hall 1965] and predominantly falls upon HAADF detector. Therefore the HAADF image will not be strongly affected by Bragg diffraction effects. The HAADF image is also referred as a Z-contrast image because of its sensitivity to the variation of the atomic number, which would be approximately proportional to Z^2 for isolated atoms (Rutherford 1911). Considering the screening effect of the orbital electrons, the exponent could be less than 2, depending on the actual value of the inner and outer angles of the detector [Hartel 1996]. For an uncorrected STEM, operated at 100 kV with a semi-illumination angle α of 10 mrad, an inner angle of 60 mrad will give

a good contrast. For SuperSTEM2, a 5th order corrected STEM, with a value of α of 30mrad, it is found that an inner angle of ~100 mrad is suitable and this results in an outer angle of ~185 mrad for this microscope [Craven 2011].

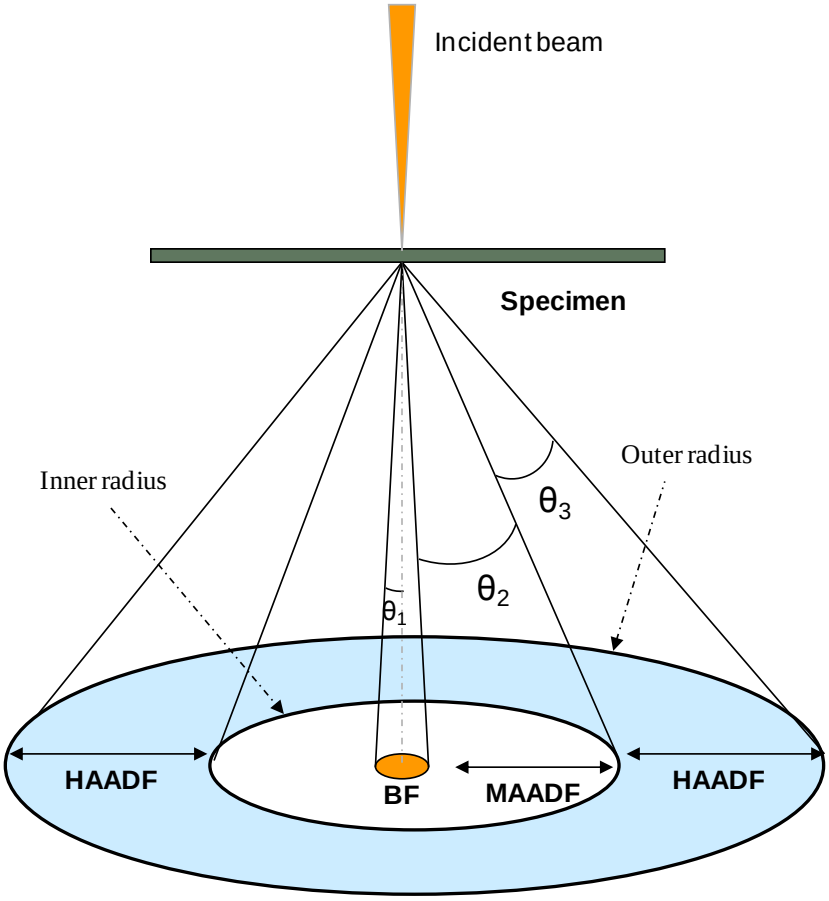

Figure 2.14. *Schematic diagram shows relative positions of different detectors with semi-angles θ_1< 10mrad (BF), 10mrad<θ_2<50mrad (MAADF), θ_3>50mrad (HAADF).*

HAADF imaging has become the most widely used imaging method in STEM. Images with atomic resolution acquired by HAADF detectors in aberration corrected STEM are, in general, more straightforward to interpret than HRTEM images due to the nature of incoherent imaging, which gives no contrast reversals over a wide range of spatial frequencies, as discussed in section 2.1.4. Contrast reversals may happen with HRTEM due to the specimen thickness or the objective-lens defocus [Pennycook 1990]. In the HAADF image, bright contrast generally indicates the presence of atoms or atom columns. However, HAADF imaging alone cannot uniquely identify atoms by just using the change of contrast in the image, except in some very well-defined cases [Allen 2008,

Krivanek 2010]. In general, to be able to determine the compositional changes at atomic scale, a fine focused probe with STEM and an electron energy loss spectrometer and/or x-ray spectrometer need to be used as a complementary way. In the following section, we will discuss electron energy-loss spectrometry in more detail.

2.3 Electron Energy-loss Spectroscopy

2.3.1 Interactions of electrons with sample

TEM works via the interaction of a fast electron beam with a thin specimen. Considering both the particle and wave aspects of the character of electrons, electron interactions with specimen can be classified as elastic scattering, inelastic scattering, coherent and incoherent scattering. Figure 2.15 shows some of the important interactions of fast electron beam with thin specimen. Here we will only outline two main processes: elastic scattering and inelastic scattering.

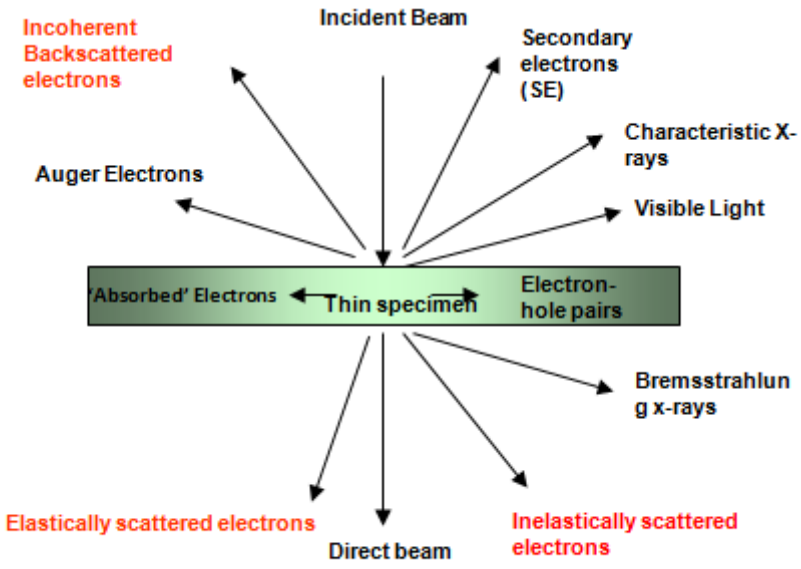

Figure 2.15. *Schematic diagram showing interactions of a direct beam with specimen.*

2.3.1.1 Elastic scattering

Considering electrons as particles, when they interact with an isolated atom, elastic scattering can happen via one of two ways: either as a result of electrons interacting with electron cloud and scattered through small angles of a few degrees (1~2°), or attracted to the positive nucleus and scattered through large angles up to 180°. Elastic scattering will not cause energy loss for electrons. Within crystalline materials,

the low-angle elastic scattering is strongly affected by the arrangement of atoms (atomic planes) within the specimen. Such collective scattering by atoms with the same arrangement in the crystal is referred as diffraction and can be understood as coherent of electron waves. Diffraction is mainly controlled by the incident angle of the electron beam to the atomic planes in the specimen and the spacing of these atomic planes with which it should satisfy the Bragg condition $n\lambda=2d\sin\theta$ (n is an integral). Low-angle, coherent elastic scattering is invaluable in charactering the crystallography of the specimen. As the scattering angle becomes larger, the degree of coherency becomes less due to the introduction of thermal diffuse scattering of the atoms, thus high-angle elastic scattering, which is also termed as Rutherford scattering, is incoherent. High-angle incoherent scattering is highly dependent on the atomic number Z of the atoms in crystal as discussed above in section 2.2.3

2.3.1.2 Inelastic scattering

In contrast to elastic scattering, inelastic scattered electrons of the incident beam will lose some energy in an interaction with the specimen. Energy-loss of incident electrons may occur through procedures like generation of characteristic X-rays or Auger electrons via ionisation of inner-shell electrons, ejection of secondary electrons from the conduction or valence bands of the atoms in the specimen, excitation of plasmons and phonons, and even the damage to the specimen through a number of mechanisms. The two important characteristics of inelastic scattering are the energy loss E and the scattering semi-angle, which determines the efficient collection angle of the spectrometer. Analytical electron microscopy can be performed using an electron energy-loss spectrometer. An EEL spectrum recorded by a spectrometer can contain abundant information about the elemental composition and chemical bonding of the specimen, as well as other features including the electronic structure of the specimen.

2.3.2 Electron energy-loss spectrometer

SuperSTEM2 is equipped with a Gatan Enfina electron spectrometer to record EELS in parallel and its main part is a sector magnet. A sector magnet typically consists of a homogeneous magnetic field normal to the electron beam. Usually for mechanical convenience the electrons are bent through a 90° angle and the Lorentz force causes electrons of different energy to emerge from the spectrometer at different angles. The

spectrometer magnetic field is provided by two parallel polepieces with two current carrying coils providing the excitation. In practice, the polepieces and coils are at atmosphere pressure. An evacuated drift or flight tube, connected to the microscope vacuum system, passes between the two polepieces. An offset voltage may be applied to this drift tube to alter the kinetic energy of all the electrons and rigidly shift the whole energy loss spectrum across the detector system. In order to record the intensity at each particular energy loss as sequence of digital values over a large number of detector channels, a multi-element detector is normally employed to record the whole spectrum in parallel. A spectrometer with this kind of detector is called a parallel-recording spectrometer. The energy resolution of the resulting EELS is mainly determined by the energy spread of the electron source, the resolution of the spectrometer itself, and the resolution of the detection system though there are other factors. Spectrometer dispersion is the vertical displacement of the electron beam per unit change in electron energy and it is typically a few micrometres per eV at the exit of the magnet. There are multipole lenses after the magnet sector to allow the dispersion to be varied for a specific energy range of the spectrum to be recorded. In general, the angular acceptance angle of a spectrometer is much smaller than the angular range that needs to be collected, especially with aberration corrected microscopes such as SuperSTEM2. The significantly enlarged probe convergence semi-angle in such microscopes has increased the difficulty of EELS signal collection. This is because a large portion of the available signal will be lost if the collection angle is not big enough, therefore, it is important to collect over at least the same angular range as the probe for relatively low energy losses and over an even larger range for higher losses. With SuperSTEM2, the QOCM is specially designed for coupling the inelastically scatted electrons into the small entrance aperture of the spectrometer, and can also be used to correct for the higher order aberrations of Enfina spectrometer. Because QOCM does not influence the imaging process except for allowing the collection angles of detectors to be varied/coupling the spectrometer to the microscope, and the 4 projector lenses are only excited for forming diffraction patterns and CTEM images, thus there is no imaging lens after the specimen for EEL spectra and the specimen is directly in the object plane of the spectrometer; therefore the area irradiated by the probe becomes the spectrometer object and its size is

determined by the size of the electron probe, which is about 0.7Å and has effectively improved the spatial resolution for analysis.

2.3.3 EELS

After interactions with the specimen, electrons will undergo either elastic scattering or inelastic scattering. A spectrum recorded by a spectrometer will contain peaks produced by electrons with and without energy loss. Basically, a typical spectrum can be recorded with three different regions – the zero-loss peak, the low-loss region and the core-loss region, as shown in Figure 2.16. Depending on the information required, specific energy ranges can be selected for a spectrum.

Zero-loss peak: The zero-loss peak (ZLP) primarily contains electrons that are elastically forward-scattered and also electrons that have suffered minor energy loss not resolvable by the spectrometer. Normally, the FWHM (full width at half maximum) of the zero-loss peak can be used as an indicator of the total resolution of a spectrometer/microscope system.

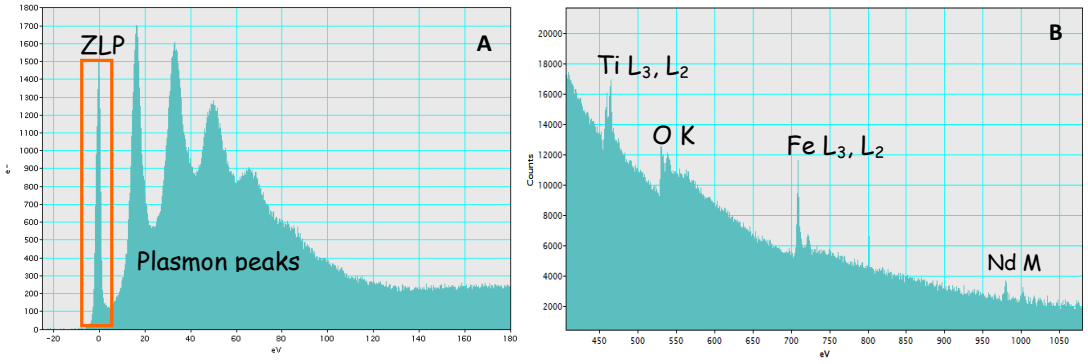

Figure 2.16. *EELS showing different energy loss regions of spectrum. A) a spectrum showing ZLP marked in orange rectangle and the rest of the peaks are plasmons caused by multiple excitation; Plasmon peaks are rather high because the sample is very thick. B) a spectrum showing core-loss region with characteristic ionization edges labelled.*

Low-loss region: In this region (e.g. < 50 eV), energy losses are mainly due to interactions with oscillations of weakly-bound (outer-shell) electrons ("plasmons") in the specimen, as well as interband and intraband transitions. Intensity in this region of the spectrum can, for instance, give information on sample optical properties. Specimen thickness, relative to the inelastic scattering mean-free path, can also be easily determined by the ratio of the intensity of the whole spectrum to the intensity of the

zero-loss peak. With high-resolution EELS, we might be able to measure the energy bandgap for some materials. But to achieve this, a very narrow energy spread beam is needed in the microscope, probably created using a monochromator.

Core-loss region: Energy loss in this region (extends from about 40 or 50eV to several thousand eV) is caused by inelastic excitation of inner-shell electrons to unoccupied states above the Fermi level. This region therefore reflects the atomic character of the specimen. An abrupt increase in intensity in the spectrum at an energy loss equal to an inner-shell ionisation energy is termed an ionization edge. Since the energy of the edge threshold is determined by the binding energy of the particular electron sub-shell within an atom, the ionisation edge energy is characteristic of a particular chemical element and is known for every electron shell, thus ionisation edges can indicate which elements are present within the specimen. Choosing a window of an energy loss (around 10eV or more in width) corresponding to an inner-shell ionization edge of a known element, **an elemental map** that represents the distribution of that element can be formed, possibly with spatial resolution down to atomic resolution depending on the set up of the microscope. This compositional mapping technique is probably the most powerful use of inelastic scattering. Above the edge onset, within the first 30-40eV, is defined as electron energy loss near-edge structure **(ELNES)**. ELNES can give a direct insight of the associated electronic structure and atomic bonding in the solid, like determination of local coordination by using "coordination fingerprint" or valence states of atomic species. This is because, in solids, the unoccupied electronic states just above the Fermi level can be significantly modified by the chemical bonding between neighbouring atoms leading to a complex but specific density of states (DOS) which will be reflected by the ELNES as spectral fingerprint. By using a proper collection aperture to satisfy the dipole selection rule ($\Delta \ell = \pm 1$), different edges of the same element can represent different symmetries of the final state, for instance, a K-edge will probe the unoccupied *p*-like DOS, while an $L_{2,3}$-edge will probe the unoccupied *s*- and *d*-like DOS. Beyond the near-edge region, a region of weaker, extended oscillations is superimposed on the gradually decreasing tail of the core loss edge. This region is known as extended energy loss fine structure (EXELFS). The details of the oscillations may be used to probe the coordination of a particular atom.

2.3.4 Spectrum imaging

Spectrum imaging (SI) is a technique which is deployed to acquire an energy-loss spectrum at each pixel as the STEM probe is rastered over the specimen. With spectrum-imaging technique, a four-dimensional data array is created which corresponds to electron intensity within a three-dimensional volume of (x,y,E) space [Jeanguillaume and Colliex 1989], Figure 2.17. As the probe is scanned by the computer and spectra are acquired by the computer, this concept has now been extended to record a wide range of data at each pixel simultaneously, like electron dispersive x-ray, HAADF and EEL SI. However, as STEM acquisition is point by point and EEL spectrum imaging takes a significant time, drift caused distortion of the image is unavoidable. To minimise this, drift correction is very important. This is achieved by recording a drift correction area with a short exposure survey then re-require it after every tenth line of the spectrum image acquisition. By comparing the re-required images to the original, the magnitude and direction of the drift can be determined and corrected. To make the recording times realistic, a parallel-recording spectrometer like the Gatan Enfina, which means many spectra can be stored on the chip before reading out, is needed. Besides, incorporating drift correction to limit the distortion of the image and the simultaneously acquired image to ensure perfect registration between the spectral data and position is also necessary. For EEL spectrum data analysis, ideally, both the low loss and the core loss regions of the EEL spectrum should be recorded under the same electron optical conditions at the same pixel before moving to the next pixel to ensure perfect registration. However, the large dynamic range of the EEL signal means that a single integration time cannot be used to record the whole spectrum. To overcome this limit and also to reduce the sample damage caused by the incident beam, a fast beam switch (FBS) [Craven 2002, Scott 2008] is very useful. The FBS has a sub-microsecond response time which allows rapid shuttering of the beam and so is capable of handling the large range of exposure times required to cover both core and low loss spectra. As a consequence, a core loss spectrum at each pixel can be collected after a low loss spectrum with the same electron optical conditions. As the datasets have “exact” pixel correlation, it is possible to correctly remove multiple scattering from the EELS core edges, either by Fourier-ratio deconvolution or by splicing the EELS SIs together and using Fourier-Log deconvolution. The spectra can also be normalized for intensity

allowing absolute quantification [Craven 2008]. This technique is also known as dual EEL spectroscopy. Unfortunately, the present set up of SuperSTEM2 does not have a FBS, thus it is not possible to do the absolute quantification with the defects as will be discussed in chapter 4 and chapter 5. But the complete dataset still can be processed for quantitative analysis like elemental mapping to show the two-dimensional distribution of a chosen element or a specific chemical bonding using ELNES signatures. With aberration correction, SuperSTEM2 has achieved probe sizes down to sub-Angstrom dimensions. Such a fine probe, combining simultaneous HAADF imaging with Gatan Enfina spectrometer, has enabled the generation of elemental maps with atomic resolution, as will be shown in chapters 4 and chapter 5. Such high spatial resolution is difficult for energy filtered imaging in the CTEM (EFTEM), which involves the selection of an energy losses window from the transmitted electron beam via use of energy selecting slit after the EEL spectrometer, to achieve without a chromatic aberration correction. EFTEM is more suitable for mapping unknown elemental distributions from larger fields of view with relatively short acquisition times while STEM is excellent with regions need more detailed analysis because it allows the maximum information per incident electron to be acquired with good spatial registration as well as the orchestration of the acquisition [Crave 2011].

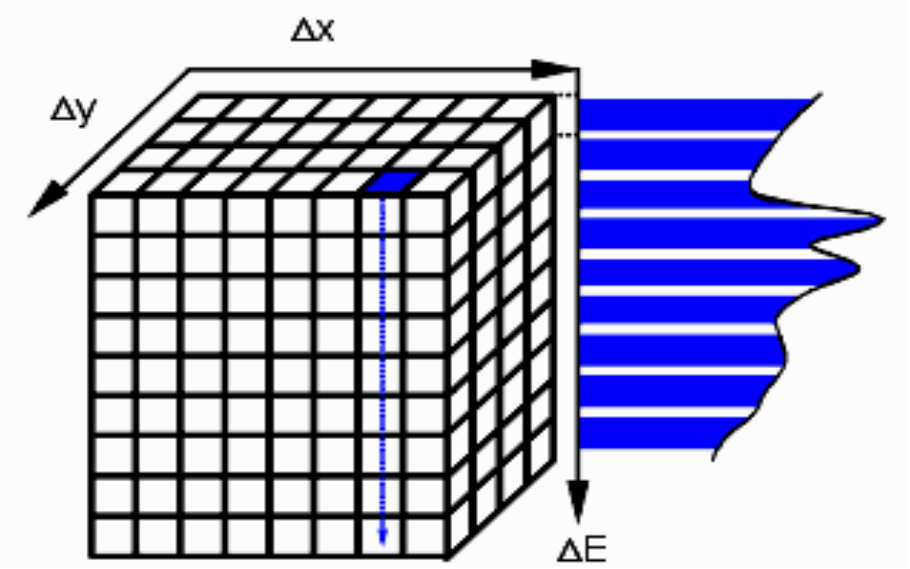

Figure 2.17. *A schematic diagram of spectrum imaging technique, which can be used for quantitative analysis [Jeanguillaume and Colliex 1989].*

2.4 Sample Preparation

2.4.1 Ceramic preparation

Co-doped BFO ceramics were prepared by our collaborators at the University of Sheffield. The preparation procedure is conventional mixed oxide synthesis [Kalantari 2011], using Bi_2O_3 (99.9 %, Acros Organics), Fe_2O_3 (99.8 %, Alfa Aesar), TiO_2 (99.99 %, Sigma Aldrich) and Nd_2O_3 (99.90 %, Sigma Aldrich) as the starting reagents. The appropriate amounts of dry raw materials were weighed and attrition milled for an hour with yttria-stabilised zirconia media in iso-propanol. Mixed powders were calcined for 3 h at the optimum reaction temperature which is 1020°C for $(Bi_{0.85}Nd_{0.15})(Fe_{0.9}Ti_{0.1})O_3$. The reacted powder was sieved through a 355 μm sieve and then attrition milled as above. The powder was pressed into pellets of 10 mm diameter and ~ 2.5 mm thickness by uniaxial pressing at an applied load of 1 ton for 1 minute. Pellets were then sintered in air for 3 h at an optimum sintering temperature, which is 1050°**C**. The optimum sintering temperature was judged to be that at which the proportion of secondary phases was minimal and density > 95 % of the theoretical density.

2.4.2 Specimens for TEM

All the specimens used for the TEM/STEM experiments in this thesis are planar samples, which were prepared by a conventional procedure of cutting, mechanical thinning, dimpling, and ion beam milling.

Cutting and pre-thinning disks: 3mm - diameter disks are made from the 10mm pellet by using the Ultrasonic Disc Cutter, then the disks are pre-thinned to about 80 - 100 micrometers by hand-grinding.

Dimpling: Disks pre-thinned in previous step are then put in a Gatan dimple grinder to thin the centre of the disk to a thickness of about 20 μm. The dimpler uses a rotating brass wheel coated with diamond paste to grind material from the surface of the disk. A specific rotational speed and weight can be applied to the wheel to accurately thin the disk on both sides. A higher grade diamond paste is also used with a soft felt wheel for a final polish. To remove the debris from grinding, manually rinsing is necessary.

Ion milling: The pre-thinned sample is then put in a Gatan Precision Ion Polishing System (PIPS), model 691, modified with a low voltage supply and cold stage

for ion milling in order to get the specimen thickness to electron transparency. The PIPS uses two argon ion guns that can be directed with specific angles of incidence onto the sample surface. Using a small angle of incidence (from surface) is preferable for two reasons. First, ion implantation is greatly reduced at glancing angle; furthermore, any preferential thinning of different materials is minimised [Williams & Carter 1996]. The ion guns were orientated at ±4° incident angles which allow both side of the sample to be milled simultaneously. Within our study, samples were initially milled at an acceleration voltage of 4 kV while being rotated at 2 rpm for approximately 4 hours, then the acceleration voltage was reduced to 1 kV for about 2-3 hours and 500 V for about 30 minutes until light was visible through a small hole formed at or near the centre of the sample. The reason for reducing the acceleration voltage is to minimise surface damage introduced by ion bombardment.

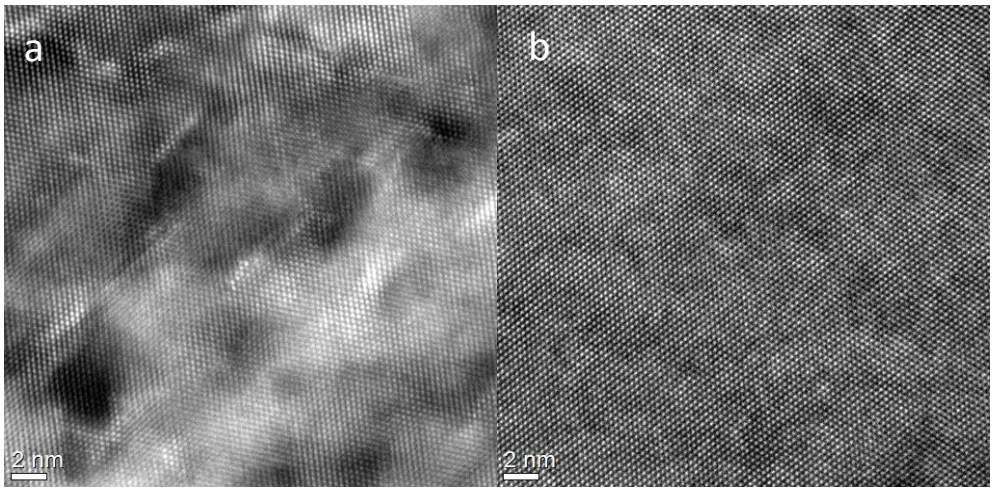

Figure 2.18*. Images of same silicon sample taken at same conditions of TEM. a) Before gentle milling. b) After gentle milling.*

Ion Polishing: final ion polish was, in some case, performed using a TECHNOORG LINDA Gentle Mill, Model IV5. This low kV ion mill was operated at 300eV with an ion incidence angle of 12 degrees. Each side of the sample was milled for 15 minutes. This final polishing procedure improves the surface quality of the prepared sample by minimising any amorphous layer produced by earlier stages of preparation. Figure 2.18 shows two TEM images of a silicon sample before and after gentle milling, respectively. It is very obvious that the surface of the sample is rather rough after initial

milling, as shown by the patches of different intensities across the image, as compared with the image taken after the gentle mill.

Carbon Coating: After the final stage of ion polishing, finally the TEM samples were carbon coated on both sides using thermal evaporation of carbon to prevent charging from the electron beam. Otherwise, a number of undesired effects can occur during investigation with TEM/STEM including unpredictable sample movement, focal or astigmatism drift, and even sample breakage.

References:

Allen J. E., Hemesath E. R., Perea D. E., Lensch-Falk J. L., Li Z.Y., Yin F., Gass M. H., Wang P., Bleloch A. L., Palmer R. E., Lauhon L. J., **(2008)** High-resolution detection of Au catalyst atoms in Si nanowires, Nature Nanotechnology **3(11)**, 676-681.

Craven A. J., Wilson J. and Nicholson W.A.P., **(2002)** Ultramicroscopy **92,** 165-180.

Craven A. J., MacKenzie M. and McFadzean S., **(2008)** Dual energy range EELS spectrum imaging using a fast beam switch, EMC2008: Vol 1, Instrumentation and Methods / edited by Luysberg M. *et al*., Springer ISBN 978-3-540-85154-7, 363-364.

Craven A. J., **(2011)** in Aberration-corrected analytical transmission electron microscopy / edited by Brydson R. et al., **(Chap. 6),** John Willey & sons, Ltd.

Delby N., Krivanek O. L., Nellist P. D., Batson P. E., Lupini A.R., **(2001)** Progress in aberration-corrected scanning transmission electron microscopy, Journal of Electron Microscopy **50 (3)**, 177-185.

Egerton R. F., **(2005)** Physical principles of electron microscopy: an introduction to TEM, SEM, and AEM, New York: Springer Science+Business Media.

Haider M., Rose H., Uhlemann S., Schwan E., Kabius B., Urban K., **(1998)** A spherical-aberration-corrected 200 kV transmission electron microscope, Ultramicroscopy **75**, 53-60.

Hall, C. R. and Hirsch, P. B., **(1965)** Effects of thermal diffuse scattering on propagation of high energy electrons through crystals, *Proceedings of the Royal Society of London* Series A, **286,** 158-177.

Hall C. E., **(1953)** Introduction to Electron Microscopy. McGraw Hill, New York.

Hartel P., Rose H., Dinges C., **(1996)** Conditions and reasons for incoherent imaging in STEM, Ultramicroscopy **63**, 93-114.

Hawkes P. W., and Kasper E., **(1989)** Principle of electron optics, Academic Press, London.

Hawkes P. W., and Kasper E., **(1996),** Principles of Electron Optics **2**, Academic Press, London and San Diego, Ch. 41.

Howie A., **(1979)** Image contrast and localized signal selection techniques, Journal of Microscopy, **117**, 11-23.

Jeanguillaume C. and Colliex C., **(1989)** Spectrum-image: The next step in EELS digital acquisition and processing, Ultramicroscopy **28,** 252-257.

Krivanek O. L., Dellby N., Lupini A. R., **(1999)** Towards Sub-Angstrom Electron Beams, Ultramicroscopy **78**, 1-11.

Krivanek O. L., Corbin G. J., Dellby N., Elston B. F., Keyse R. J., Murfitt M. F., Own C. S., Szilagyi Z.S., Woodruff J.W., **(2008)** An electron microscope for the aberration-corrected era, Ultramicroscopy **108**, 179–195.

Krivanek O. L., Chisholm M. F., Nicolosi V., Pennycook T. J., Corbin G. J., Dellby N., Murfitt M. F.,. Own C. S., Szilagyi Z. S., Oxley M. P., Pantelides S. T. and Pennycook S. J., **(2010)** Atom-by-atom structural and chemical analysis by annular dark-field electron microscopy, Nature **464**, 571-574.

Kalantari K., Sterianou I., Karimi S.,. Ferrarelli M. C, Miao S., Sinclair D. C., and Reaney I. M., **(2011)** Ti-Doping to Reduce Conductivity in $Bi_{0.85}Nd_{0.15}FeO_3$ Ceramics, Adv. Func. Mater., **21**, 3737–3743.

Nellist P. D. and Pennycook S. J., **(1998)** Sub-Ångström resolution by underfocused incoherent transmission electron microscopy, Phys. Rev. Lett., **81**, 4156-4159.

Nellist P. D., **(2011)** Aberration-corrected analytical transmission electron microscopy/ edited by Brydson R. et al., (Chap. 5), John Willey & sons, Ltd.

Pennycook S. J. and Jesson D. E., **(1990)** High-resolution incoherent imaging of crystals, Phys. Rev. Lett., **64**, 938-941.

Rose H. and Wan W., **(2005),** Aberration correction in electron microscopy, Proceedings of 2005 Particle accelerator conference, Knoxville, Tennessee, 44-48.

Rutherford E., **(1911)** The Scattering of α and β Particles by Matter and the Structure of the Atom, Philosophical Magazine. Series 6, **21**, 669-688.

Scherzer O., **(1936)** Über einige Fehler von Elektronenlinsen, *Zeitschrift Physik*, **101**, 593.

Scherzer O., **(1947)** Sphärische und chromatische Korrektur von Elektronenlinsen, *Optik* **2**, 114-132.

Scherzer O., **(1949)** The Theoretical Resolution Limit of the Electron Microscope, J. Appl. Phys., **20,** 20-29.

Scott J., Thomas P. J., MacKenzie M., McFadzean S., Wilbrink J., Craven A. J. and Nicholson W. A. P., **(2008)** Ultramicroscopy **108(12)**, 1586-1594.

Uhlemann S., and Haider M., **(1998)** Residual wave aberrations in the first spherical aberration corrected transmission electron microscope, Ultramicroscopy **72**, 109.

Williams D. B., Carter C. B., **(1996)** Transmission electron microscopy, Springer Science +Business Media, LLC.

Zach J., **2009** Chromatic correction: a revolution in electron microscopy?, Phil. Trans. R. Soc., A, **367**, 3699-3707.

Chapter 3 Computational software related to data analysis

3.1 Introduction

In order to be able to perform quantitative analysis of atom resolution data, several computational methods have been used for noise reduction, drift correction and quantitative atomic position measurement. Principal Component Analysis (PCA) [Jolliffe 2002] is used prior to elemental mapping with EELS to reduce the background noise and thus improve the visibility weak signals obscured by the background noise. The Statistically Determined Spatial Drift (SDSD) software [Schffer 2004] is used for the drift correction and alignment of an image series to produce a high signal to noise image, which is minimally affected by sample drift. The iMtools package is used for accurate atom position determination from high-resolution STEM images prior to further scanning distortion correction. Final scanning distortion correction and averaging of images of identical features is done using our own routines within Microsoft Excel, as well as the construction of three dimensional atomic structure models. These models are then tested in image simulations using the QSTEM package [Koch 2002], which are used to help interpret the high-resolution images and/or verify the proposed models of new structures. In some cases, density functional theory calculations were carried out on our three dimensional structures by external collaborators at the ETH Zürich using the VASP programme. In this chapter, I will give some brief descriptions of the methods and background of the computational methods used in the data analysis.

3.2 Principal Component Analysis (PCA)

PCA is one of the most popular forms of Multivariate Statistical Analysis, which is a useful family of techniques to analyse large datasets containing many known and/or unknown variables. The general concept of **PCA** is to identify any statistically significant features in large data sets and to reduce random noise components efficiently in a statistical manner [Jolliffe 2002]. This technique is applied to the EEL-SI analysis in this work by a PCA plug-in for Gatan Digital Micrograph, developed by Masashi Watanabe [Watanabe 2005], to reduce the random background noise in the spectrum and thus enhance the weak signals hidden by the noise prior the elemental mapping. For

example, in Figure 3.1, the Nd $M_{4,5}$ signal in the raw EEL-SI is very weak and almost hidden by the random back ground noise. After the PCA is applied, the weak Nd signal is enhanced greatly due to the random background noise has been removed. The main concept of this method is summarised in the following paragraph.

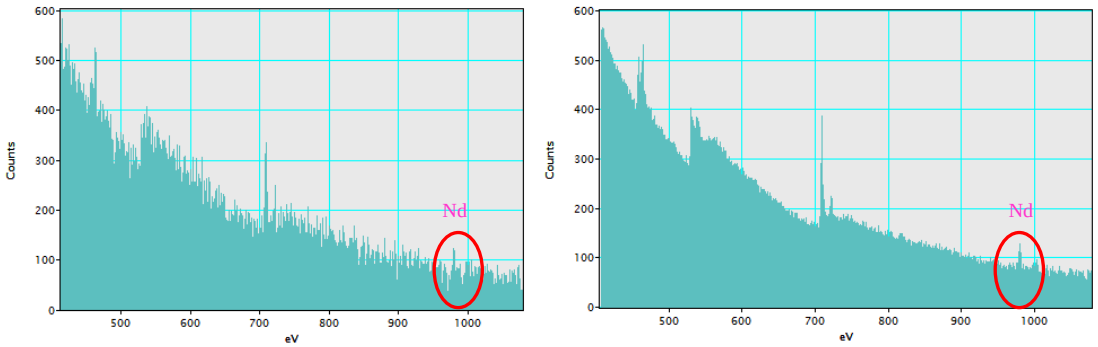

Figure 3.1. *Comparison of spectra before and after PCA: left is the raw spectrum; right is the spectrum after PCA was applied.*

With an EEL-SI that contains three-dimensional information, it can be decomposed into two spatial axes (x,y) and one energy axis (E). By applying PCA, The EEL-SI dataset can be described by a data matrix $\vec{D}_{((x,y),E)}$ formed by the product of a score matrix $\vec{S}_{((xy)n)}$, which contains the spatial information (x,y) and is stored in the columns of the data matrix, and a loading matrix $\vec{L}^{T}_{(E,n)}$, which includes the spectral information (E) and is put in the rows [Malinowski 2002],

$$\vec{D}_{((x,\,y),\,E)} = \vec{S}_{((x,\,y),\,n)} \times \vec{L}^{T}_{(E,\,n)} \qquad (3.1)$$

where the superscript T of $\vec{L}$ represents a matrix transpose; n is the number of principal components. In the loading matrix $\vec{L}^{T}$, each row is uncorrelated to the other rows and is called an eigenspectrum of the dataset. The corresponding column of the score matrix $\vec{S}$ represents the spatial amplitude of each eigenspectrum. Thus, the individual product of each row of the loading matrix and the corresponding column of the score matrixes produces a principle component. The number of principal components, n, is mathematically equal to the smaller number of x*y or E. In the decomposed matrixes, the principal components are ordered from high to low according to their eigenvalues, so is the variance or information that they describe.

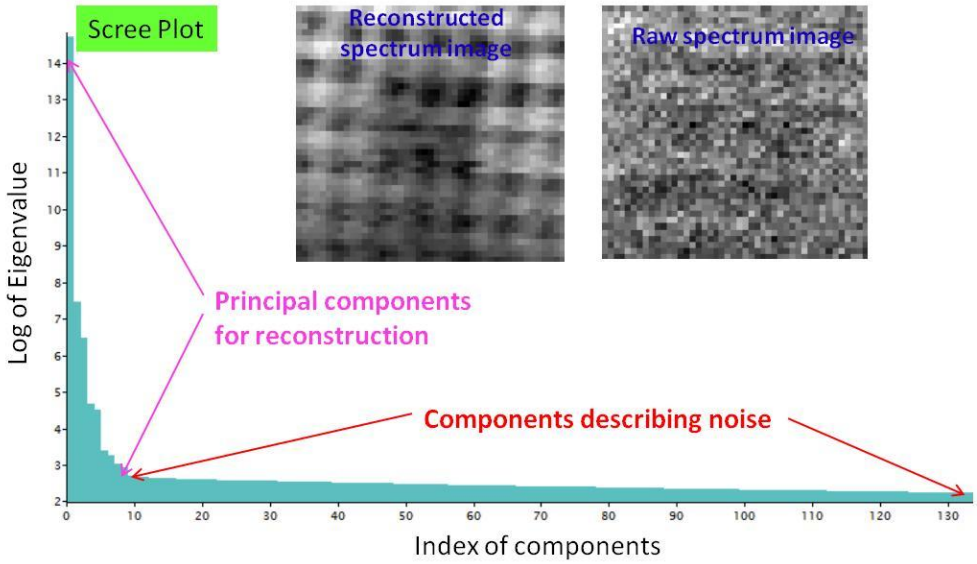

Figure 3.2. *An example of the screen plot, showing the correlation between log eigenvalue and components. Significant features are represented by those exponentially decreased principal component, experimental random noise are represented by the straight line in the scree plot. 10 components reconstructed spectrum image showing the random back ground noise has been greatly reduced.*

Typically, the number of dominant features in the dataset is much less than n, and many of the weak principal components will therefore describe experimental noise. If the number of non-noise principal components, m, is determined, the original dataset can be reconstructed using this limited number of principal components, m:

$$\vec{D}_{((x,y),E)} = \vec{S}_{((x,y),m)} \times \vec{L}^{T}_{(E,m)} \qquad m << n \qquad (3.2)$$

As a result of the reconstruction, the experimental noise can be removed efficiently from the original dataset without losing spatial or energy resolution [Jolliffe 2002, Burke 2006, Bosman 2006, Watanabe 2007]. To determine the value for m, an approach named as the "scree plot" is used whereby the logarithms of the eigenvalues are plotted versus the component number (Figure 3.2). Since the eigenvalues of random-noise-containing principal components decrease exponentially, components that only describe experimental noise should lie on a straight line in the scree plot. In this work, this number m was generally in the range of 10 ~ 20. Reconstructed spectrum images using different number of components have been compared. There are no subtle features have

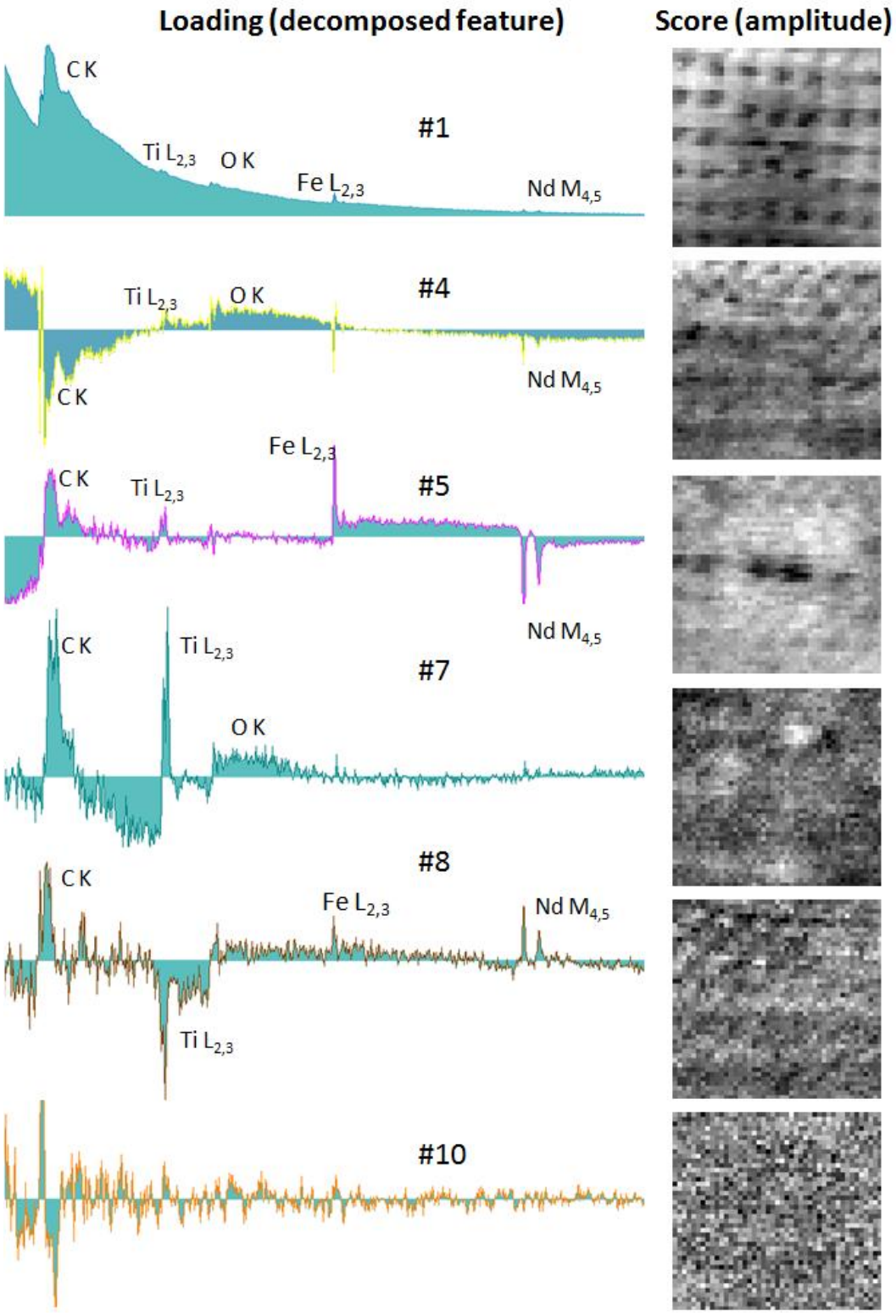

Figure 3.3. *Selected pairs of the loading spectra and the corresponding score images of the components showing significant features are represented by those exponentially decreased principal components in the scree plot of Figure 3.2.*

been missed out as long as the number of components for reconstructing is beyond the number of the breaking point in the scree plot. The only difference between them is that reconstructed spectrum images with larger number of components have more background noise induced. Figure 3.2 shows a scree plot and its correlated raw spectrum image acquired from one of the defects, which will be discussed in chapter 4, and the corresponding reconstructed spectrum image using 10 principal components indicated by the scree plot. As a result, the reconstructed spectrum image shows that the random background noise has been effectively removed from the raw data by PCA. Figure 3.3 gives a further insight on some selected pairs of the loading spectra and their corresponding score images of the components of the raw EEL-SI and how the number of principal components provided by the scree plot for reconstructing the EEL-SI is valid. The loading spectrum of #1 component represents the average spectrum of the EEL-SI, which means it is always the most significant component in the dataset. Any component that contains signals higher than #1 indicates its significant difference from the average. Thus, the loading spectra after #1 component contain positive and negative peaks. The #4 loading spectrum is dominated by positive O K-edge together with a little bit of Ti L-edge; C K-edge and Nd M-edge are negative. The corresponding score image indicates that the dominating O are distributed relatively even within the EEL-SI. The #5 loading spectrum has positive peaks of C K-edge, Ti L-edge and Fe L-edge but with Fe L-edge signal stronger, Nd M-edge shows a strong negative value, thus the bright regions in the score image likely represents the distribution of Fe, and the dark contrast possibly means the distribution of Nd. The #7 loading spectrum contains positive peaks of C K-edge, Ti L-edge and O K-edge, but with Ti signal competitive to C signal; thus these relatively brighter 3 spots represent the Ti distribution there. The #8 loading spectrum has positive C K, Fe L and Nd M peaks, and a negative Ti L peak. However, as Nd M peak is still relatively weak compared to the C K peak, it is difficult to discriminate any significant feature of Nd in the corresponding score image. From the #10 loading spectrum and its related score image, it is obvious that their corresponding principal can be clarified to the noise component. Over all, by combining the information from the decomposed components together with the scree plot, the number of principle components for reconstructing the EEL-SI can be determined reliably.

Therefore, PCA can reduce the random background noise effectively and give the enhanced features of the EEL-SI.

3.3 Drift Correction via the Statistically Determined Spatial Drift (SDSD) Method

Image processing to extract valuable positional atomic-column data from HAADF - STEM images is very important for the quantitative analysis. In order to get the precise location of an atom column with sub-pixel accuracy, corrections for distortions due to specimen drift or scanning electronic artefacts like hysteresis effects during the "fly back" between scan lines is necessary [Sanchez 2006]. Since STEM records the pixels sequentially, and to record a full size image with good signal to noise ratio always takes a longer exposure, drift is unavoidable.

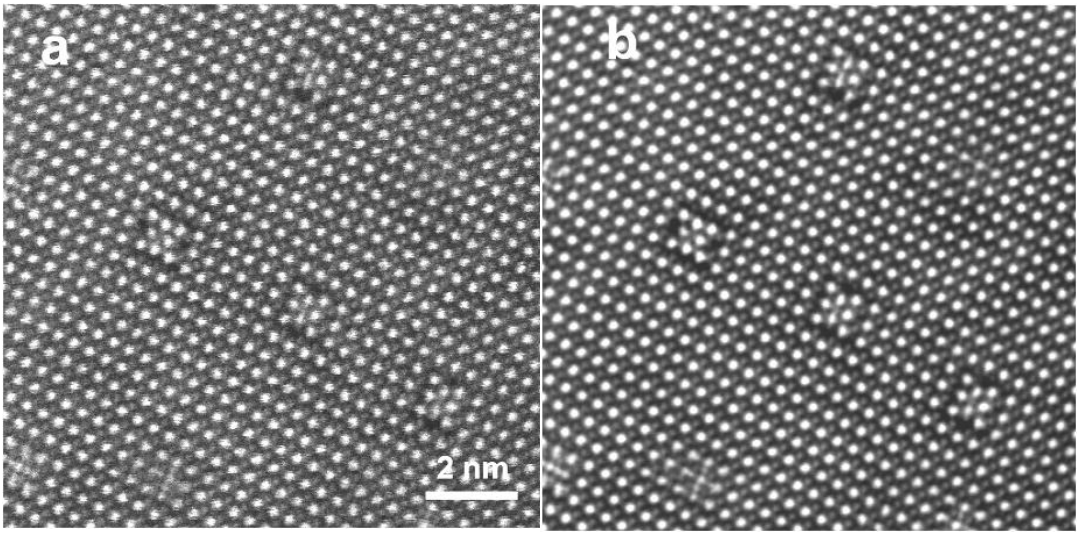

Figure 3.4. *(a) One slice from a series of images taken using a dwell time of 5μs/pixel; (b) A sum of the image series after spatial drift correction.*

To minimize these drawbacks, a stack of the HAADF images with very short exposure time was taken, and then the SDSD software tool [Schaffer 2004] was used, which is a plug-in to the Digital Micrograph (DM) software, to carry out the correction for the sample drift. Finally, a sum of the corrected images was created to increase the signal to noise ratio (SNR) for the extraction of atom columns' positions with high accuracy. Within this work, corrections for distortions were carried out using the FFTW routines from Christoph Koch [http://www.christophtkoch.com/stem/], and the most

reliable cross-correlations were generally achieved using the "Phase Correlation" option in the SDSD software without any filter being chosen. By cross-correlating all image pairs with each other and statistically evaluating all the obtained shift vectors, the algorithm increases its robustness. Outliers can thus be identified and excluded resulting in a much more accurate drift determination with sub-pixel precision [Schaffer 2004]. Figure 3.4 shows one slice of the image from a stack and the sum of the stack images after correction. As a result the SNR is improved significantly.

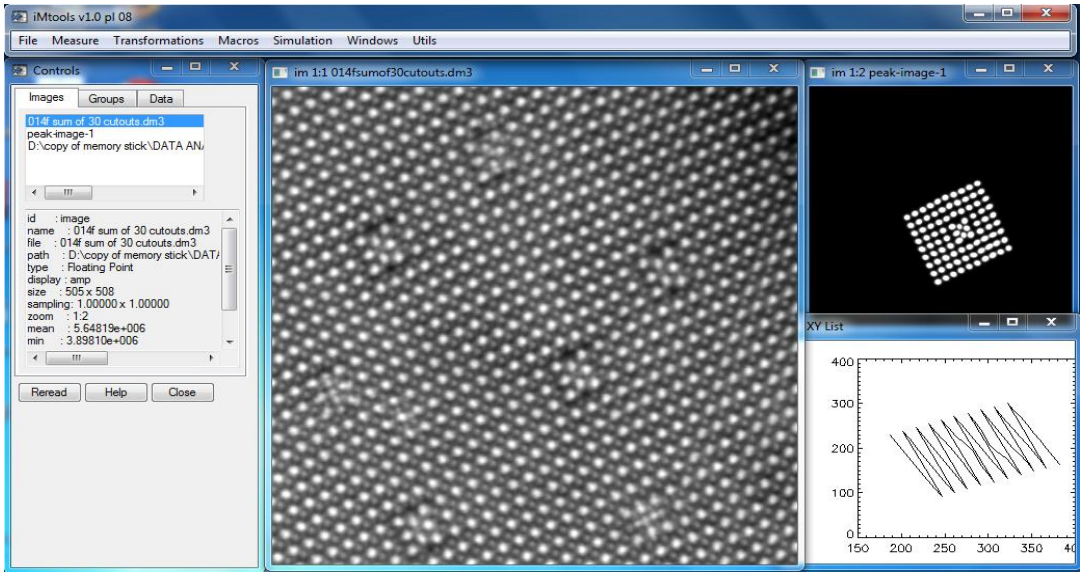

Figure 3.5. *Interface of iMtools and fitted peak image (top-right) from the SDSD corrected HAADF image (left) together with corresponding coordinates list.*

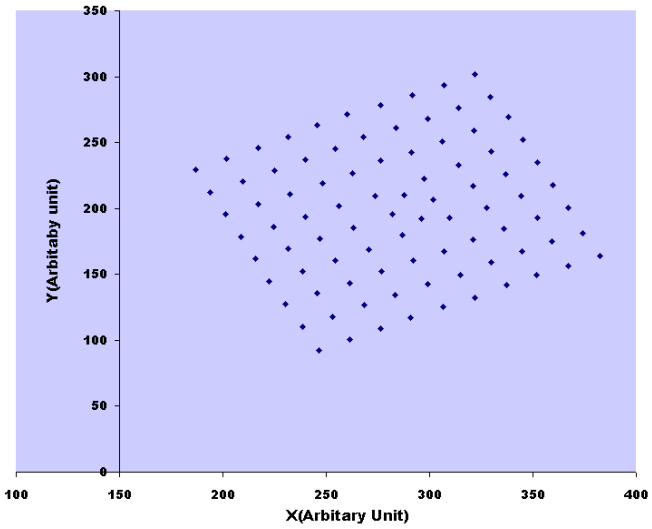

Figure 3.6. *A chart of the corresponding defect in Figure 3.5 plotted with Excel using the coordinations (x, y) extracted by iMtools.*

3.4 iMtools

iMtools programmed by Dr Lothar Houben in Ernst Ruska-Centre Jülich is a binary software collection and graphical user interface developed for digital image processing of electron micrographs [http://www.er-c.org/centre/software]. One of its implementations is the determination of atom column positions from atomic resolution electron microscope images by two-dimensional (2D) Gaussian fitting to the peak phase maxima (see Figure 3.5), which allows peak centre interpolation with sub-pixel accuracy [Houben 2006]. In this thesis, 2D Gaussian peak fitting by iMtools was applied to the summed HAADF images created by SDSD for the determination of the atom positions to ensure the precise location of atom columns. Once the atom column positions were determined, their coordinates were exported to a spreadsheet for the further correction of the distortions likely caused by imperfections in the scanning system (Figure 3.6).

3.5 Distortion Corrections and Primary Model Development

Figure 3.6 is plotted from the data imported from iMtools showing the atom column positions of a nanorod with its surrounding doped - BFO matrix along $[001]_o$ direction (here the subscript defines orthorhombic, unless stated otherwise, for example, to define primitive perovskite structure). The cell parameters of a closely related composition with the same crystal structure, $Bi_{0.85}Nd_{0.15}FeO_3$, were Rietveld-refined from x - ray diffraction and neutron powder diffraction data as part of previous works [Karami 2009, Levin 2010]. Results from these refinements showing that the structure is of $PbZrO_3$ - type orthorhombic, with cell parameters of a = 5.5959 Å, b = 11.2399 Å, c = 7.8076 Å. According to the $PbZrO_3$-type orthorhombic structure that has unit cell of $\sqrt{2}a_c \times 2\sqrt{2}a_c \times 2a_c$ (a_c is the cell parameter of the primitive perovskite) and reducing this orthorhombic cell to a pseudotetragonal cell, cell parameters of a ≈ b ≈ 3.965 Å, c = 3.904 Å can be obtained. In this case, the cells in the $[001]_{pc}$ direction can be assumed to be square on average and oriented with a side of 3.965 Å. However, due to the linear distortions likely originates from small non-idealities in the scanning system, the atom column positions in the perovskite matrix surrounding the nanorods displayed in Figure3.6 are clearly not showing squared unit cells. Therefore, to build an atomic structure model, corrections of these distortions are necessary. The typical procedure of linear distortion correction includes shifting the origin for the interpolated peak positions

to zero, horizontal correction, shear correction and magnification correction to make the crystal cells in the [001] direction to be square. All the measurement of these corrections was performed using patches of perfect perovskite structure that are a bit further away from the defects or anti-phase boundaries by performing least squares fitting to determine the gradients and spacings of rows of peak positions, and then converting the fit parameters to correction matrices to apply to the dataset (i.e. rotation, shear, and magnification and anisotropic expansion matrices). The matrix used for the rotation correction was constructed from the averaged rotational gradient from the rows of peaks of those chosen patches of perfect perovskite structure. The matrix for shear correction was constructed from the averaged gradient of the columns of peaks that should be vertical to the rows of peaks used for the rotation correction. In general, for shear corrections, the averaged gradient of the columns of peaks would result in the angle value of ~1.50 radians (about 86 degrees with respect to horizontal axis).

After all the procedure for correction was done, atom positions with identical features were overlaid and averaged in order to get the unbiased atom positions. Errors were generally less than 25pm. Then, by correlating the atoms position with the chemical information from the atomic resolution EELS-SI, proposed structure model were built up for further test with image simulation or electronic structure calculation.

3.6 Image Simulation

Image simulation is an essential tool in the effective interpretation of high resolution electron microscope images and is particularly necessary in the study of crystalline samples where dynamical effects can be important [Kirkland 1987]. This is because artefacts due to the aberrations of the instrument and/or specimen manipulation (like thickness and tilt) will be present in the images. Additionally, the beam-specimen interaction can also have big and complex effects on the images, especially in HRTEM. Image simulation is therefore essential in the detection and understanding of these artefacts. Of special interest to this work, in the process of discovering new structures, proposed models can be verified by comparing calculated images with the experimental images. Here I will briefly explain a well-known method – the multislice method using the frozen phonon method for HAADF-STEM image simulation of thick specimens (>10Å), which was used for the simulations in this study.

3.6.1 Multislice algorithm

The multislice algorithm is based on the physical optics theory of Cowley and Moodie [Cowley and Moodie 1957] and a numerical integration method to solve the Schrödinger equation. This allows the dynamical simulation of images of thick specimens. With this method, a thick specimen is divided into thin two-dimensional slices perpendicular to the electron beam direction (like a loaf of sliced bread) when the effect of dynamical scattering (whereby the electron is scattered more than once as it passes through the specimen) is considered. Each slice is thin enough to be treated as a weak phase object (which only gives a small change in the wavelength of the electrons as they pass through the specimen) and the propagation between slices is determined using Fresnel diffraction (waves are treated as spherical waves, not plane waves) over a distance Δz. In STEM, the wave function $\psi_p(\vec{x})$ of the electron probe incident upon the specimen at position $\vec{x}_p$ is given by integrating the aberration wave function $\exp[-i\chi(\vec{k})]$ over the objective aperture as

$$\psi_p(\vec{x},\vec{x}_p) = A\int_0^{k_{\max}} \exp[-i\chi(\vec{k}) - 2\pi i\vec{k}\bullet(\vec{x}-\vec{x}_p)]d^2\vec{k} \qquad (3.3)$$

where $\lambda k_{max}=\alpha_{max}$ is the maximum angle in the objective aperture and A is a normalization constant chosen to yield:

$$\int\left|\psi_p(\vec{x},\vec{x}_p)\right|^2 d^2\vec{x} = 1 \qquad (3.4)$$

As the electron probe passes through each slice of the specimen it is modulated by the specimen transmission function $t(\vec{x})$ which is considered as a small, position dependent phase shift to the wave function due to the slice, which is so thin that it is treated as a weak phase object. The resulting transmitted wave function is

$$\psi_t(\vec{x},\vec{x}_p) = t(\vec{x})\psi_p(\vec{x},\vec{x}_p) = \exp[i\sigma\upsilon_z(\vec{x})]\psi_p(\vec{x},\vec{x}_p) \qquad (3.5)$$

in which $t(\vec{x}) = \exp[i\sigma v_z(\vec{x})]$ with $\upsilon_z(\vec{x})$ the total projected atomic potential of the single specimen slice along the optic axis, which could be calculated from the electron

scattering amplitudes in the first Born approximation [Kirkland 1998]. $\sigma=2\pi me\lambda/h^2$ is termed as the interaction parameter.

After transmission, the wave function is propagated through free space to the next slice via convolution in real space (or multiplication in reciprocal space) with the propagator function defined as

$$FT[p(x,y,\Delta z)] = P(k,\Delta z) = \exp(-i\pi\lambda k^2 \Delta z) \tag{3.6}$$

Thus in real space:

$$p(x,y,\Delta z) = FT^{-1}[P(k,\Delta z)] = \frac{1}{i\lambda\Delta z}\exp[\frac{i\pi}{\lambda\Delta z}(x^2+y^2)] \tag{3.7}$$

This concept allows the calculation to proceed using a two-step approach. The wave function is first transmitted through a slice and then propagated through vacuum to the next slice. If the slices in the specimen are labelled n=0,1,2,3… then the depth in the specimen is z_n; the wave function at the top of each slice is labelled as $\psi_n(x,y)$ and the propagator and transmission functions for each slice are labelled as $p_n(x,y,\Delta z_n)$ and $t_n(x,y)$, respectively; the wave function at the top of n+1 slice would be:

$$\psi_{n+1}(x,y) = t_n(x,y)[p_n(x,y,\Delta z_n) \otimes \psi_n(x,y)] \tag{3.8}$$

where $\otimes$ represents a convolution. The initial wave function $\psi_0(x,y)$ is the probe wave function in STEM, which is given by equation (3.3).

It is important to limit the spatial frequencies present in both the propagator function and the transmission function otherwise artefacts can enter into the calculation. The propagator and transmission functions should therefore be limited to 2/3 of the maximum spatial frequencies present and also be cylindrically symmetric [Self 1983, Kirkland 1987]. Table 3.1 gives the idea how this method works with the computing.

Table 3.1 Steps for simulations of STEM images of thick specimen [Kirkland 1998]

Step 1 Divide the specimen into thin slices.
Step 2 Calculate the projected atomic potential $v_{zn}(\mathbf{x})$ for each slice and symmetrically bandwidth limit them.
Step 3 Calculate the transmission function $t_n(\mathbf{x}) = \exp[i\sigma\, v_{zn}(\mathbf{x})]$ for each slice and symmetrically bandwidth limit each to 2/3 of its maximum to prevent aliasing.
Step 4 Calculate the probe wave function $\psi_p(\boldsymbol{x}, \boldsymbol{x}_p)$ at position $\mathbf{x}_p$.
Step 5 Recursively transmit and propagate the probe wave function through each slice $\psi_{n+1}(x, y) = P_n(x, y, \Delta z_n) \otimes [t_n(x, y)\psi_n(x, y)]$ using FFT. Repeat until the wave function is all the way through the specimen
Step 6 Fourier transform the transmitted wave function to get the wave function in the far field (diffraction plane)
Step 7 Integrate the intensity (square modulus) of the wave function in the diffraction plane including only those portions that fall on the detector. This is the signal for one point or pixel in the image.
Step 8 Repeat step 4 through step 7 for each position of the incident probe $\mathbf{x}_p$

3.6.2 Frozen phonon method

The frozen phonon method [Kirkland 1998] was developed as a means of including TDS effects into multislice simulations for HAADF image simulation. The word "frozen" in the term was originate from the concept that electrons accelerated to energy of ≥ 100kV will pass through the specimen in a time much shorter than the period of even one thermal vibration (phonon) of the lattice. Thus, whilst the lattice is in constant thermal vibration, each electron will see a lattice that is essentially frozen as it transits the sample. With each electron seeing a different phonon configuration, multiple multislice calculations can be carried out for different thermal displacements of the atoms, and the resultant intensity in the detector plane is summed over the different configurations [Koch 2002] with the detector geometry, and this calculation repeated for all the probe positions in the image. With frozen phonon method, several multislice calculations (generally in the range 10-100) are required for each probe position in order to average effectively over the thermal lattice displacements.

The frozen phonon multislice method was chosen over other methods (such as the use of an absorption potential) as it accurately includes the effects of electron re-scattering. The effects of electron re-scattering becomes important as the thickness of the sample increases and if not included can result in calculation errors.

In practice, specimens are almost always thick enough for multiple electron scattering, therefore any simulation method for ADF STEM has to explicitly consider the effect of dynamical scattering of the probe and also the contribution of the thermal diffuse scattering (TDS). A summary of methods dealing effectively with these two issues will be described below.

3.6.3 QSTEM

QSTEM is a computational software package developed by Prof. C.T. Koch for quantitative (HAADF-) STEM and HRTEM simulations. The computer code is based on the multislice algorithm but with thermal diffuse scattering (TDS) included via the frozen phonon method [http://www.christophtkoch.com/stem/]. Key features of this program are listed below:

1. Potential slicing works for arbitrary samples (e.g. nonperiodic and periodic samples) due to the advantages of multislice method. The projected potential of the whole model is calculated on a fine grid, then the 3D potential is sliced and integrated within each slice.
2. Image computation can be carried out with any orientation by just setting suitable tilting angles for the whole model rather than only shifting the slices by certain amount to each other, as was done in some older and cruder codes.
3. Suitable atomic scattering factors are chosen, which are accurate to the large angles needed for STEM simulations.

In this work, the general set up for QSTEM image simulations were carried out using the following conditions, chosen to provide a reasonable match to the experimental conditions: 100 kV accelerating voltage, 30 mrad convergence angle and a slight spherical aberration of –1 μm with zero defocus. The detectors were simulated with the parameters used in the SuperSTEM experiments of 0 - 5 mrad for the bright field detector and 100-185 mrad for the high angle annular dark field detector. Slices of

half a primitive unit cell in thickness (i.e. 1.98 Å) were used, with the atoms centred in each slice. The frozen phonon method was used to give an average over 30 phonon configurations. The effect of a finite source size was simulated by convolution of the simulated images with a 0.7 Å Gaussian function.

3.7 Density Functional Theory

The properties of solids naturally fall into two categories determined, respectively, by electronic ground state and by electronic excited states [Martin 2004]. The stable structure of solids is generally classified in terms of the electronic ground state, which determines the bonding of nuclei. Therefore, the ground state of the electrons is an important part of electronic structure. The ground state energy can be calculated directly by solving the Schrödinger equation, which involves searching all possible (3N dimensional) wavefunctions for the one that minimizes the total energy. However, the computational cost is very high and the accurate solutions require a very flexible description of the wavefunction's spatial variation, i.e. a large basis set is required which also adds to the expense for practical calculations. An alternative method of solving the Schrödinger equation is using density functional theory (DFT) since the ground state charge density ρ uniquely determines the Hamiltonian operator with $E(\rho)$ being the ground state total energy functional [Hohenburg and Kohn 1964], thus, the ground state properties are uniquely determined by the ground state density. Indeed, the present-day calculations using DFT that attempt to make "first principles" or *"ab initio"* predictions for the properties of condensed matter and large molecular system are based on the approach developed by Kohn and Sham in 1965 [Kohn and Sham 1965]. This Kohn-Sham approach has replaced the difficult interaction with many-body system by some chosen independent-particle system that incorporates the effects of exchange and correlation among the particles. In this case the Schrödinger equation can be written as (the well-known Kohn-Sham equation):

$$\left[-\frac{\nabla^2}{2} + V_{KS}[n](\vec{r})\right]\psi_i(\vec{r}) = E_i\psi_i(\vec{r}) \qquad (3.9)$$

with $V_{KS}[n]$ represents the Kohn-Sham potential that has a functional dependence on the electron density, n, and can be expressed as a sum of the external potential (normally the potential generated by the nuclei), the Hartree term and the exchange and correlation potential (xc):

$$V_{KS}[n](\mathbf{r}) = V_{ext}(\mathbf{r}) + V_{Hartree}[n](\mathbf{r}) + V_{xc}[n](\mathbf{r}) \quad (3.10)$$

Thus, the problems of solving Schrödinger equation are simplified to the calculation of ground state electron density and V_{KS}. For V_{KS}, the most difficult part is the contribution of the exchange-correlation. A widely used approximation is called generalized-gradient approximations (GGAs), which defines that the exchange-correlation energy functional E is not only dependent on the local electron density n as in the cruder local density approximation, but also depends on its gradient ∇n.

To calculate the total energy of solids, a plane-wave expansion of the Kohn-Sham wave-functions is very useful, as it takes advantage of the periodicity of the crystal and easy to calculate. However, for a finite system, solving the Kohn- Sham equation needs a large number of plane-waves as the electronic density is concentrated on a small fraction of the total volume of the super-cell. On the other hand, the valence wave-functions of the large Z atoms oscillate strongly in the vicinity of the atomic core due to the orthogonalization to the inner electronic wave-functions. To describe these oscillations also requires a large number of plane-waves, increasing the computational expense for the calculation of the total energy. However, the inner electrons are almost inert and are not significantly involved in bonding. This suggests that the strong Coulomb potential of the nucleus and the effects of the tightly bound core electrons can be replaced by a modified effective potential acting on the valence electrons. This idea is called the pseudo-potential approximation. One goal of pseudopotentials is to create pseudofunctions that are as “smooth” as possible to describe valence properties to a given accuracy. There are a variety of approximations based on pseudopotentials, such as norm-conserving pseudopotential [Hmann 1979], ultrasoft pseudopotential [Vanderbilt 1990] and more recent developed projector-augmented wave (PAW) [Blöchl 1994] method, which is now adopted quite widely, to conduct a better computational efficiency and accuracy. Details of these approaches can be found in related papers and will not be listed here as the DFT calculations for the nanorods (Chapter 4) were conducted by our external collaborators, and they are quoted in this work to provide deeper insights into the structure and properties of the nanorods.

The DFT calculations relating to this work are performed by Dr S.M. Selbach (NTNU, Norway) whilst on sabbatical in the group of Prof. N. Spaldin in Zurich,

Switzerland, using the program called *Vienna Ab-initio Simulation Package*, known as VASP [Kresse 1996, 1999], using the projector-augmented wave method. The set up are as follows: The spin polarized generalized gradient approximation GGA with the Dudarev approach was used for treating on-site correlations of the Fe 3*d* electrons with a *U*eff of 4 eV. Standard PAW potentials of Bi, Ti, Fe and Nd_3 potential supplied with VASP were used. . A 336 atom $Nd_4Bi_{66}Ti_2Fe6_2O_{202}$ supercell was constructed to model the Nd rod precipitates in a BiFeO3 matrix. A 1x1x3 G-centred *k*-point mesh was used to sample the Brillouin zone of the supercell, and the plane-wave cutoff energy was set to 500 eV. More details can be found in the supporting material of our published paper [MacLaren 2013].

References:

http://www.christophtkoch.com/stem/

http://www.er-c.org/methods/software.htm

Blöchl, P. E., **(1994)** Projector augmented-wave method, Phys. Rev. B**, 50**, (24), 17953-17979.

Bosman M., Watanabe M., Alexander D. T. L. , Keast V. J. , **(2006)** Mapping chemical and bonding information using multivariate analysis of electron energy-loss spectrum inages, Ultramicroscopy **106**, 1024-1032.

Burke M. G., Watanabe M.,Williams D. B., Hyde, J. M., **(2006)** Quantiative characterization of nanoprecipitates in irradiated low-alloy steels: advances in the application of FEG-STEM quantitative microanalysis to real materials, J. Mater. Sci., **41**: 4512-4522.

Cowley J. M. and Moodie A. F., **(1957)** The scattering of electrons by atoms and crystals. 1. a new theoretical approach, Acta Cryst. **10**, 609.

Hamann D. R., Schluter M., Chiang C., **(1979)** Norm-conserving pseudopotentials, Phys. Rev. Lett. **43**, 1494–1497.

Houben L., Thust A., Urban K., **(2006)** Atomic-precision determination of the reconstruction of a 90 degrees tilt boundary in $YBa_2CU_3O_7$-delta by aberration corrected HRTEM, Ultramicroscopy **106**, 200-214.

Jolliffe I.T., **(2002)** Principal Component Analysis, second ed., Springer, New York.

Kirkland E. J., **(1998)** Advanced Computing in Electron Microscopy, New York, Plumn.

Kirkland E. J., Loane R. F., and Silcox J., **(1987)** Simulation of annular dark field stem images using a modified multislice method, Ultramicroscopy **23**, 77-96.

Koch C., **(2002)** PhD Thesis: Arizona State University.

Kohn W. and Sham L. J., **(1965)** Self-consistent equations including exchange and correlation effects, Phys. Rev. **140** (4A), 1133–A1138.

Kresse G. and Furthmuller J., (**1996)** Efficient iterative schemes for ab initio total-energy calculations using a plane-wave basis set, Phys. Rev. B**, 54** (16), 11169-11186.

Kresse, G. and Joubert, D.; **(1999)** From ultrasoft pseudopotentials to the projector augmented-wave method, Phys. Rev. B**, 59** (3), 1758-1775.

Levin I., Karimi S., Provenzano V., Dennis C. L., Wu H., Comyn T. P., Stevenson T. J., Smith, R. I., Reaney I. M., **(2010)** Reorientation of magnetic dipoles at the antiferroelectric-paraelectric phase transition of $Bi_{1-x}Nd_xFeO_3$ (0.15 <= x <= 0.25), Phys. Rev. B., **81,** (2), 020103.

MacLaren I., Wang L. Q., Schaffer B., Ramasse Q. M., Craven A. J., Selbach S. M., Spaldin N. A., Miao S., Kalantari K., Reaney I. M., **(2013)** Novel Nanorod Precipitate Formation in Neodymium and Titanium Codoped Bismuth Ferrite, Adv. Func. Mater., **23,** (2), 683-689.

Martin R. M., **(2004)** Electronic Structure: Basic theory and practical methods, Cambridge university press, ISBN 0 521 782850 6.

Molinowski E.R., **(2002)** Factor Analysis in Chemistry, third ed., Willey New York.

Sanchez A. M., Galindo P. L., Kret S., Falke M., Beanland R., and Goodhew P. J., **(2006)** An approach to the systematic distortion correction in aberration-corrected HAADF images, J. Microsc., **221** (1), 1-7.

Schaffer B., Grogger W. , Kothleitner G., **(2004)** Automated Spatial Drift Correction for EFTEM Image Series, Ultramicroscopy **102**/1: 27-36.

Self P.G., O'Keefe M. A., Buseck P. R. and Spargo A. E. C., **(1983)** Practical computation of amplitudes and phases in electron-diffraction, Ultramicroscopy **11,** 35.

Vanderbilt D., **(1990)** Soft self-consistent pseudopotentials in a generalized eigenvalue formalism, Phys. Rev. B, **41**, 7892-7895.

Watanabe M. *et al*., **(2005)** Atomic-level analytical electron microscopy of diffusional phase, Proc. Inter. Conf. on Solid-Solid Phase Transformations in Inorganic Materials 2005 - **2**, 431-442.

Watanabe M. *et al.*, **(2007)** Applications of Electron Energy-Loss Spectrometry and Energy Filtering in an Aberration-Corrected JEM- 2200FS STEM/TEM, Microscopy and Microanalysis, **13** Suppl. 2: 1264-1265.

Chapter 4 Characterisation of nanorod precipitates

4.1 Introduction

In recent years, there has been tremendous research activity on perovskite $BiFeO_3$ (BFO) because of its room temperature multiferroism [Catalan 2009], as well as for the benefit of global enviornment since it is lead-free. Perhaps of equal interest are its ferroelectric properties: It shows one of the largest known electric polarizations (~90 μC cm^{-2}) and has a small (~2 eV) band gap which is likely responsible for recent reports of conducting domain walls [Seidel 2009] and enhanced photovoltaic behaviour [Choi 2009]. However, there are critical problems that limits its application. 1) Single phase samples are difficult to synthesis due to the metastable state of BFO and volatilization of Bi_2O_3. 2) High conductivity that hampers the exploitation of the FE. 3) Difficult to obtain the linear ME effect due to the space - modulated spin structure [Yuan 2006]. Chemical modification of $BiFeO_3$ is proving to be a valuable route to solving these problems. This has been evidenced by the following research. Murashov *et al.* [Murashov 1991] reported that doping of BFO with La can suppress the space modulated spin structure thus stabilizing the collinear AFM structure. They observed a linear *i.e.* first order magnetoelectric effect in $(Bi_{0.7}La_{0.3})FeO_3$. Later on, other studies have shown a similar result with BFO doped by Nd or Sm [Yuan 2006, Das 2007, Fujino 2008, Kan 2010, Levin 2010], often resulting in a phase transformation from a rhombohedral *R3c* structure to an orthorhombic antipolar $PbZrO_3$ (PZ)-like *Pbnm* structure. In addition to the suppression of the SMSS, part substitutions of Bi^{3+} can also minimise the occurrence of defects such as oxygen or bismuth vacancies, together with the formation of secondary phases like $Bi_2Fe_4O_9$ or $Bi_{25}FeO_{39}$ during the synthesis of BFO [Yuan 2006, Zhang 2006, Das 2007]. However, the leakage current is still too high for the A-site doped BFO to be used as a dielectric or ferroelectric. Some reports have pointed out that A and B site co-doping can reduce the conductivity. Yu *et al.* [Yu 2008] have reported that the conductivity with (less than 3%) La^{3+} and V^{5+} co-doped BFO was reduced markedly and the leakage current was more likely to be affected by charge defects (e.g. V_o^{2+}, V_{Bi}^{3-}) than by secondary phases. Cui *et al.* [Cui 2010] have also observed the improvement of dielectric permittivity with La and Ti co-doped BFO

($Bi_{0.85}La_{0.15}Fe_{0.9}Ti_{0.1}O_3$) due to the significant reduction of oxygen vacancies. In 2011, for the first time, Kalantari *et al.* [Kalantari 2011] found that Ti^{4+} doping up to 10% reduced the conductivity of PZ-structured $Bi_{0.85}Nd_{0.15}FeO_3$ (BNFO) massively. Additionally, they also discovered that < 5% Ti on the B-site did not change the PZ-like structure with antipolar order but above this concentration, the antipolar order is gradually destroyed, as judged by the appearance of superlattice spots in electron diffraction patterns. In contrast to a linear decrease in T_N with increasing Ti concentration due to the dilution of antiferromagnetic ordering by the replacement of magnetic Fe^{3+} ions with non-magnetic Ti^{4+} ions, T_C shows a non-linear trend with increasing Ti content, which indicates that more complex processes may be going on as regards the effect of Ti doping on the structure and thus on the polarisation ordering. To further understand what is going on with this phenomenon, a series of Ti doped BNFO samples including: $Bi_{0.85}Nd_{0.15}Fe_{0.9}Ti_{0.1}O_3$ (BNFT-15_10), $Bi_{0.875}Nd_{0.125}Fe_{0.97}Ti_{0.03}O_3$ (BNFT-12.5_3) and $Bi_{0.9}Nd_{0.10}Fe_{0.97}Ti_{0.03}O_3$ (BNFT-10_3) were investigated using the atomic-resolution scanning transmission electron microscope (STEM) with a combination of conventional imaging and EEL SI. These investigations showed a surprisingly complex range of Nd-rich nanorod precipitates only 2 atomic columns wide (section 4.2). Based on the information from the quantitative analysis of HAADF images and atomic resolution chemical maps from the atomic resolution EEL SI (section 4.3), the 3D model structure of the nanorods is elucidated by first principles calculations, followed by confirmation using QSTEM simulation (section 4.4). Following this, the properties of nanorods and their effect on the perovskite matrix are discussed in section 4.5. Finally, conclusions are made in section 4.6.

4.2 TEM Imaging of The Nanorods and Their Connection to The Domain Structure of $Bi_{0.85}Nd_{0.15}Fe_{0.9}Ti_{0.1}O_3$

Figure 4.1(a) shows a dark field TEM image and its related diffraction patterns (inserted) along the [001] direction of one area of interest, taken by the SIS Megaview III camera on the FEI Tecnai T20 as described in Chapter 2. The dark field image of Figure 1(a) also shows 2 diagonal boundaries across the field of the image, and in all regions to the top left of the lowest boundary there is a highly unusual contrast in the material of apparently randomly scattered white dots. Areas with such dotty contrast

can be easily distinguished from other areas by examination of the diffraction patterns. The top left area shows diffraction pattern with ¼ spacing spots along [110] directions, as shown in the left inset of Figure 4.1(a) and these quadrupled superlattice reflections between the strong perovskite sublattice reflections are characteristic of an [001] orientation of the $PbZrO_3$-like structure with unit cell of $\sqrt{2}a_c \times 2\sqrt{2}a_c \times 4a_c$ as Karimi *et al.* has reported for the structure of 15% Nd doped BFO [Karimi 2009], even if they are somewhat streaky and diffuse. The quadrupling is caused by the tilting system of oxygen octahedra along the c-axis, thus can only be detected by electron diffraction. Below and to the right of the bright line, a different orientation is observed corresponding to [100] or [010] of the primitive pseudotetragonal perovskite structure ([210] or $[2\bar{1}0]$) of the orthorhombic $PbZrO_3$ structure); this is a simple cubic diffraction pattern with no extra ordering spots and the only unusual feature is some streaking along a [001] direction. Thus, the diagonal bright line delineates a domain boundary between two orientations of the unique [001] axis; i.e. a domain boundary of the antiferroelectric structure. More details about this and similar boundaries will be discussed in chapter 5. Further investigation using HRSTEM with HAADF imaging reveals that these unusual features in dark field images are actually defects with a clearly recognizable pattern of 8 atom columns (where there would be 9 in a perfect perovskite) with two columns of heavy (i.e. bright) atoms in the centre surrounded by three other columns of heavy atoms on each side of it as seen in Figure 4.1(b). The bright spots show the positions of the A-site Bi/Nd columns and the weaker spots the B-site Fe/Ti columns. The defects are approximately randomly spaced in the (001) plane. Similar features are observed throughout the sample. As will be discussed in section 4.3.3, these defects turned out to be nanoscale rod-shaped precipitates (hence referred to as nanorods) and they tend to be orientated with the long axis always along the [001] axis of the orthorhombic $PbZrO_3$-like crystal structure. It is worth pointing out that some other defects (as some of them have been circled) appear somewhat different with weaker contrast than the clear 8 -atom pattern, and the origin of this contrast is discussed in sections 4.3.3 and 4.4.3.

In order to understand these defects in detail, we first applied techniques for quantitative STEM imaging from two orthogonal projections combined with chemical mapping using EEL SI to provide the data required for the development of a three dimensional model of these defects.

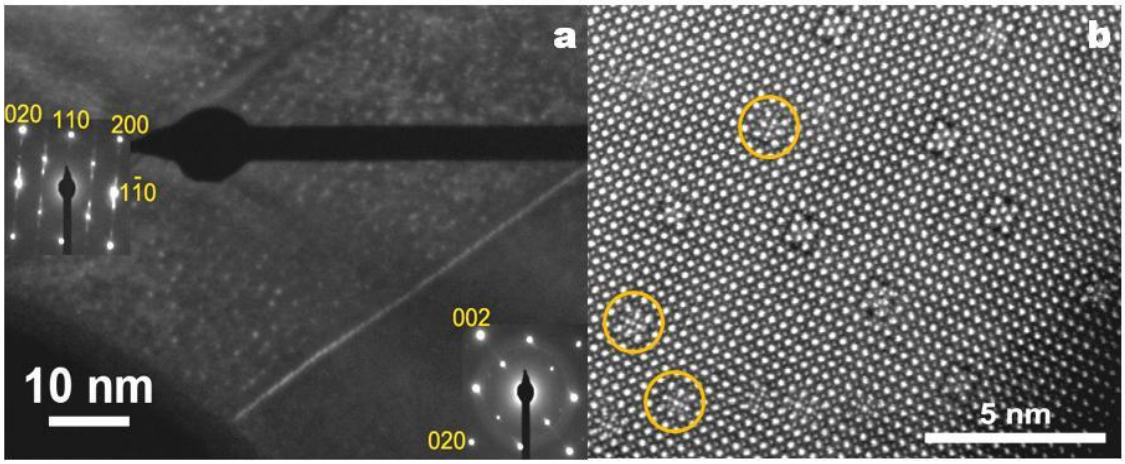

Figure 4.1. (*a) Dark field image of one area examined by HRSTEM; diffraction patterns insets show the crystal orientation to either side of the domain boundary, which appears as a bright diagonal line. (b) HAADF image of nanorod precipitates in an end-on orientation.*

4.3 Quantitative Analysis of Atomic Resolution STEM Imaging and Chemical Mapping of The Nanorods From $Bi_{0.85}Nd_{0.15}Fe_{0.9}Ti_{0.1}O_3$ Sample

4.3.1 Quantitative analysis of the atom positions from HAADF STEM images

To minimize the effect of sample drift and beam damage, images for quantitative evaluation were acquired by repetitive scanning of the same area in a video acquisition mode in SuperSTEM2 using short pixel dwell times of 5µs. These were then processed by first manually examining the frame stack and discarding any frames with obvious serious defects such as missing lines or notable distortions. Following this step is the alignment of the remaining images using the SDSD plugin for Digital Micrograph [Schaffer 2004] and peak positions were then extracted using the iMtools software package as discussed in chapter 3. The interpolated peak positions were then exported to a spreadsheet for further data processing including distortions correction, averaging, and 3D model building.

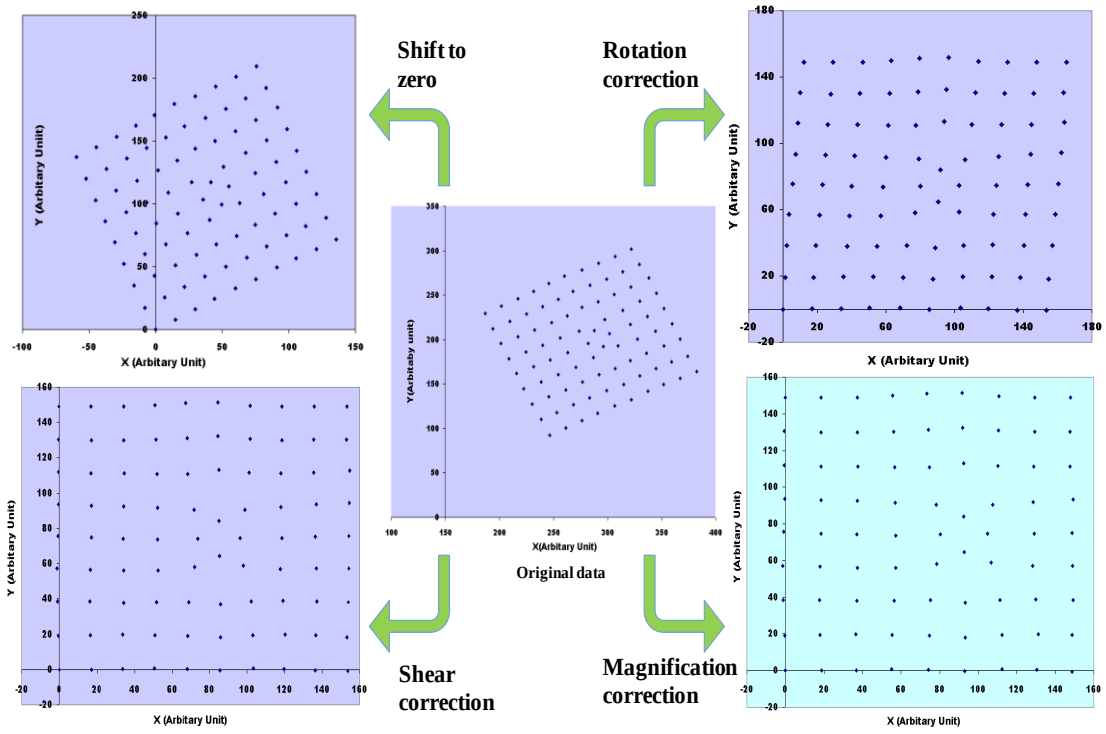

Figure 4.2. *A typical procedure for linear distortions correction, including shifting peak positions to zero, rotation correction, shear correction and magnification correction.*

The cell parameters of a closely related composition with the same crystal structure, $Bi_{0.85}Nd_{0.15}FeO_3$, were Rietveld-refined from XRD and neutron powder diffraction data as part of previous works [Karami 2009, Levin 2010]. Results from these refinements showing that the structure is of $PbZrO_3$ - type orthorhombic, with cell parameters of a = 5.5959 Å, b = 11.2399 Å, c = 7.8076 Å. According to the $PbZrO_3$ - type structure that has unit cell of $\sqrt{2}a_c \times 2\sqrt{2}a_c \times 2a_c$ (a_c is the cell parameter of the primitive perovskite) rather than $\sqrt{2}a_c \times 2\sqrt{2}a_c \times 4a_c$, since the further cell doubling is caused by the octahedral tilting which is not detectable to XRD or neutron power diffraction, and reducing this orthorhombic cell to a pseudotetragonal cell, cell parameters of a ≈ b ≈ 3.965 Å, c = 3.904 Å can be obtained. Since the nanorod precipitates always lie along [001], then the cells in the [001] direction can be assumed to be square on average and oriented with a side of 3.965 Å (see Figure 4.3). Any linear distortions likely caused by the imperfection in the scanning system were then corrected to leave a square image of side 3.965 Å, in a similar manner to that used for the quantitative analysis of the atomic structure of incommensurate La - doped $Pb(Zr,Ti)O_3$ [MacLaren 2012]. Figure 4.2 shows the typical procedure of linear distortion correction

for one of the defects, which includes shifting the interpolated peak positions to zero, rotation correction, shear correction and magnification correction to make the crystal cells in the [001] direction to be square. All the measurement of these corrections was performed using patches of perfect perovskite structure between the defects by performing least squares fitting to determine the gradients and spacings of rows of peak positions, and then converting the fit parameters to correction matrices to apply to the dataset (i.e. rotation, shear, and magnification and anisotropic expansion matrices). The matrix used for the rotation correction is formed by using the averaged rotation gradient from the rows of peaks below and above the defect. The matrix for shear correction was constructed from the averaged gradient of the columns of peaks which should be vertical on either side of the defect. In general, the averaged gradient of the columns of peaks would result in the angle value of ~1.50 for shear corrections (about 86 degrees with respect to horizontal axis).

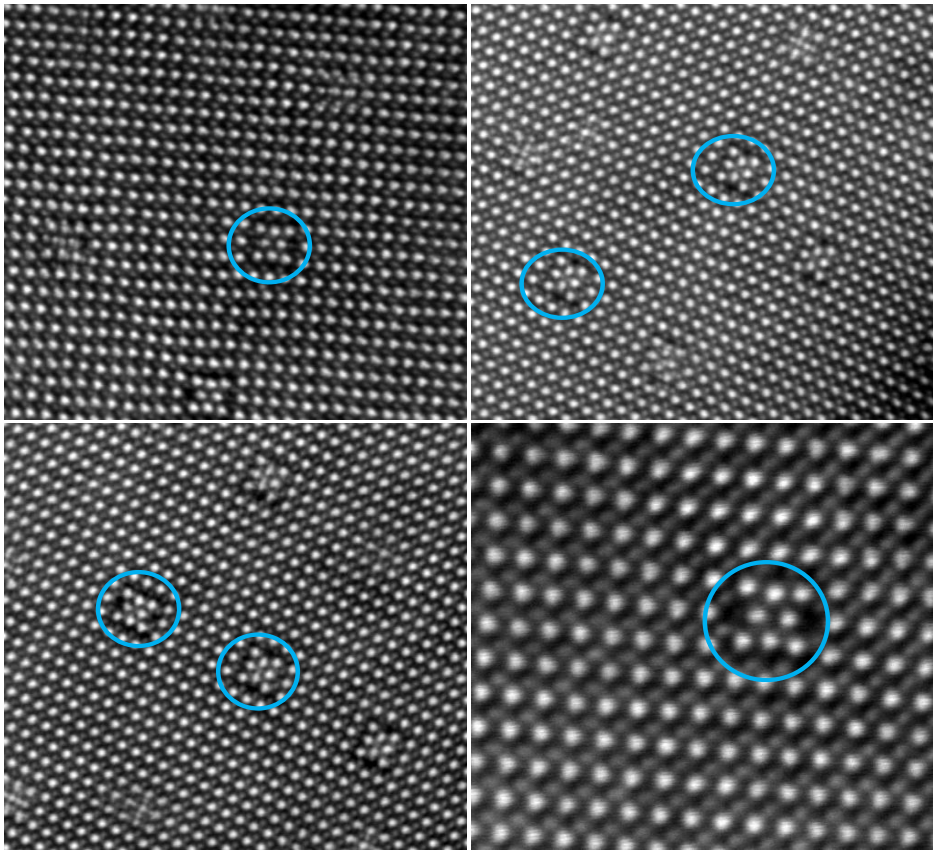

Figure 4.3. *HAADF images showing six defects used for quantifying atomic positions. Scale bars can be worked out by the distance between two nearest bright A-site spots of the bulk matrix, which is about 3.965Å.*

Figure 4.3 shows images of six defects that were used for the quantitative analysis of atom positions. All of the atomic positions from these defects, corrected and rotated into the equivalent orientation (since there are two possible orientations, at 90° to one another) are overlaid in Figure 4.4 (a) showing that all defects were extremely similar in structure. These atomic positions were then averaged in the following way. It was assumed that the defect had a plane symmetry of 2mm as marked on Figure 4.4 (a) and therefore all symmetry equivalent points were averaged, after the application of suitable symmetry operations to produce a symmetry-reduced list of atomic positions for the A-sites in the precipitate. These are then plotted, together with 3σ error bars (99.7% confidence intervals) on all atom positions in Figure 4.4 (b). The average atomic positions and standard deviations are listed in Table 4.1.

Table 4.1. Averaged atomic positions for the defect after reduction to *2mm* symmetry

Label	***x (Å)***	***σ_x (pm)***	***y (Å)***	***σ_y (pm)***
1,1	0.06	13	-0.01	17
2,1	4.04	12	0.04	15
3,1	7.99	13	0.06	14
4,1	11.90	14	0.03	11
1,2	0.03	15	3.98	16
2,2	4.10	14	4.16	9
3,2	8.08	17	4.24	9
4,2	11.90	17	4.28	10
1,3	-0.10	14	7.94	14
2,3	4.07	11	8.08	11
3,3	8.46	8	8.80	9
4,3	11.90	7	9.21	7
1,4	-0.20	20	11.90	17
2,4	3.86	12	11.90	10
3,4	9.87	9	11.90	8

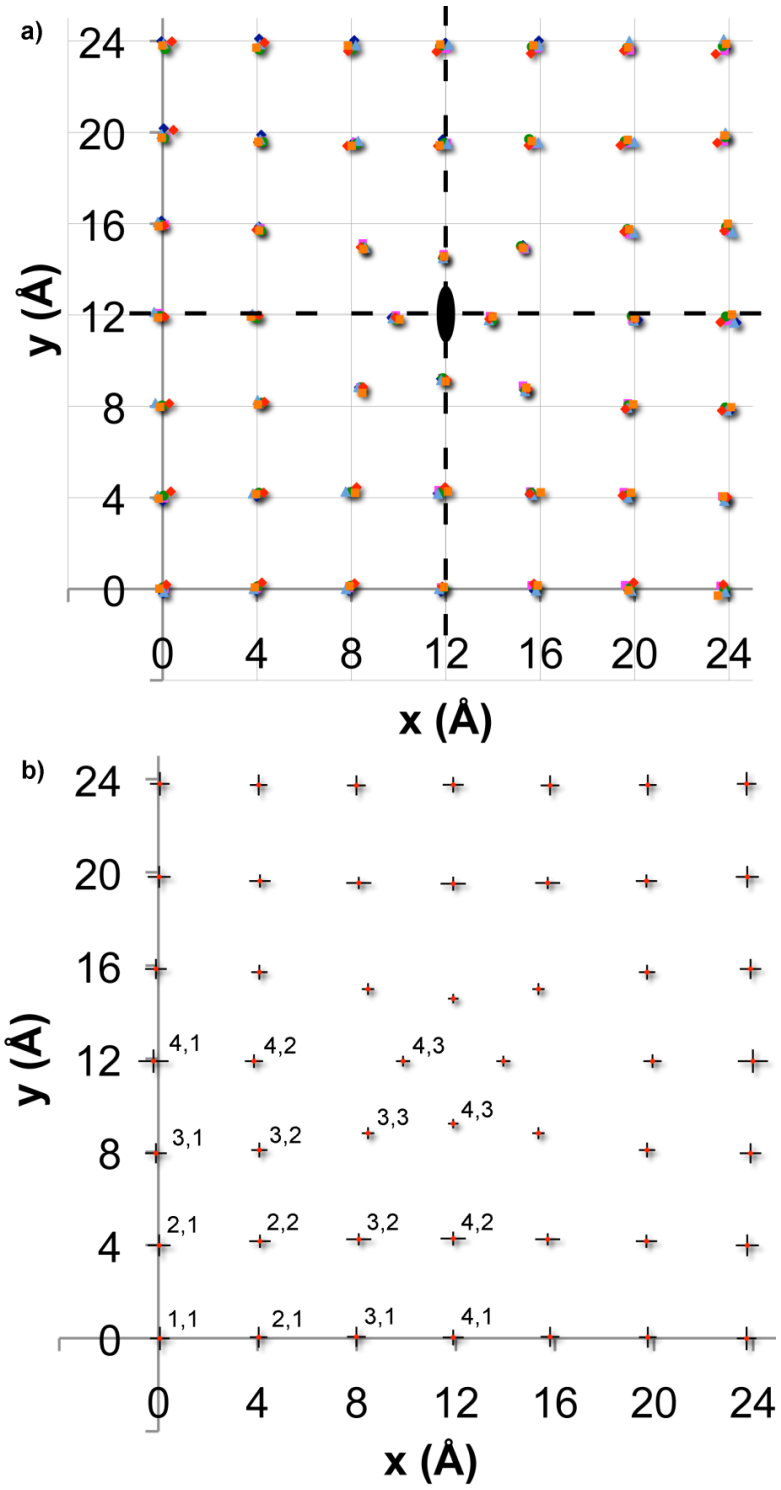

Figure 4.4. *Corrected A-site positions for six defects: a) the positions for each of the six defect images, each in a different colour, together with a symmetry markers for the proposed 2mm plane symmetry of the defect; b) averages for each position after averaging all symmetrically equivalent positions to generate each data point, error bars are 3* σ *to make them clearly visible.*

4.3.2 Chemical mapping of the nanorods from the top view

To determine the chemistry of the nanorods, atomic resolution chemical mapping technique was carried out by using EEL SI. The full procedure for generation the maps for Figure 4.6 are shown in Figure 4.5 and a similar procedure was used throughout this thesis for all other elemental maps. Prior to creating any maps, the spectrum image was processed using PCA to remove random noise, as described in chapter 3, and the reconstructed spectrum image was created from just the first 20 components from the PCA analysis. Following this, maps were created using relatively wide energy windows for the elemental maps with the parameters listed in Table 4.2; this was done to maximize signal to noise ratio in the maps and did not result in any strange contrast inversions or loss of contrast [Allen 2010]. Background fitting windows were kept as wide as possible to avoid the effects of noise in individual channels of the spectrum, whilst avoiding disturbance from oscillations due to the previous core loss edge, and were typically as listed below.

Table 4.2. Typical Mapping parameters using in creating the maps

Ionization edge	Signal Window		Background Window	
	Start (eV)	End (eV)	Start (eV)	End (eV)
Fe $L_{2,3}$	707.4	830.6	599.5	703.1
Nd $M_{4,5}$	978.8	1165.0	771.0	970.5
Ti $L_{2,3}$	456.8	526.8	419.6	453.9
O K	529.6	579.3	490.3	524.6

Careful examination with the intensity distribution from carbon map, it is noticeable that the intensity varies from atom columns to columns, indicating that the total intensity entering the spectrometer depends on the elastic scattering. Therefore, the elemental maps should be normalised by the corresponding total intensity map to give a unbiased intensity distribution in order to give quantitative information from elemental maps, especially for oxygen maps if we want to extract oxygen information from the matrix as a reference to the defects. This is based on the assumption that the number of

oxygen in pure oxygen columns O-O should have the same number as that in the columns mixed with B-site atoms Fe/Ti-O, thus the intensity distribution around the heavy A-site atom columns should be the same within the matrix. Ideally this would be carried out using the integrated low-loss signal [Scott 2008]. However, it was not possible to record this simultaneously in the current experimental set-up in SuperSTEM2. The alternative is to use another signal in the spectrum, which should also correlate to the total signal into the spectrometer; here the carbon K edge intensity is used. The carbon deposited onto the samples to prevent charging is thought to be fairly evenly deposited, at least at the nanoscale. The background subtracted carbon signal from a fixed number of carbon atoms per unit area is directly proportional to the low loss intensity and thus the carbon K-edge signal should correlate very well with the total signal entering the spectrometer. Although the contrast variation in the carbon map in Figure 4.5 is noticeable, the variation is still pretty weak with which the contrast only drops to about 75% of the maximum intensity on the heaviest columns. Therefore, this normalisation does not change the maps strongly even if the contrast from the maps to be normalised is not very high. However, the intensity distribution of normalised oxygen map still varies. Therefore, this procedure wouldn't give any further quantitative information regarding oxygen number in columns since maybe more complex scattering procedure involved rather than just elastic scattering, but it seems still useful for sharpening the column images slightly for the cations.

As the processed maps still have noise after the normalisation, as well as the effects of scanning defects and drift in acquisition, a weak low pass filter is applied with a diameter of just 3 pixels to smooth out the effects of these slight acquisition defects.

$$\begin{pmatrix} 1 & 1 & 1 \\ 1 & 4 & 1 \\ 1 & 1 & 1 \end{pmatrix}$$

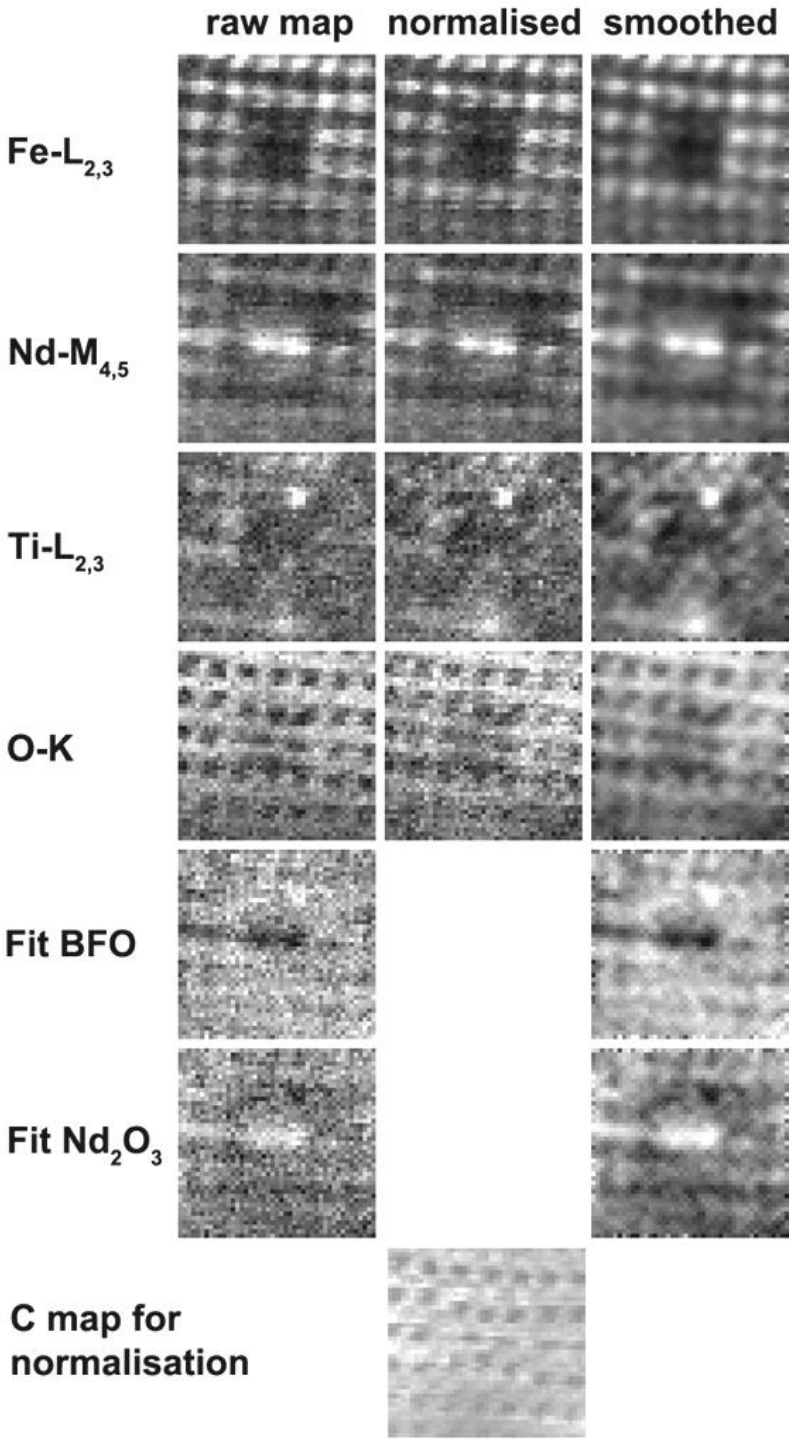

Figure 4.5. *Processing steps involved in creating the maps shown in Figure 4.6: the initial maps are created from a PCA analysed spectrum image using the first 20 components, these are then normalised by division by the carbon map shown to try to normalise them to the total signal entering the spectrometer. Finally, maps are cleaned up by the application of a low pass filter.*

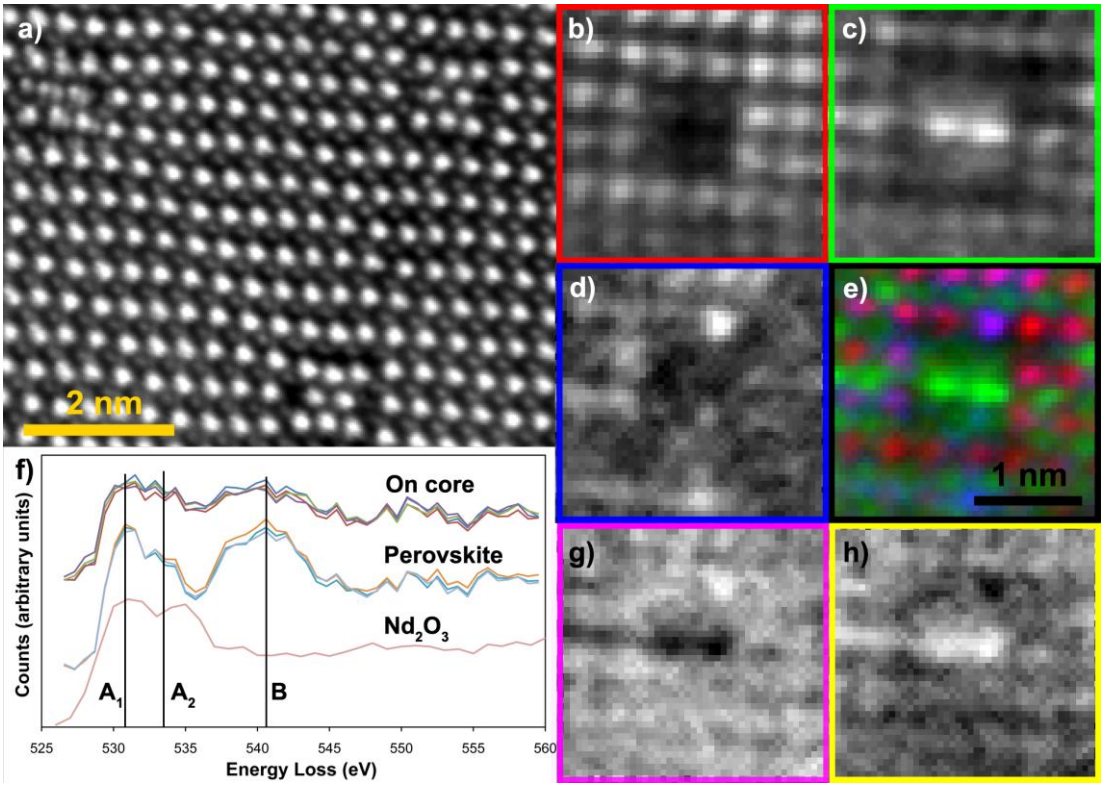

Figure 4.6. *Quantitative imaging and electron energy loss elemental mapping of the nanorods in an end-on orientation; a) HAADF image formed by summing 46 drift-corrected short acquisitions of one area. b) – e) elemental maps created from a EEL SI of one such nanorod: b) Fe map; c) Nd map; d) Ti map; e) RGB map created where red represents Fe, green represents Nd and blue represents Ti; f) O K-edge EEL spectra from the nanorod core, outside the nanorod core and a Nd_2O_3 spectrum for reference; g) MLLS fit coefficient map for the O-K edge shape for bulk perovskite; h) MLLS fit coefficient map for the O-K edge shape for the Nd_2O_3 edge shown in f).*

Figure 4.6 (b) - (e) shows the results of atomic resolution maps for the elemental distribution of Fe, Ti and Nd derived from an EEL SI of one nanorod in "top view" (along [001]) after the whole procedure was done. The EEL SI data show clearly that B-site cations (Fe/Ti) are depleted in the central part of the nanorod and that the two central columns are Nd-rich. Nd is also found in other columns around the nanorod, but in smaller and variable quantities consistent with its alloying with Bi in the matrix; spectrum images of regions without nanorods show a random and non-uniform distribution of Nd on the A sites. In addition, the electron beam tends to spread significantly after channelling along a heavy column for a few unit cells resulting in

significant background signals in both imaging and spectroscopy [Robb 2012]. Thus each atomic column in the spectrum image will also contain unknown contributions from the $BiFeO_3$ matrix and the chemistry therefore cannot be absolutely quantified from the EEL SI. The Ti map (Figure 4.6(d)) shows that at least one column at the edge of the nanorod is enriched in Ti, which matches the result from the side-view EEL SI data for Ti (Figure 4.9). Oxygen maps were also created, but very little information on precise atomic positions in the nanorods can be revealed (Figure 4.5 O-K). This is possibly due to the delocalisation of the excitation of the O-K edge [Allen 2010]. It seems that the nanorods have similar oxygen content in the core of the nanorods to the matrix, but it is difficult to determine the precise locations of oxygen in the nanorods.

Since the EEL SI oxygen maps reveal relatively little about the oxygen distribution, investigations into the oxygen ELNES were carried out to reveal the oxygen local bonding in the nanorods. In Figure 4.6(f) we compared the structure of the O K-edge in the nanorod core using a spectrum summed from a selected 7×7 square of pixels of the spectrum image centred around a Nd column and the same selection size around an expected column position for the oxygen in the perovskite matrix at the top of the image, in each case recording background subtracted O K-edge spectra in these different locations. For comparison a reference spectrum from Nd_2O_3 is also shown [Ahn 1983]. Apparently, the nanorod and matrix spectra are very different from each other. As expected, the spectra from the matrix correspond well to the spectra from bulk doped $BiFeO_3$ (see for instance Saeterli *et al.* 2010). The Nd-rich core, in contrast, gives an A_2 peak of similar height to the A_1 peak and the whole O post-edge region after the A_1 and A_2 peaks is flatter than for the matrix. This is consistent with previously recorded spectra for Nd_2O_3 where the A_1 and A_2 peaks are of similar height and the B peak is weaker, and this suggests that the core of the nanorod is chemically similar to neodymium oxide. To show this local variation visually we next map the local chemistry from the EEL SI using multiple linear least squares (MLLS) fitting. The MLLS maps (see Figure 4.5: Fit BFO, Fit Nd_2O_3 and Figure 4.6(g), (h)) were made using the MLLS function in Gatan Digital Micrograph (Gatan Inc., Pleasanton, CA) using the $BiFeO_3$ perovskite signal integrated from one unit cell at the top of the spectrum image outside the core and using a Nd_2O_3 standard spectrum [Ahn 1983]. By fitting the observed O K edge shape at each point in the spectrum image as a linear

combination of our measured O-K edge profile from the $BiFeO_3$ matrix and a Nd_2O_3 standard electron energy loss spectrum [Ahn 1983], the similarity between the O bonding map of Figure 4.6(h) (for Nd_2O_3) and the Nd elemental map of Figure 4.6(c) confirms the chemical similarity of the nanorod core to Nd_2O_3. The fit coefficient for the $BiFeO_3$ matrix and shows the fit coefficient for the Nd_2O_3 standard are shown in Figure 4.6(g) and Figure 4.6(h), respectively.

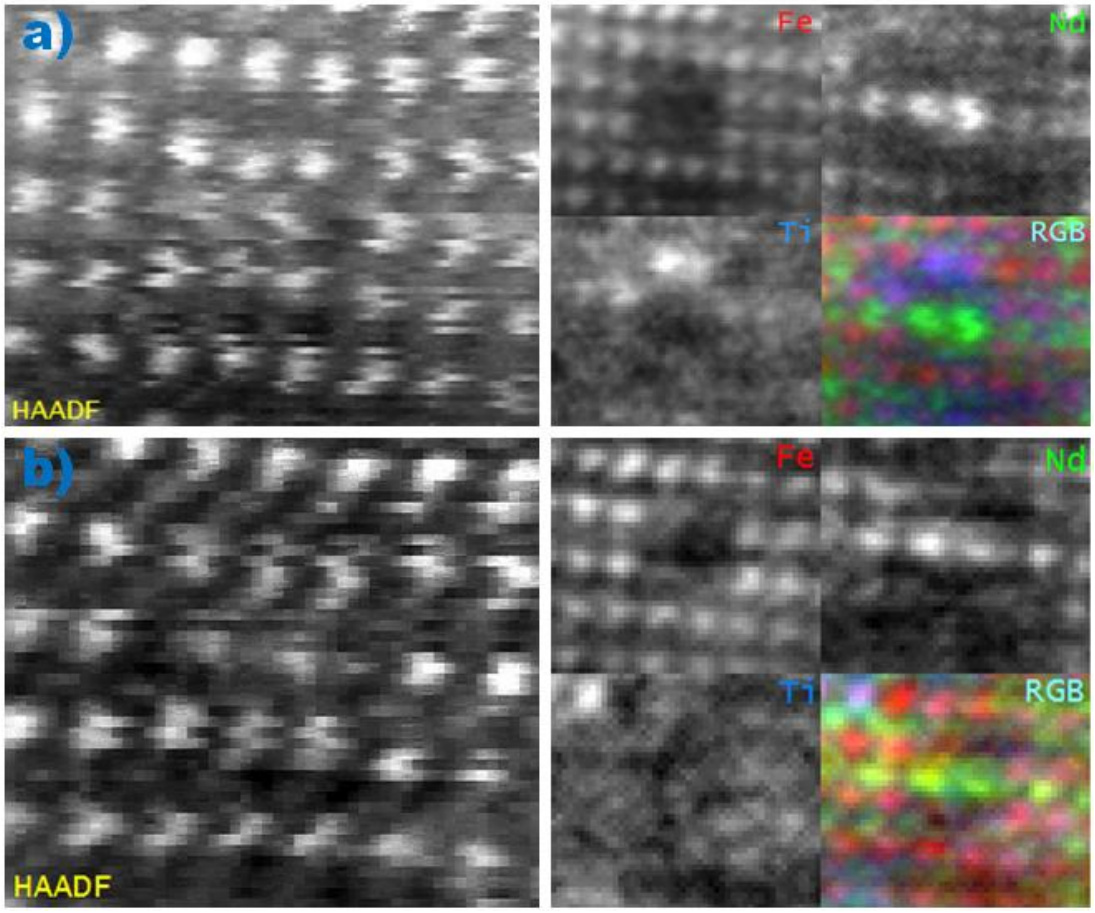

Figure 4.7. *a) Elemental maps from another defect with similar results as in Figure 4.6. b) elemental maps from a defect but overlapped with normal BFO crystal matrix. HAADF images presented in both a) and b) were acquired simultaneously with EEL SI.*

Figure 4.7 shows elemental maps processed with the same procedure used above for another two defects (along [001] direction]). Figure 4.7(a) is from a defect with a thickness spanning much of the specimen while Figure 4.7(b) is from a defect that did not run through the whole thickness of the specimen but overlapped with some normal BFO crystal matrix. Again, the same key features of the nanorods are definitely shown

here, such as Nd_2O_3 in the core with B-site elements (Fe/Ti) depleted but with some Nd atom columns distributed randomly at the surrounding matrix and at least one Ti atom column at the periphery of the core. However, due to the overlapping effect from the normal crystal matrix, alloying of Nd onto Bi columns in the matrix is clearer in the Nd map of Figure 4.7(b) . Also, the contrast in the core of the nanorod for Fe and Ti in Figure 4.7(b) is less than that in Figure 4.7(a) due to the fact that scattering from B-site atoms of the normal matrix below/ above the nanorod enters the detector. More work has been done with more other defects, but they all displayed the same main features as we mentioned here with more or less difference for the columns at the periphery, hence, it is not necessary to list them all here.

4.3.3 Imaging of the nanorods from the side view

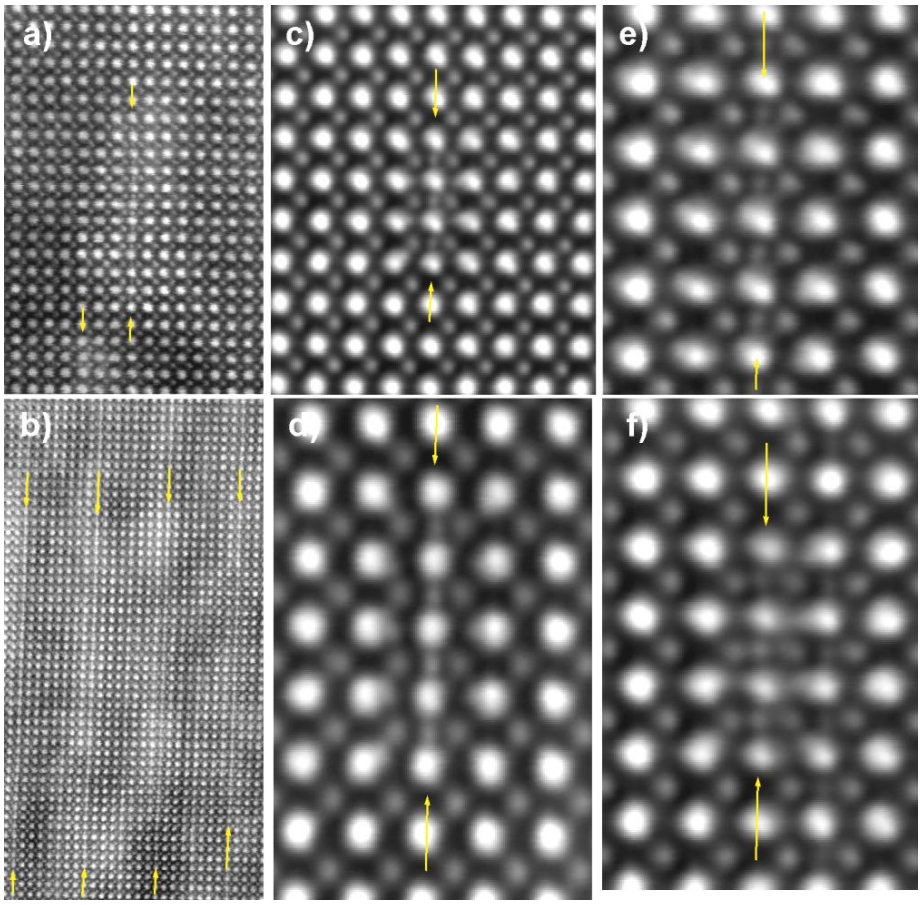

Figure 4.8. *Side views of some different nanorod precipitates (in all cases nanorods are indicated by yellow arrows): a) and b) lower magnification MAADF images, showing strain around the precipitates; c)-f) HAADF images formed by repeat scanning, alignment and summation of multiple scans.*

Figure 4.8 illustrates several HAADF images from areas of samples with the same composition (15% Nd, 10% Ti). The common but characteristic feature in these images is that additional bright columns of atoms (indicated by arrows) lying between the A-site atoms. These delicate features are assumed to be the side-view of the defects, which will be confirmed by the simulations of section 4.4.3. The length of the defects varies in a wide range, from just about 3 unit cells (≈1.2 nm) up to more than 20 unit cells in the case (≈10 nm) in Figure 4.8(b). Considering the scale and the morphology of these defects, they are referred to as nanorods. It is worth to point out that Figure 4.8 (a) and (b) are two images that were taken with MAADF detector. This detector samples both the incoherent scattering seen at the HAADF detector as well as some coherent diffraction seen at lower angles. The result of this is that typical MAADF images have both clearly resolved atomic columns with brightness variations superimposed due to local strain or lattice distortion resulting in increased diffraction contrast. Thus, the highly strained areas around the nanorods are easily seen using MAADF as bright areas and closer inspection reveals the extra columns of atoms between the A-site positions in the centres of these bright areas. Further MAADF images with this strain effect on overall intensity are shown in section 4.5.3 with samples co-doped with lower levels of Nd and Ti.

4.3.4 Chemical mapping of the nanorods from the side view

In order to understand the chemical identity of the atoms in between the A-site positions, EEL SI was performed on 17 nanorods from the side-on view. Maps derived from one of these spectrum images are shown in Figure 4.9 (b)-(e). Figure 4.9 (b) shows the Fe map, which is similar to the matrix and immediately adjacent to the nanorod core. In contrast, the Nd map (Figure 4.9 (c)) shows a clear concentration to some sites in the nanorod core. Finally, the Ti map (Figure 4.9 (d)) indicates a depletion of Ti in the core and a slight enrichment at some sites on the edge of the nanorod, which matches the result of Ti from the end-on data mapping. The three-colour RGB overlay reveals that some of the Nd sites at the nanorod core lie in the same plane as the Fe atoms, and not in the main A-site (Bi,Nd) columns. We conclude, therefore, that the "halfway" positions pointed out previously in the HAADF image of Figures 4.8 and 4.9 (a) are occupied by Nd atoms. However, in the surrounding matrix, the Nd atoms occupy the expected A-site positions.

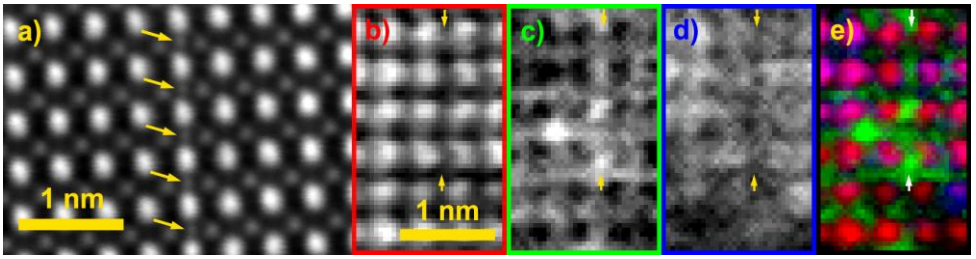

Figure 4.9. *Quantitative imaging and electron energy loss elemental mapping of the nanorods in side-on orientation; a) HAADF image of one such nanorod formed by summing 27 drift-corrected short acquisitions, pairs of Nd atoms along the beam direction are indicated by yellow arrows. b)-e) elemental maps created from a EEL SI of one such nanorod, the nanorod lies between the arrows in all maps: b) Fe map; c) Nd map; d) Ti map; e) RGB map created where red represents Fe, green represents Nd and blue represent Ti.*

4.4 The 3-Dimensional Structure of The Nanorods

Based on the A-site atoms positions we extracted from the HAADF image as described in section 4.3.1 and the atomic resolution elemental mapping results from section 4.3.2 and 4.3.3, we built up an initial 3D model for the structure of the nanorod. However, in view of the fact that the exact positions of the oxygen atoms could not be determined experimentally, next we use density functional theory (DFT) with the GGA plus Hubbard U method to calculate the lowest energy arrangement of the atoms. To confirm the optimized structure, QSTEM simulations were carried out.

4.4.1 The primary 3D model of the structure of the nanorods

The initial model (see Figure 4.10) has 2 columns of Nd ions surrounded by a matrix of bulk-like $BiFeO_3$, which is very distorted close to the Nd core. B-site positions were obtained by averaging its nearest neighbouring A-site positions, presuming that the B-site atoms were in the centre of the A-site octahedral without the consideration of polarization. In accordance with the chemical mapping, Ti ions were then placed in the B-site columns of the matrix $BiFeO_3$ adjacent to the Nd columns. To choose the number of oxygen ions we took the formal charges of Nd^{3+}, Bi^{3+}, Fe^{3+} and Ti^{4+}, and added a stoichiometric number of oxygen ions to maintain charge balance. Initially all the Oxygen's positions were obtained from B-sites positions but arranged

with all the B-sites ions have 6 coordinates. To keep the charge balance, one more O atom column was put in between the two Nd columns.

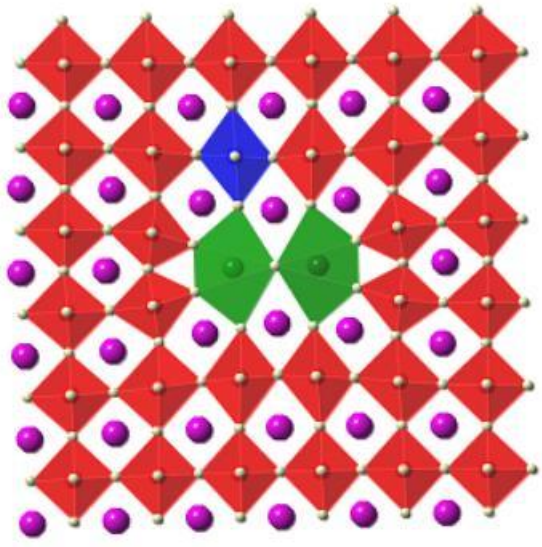

Figure 4.10. *The initial model of nanorods with all the B-sites atoms 6 coordinated.*

4.4.2 Optimum of the 3D structure model by DFT

As the DFT calculations were done by our collaborators at ETH Zürich, more details of the setting for the calculation can be found in the supporting information of our published paper [MacLaren 2012]. Here we only summarise the procedure regarding the modification of our initial model and main results.

Figure 4.11 schematically shows the definition of the super cell we used for the calculation which contains 336 atoms in total with 66 Bi, 4 Nd, 62 Fe, 2 Ti and 202 O. A size of 6x6x2 $BiFeO_3$ matrix marked as blue was constructed at the edge of the supercell. The nanorod region marked as red mainly contained 4 Nd and 12 Bi. The rest were allocated to the interface region as marked with green outside of the red. These regions are used to calculate the local densities of states (DOS) in Figure 4.14. In order to optimize the primary model, a large number of possible starting configurations were tested with different local arrangements of oxygen ions coordinating Nd and Ti, and O ions in the interface region. Specifically, starting configurations with edge and corner sharing Nd polyhedra along the *c*- and *b*-axes were tested, and Ti was initiated as 5- and 6-coordinated. With the stoichiometric restriction that the supercell must be charge-neutral, octahedral oxygen coordination of Nd^{3+}, Ti^{4+} and Fe^{3+} requires strongly

elongated octahedra at the interface between the $Bi(Fe,Ti)O_3$ matrix and the Nd nanorod precipitates. Such elongated octahedra were found to be unstable, and structural relaxation of the oxygen positions spontaneously evolved towards five-coordinated Fe^{3+} and Ti^{4+} in the interface region, and seven-coordinated Nd in the nanorod precipitate. Placing Ti^{4+} in one column rather than in different columns was found to be energetically favourable. Details are described as below.

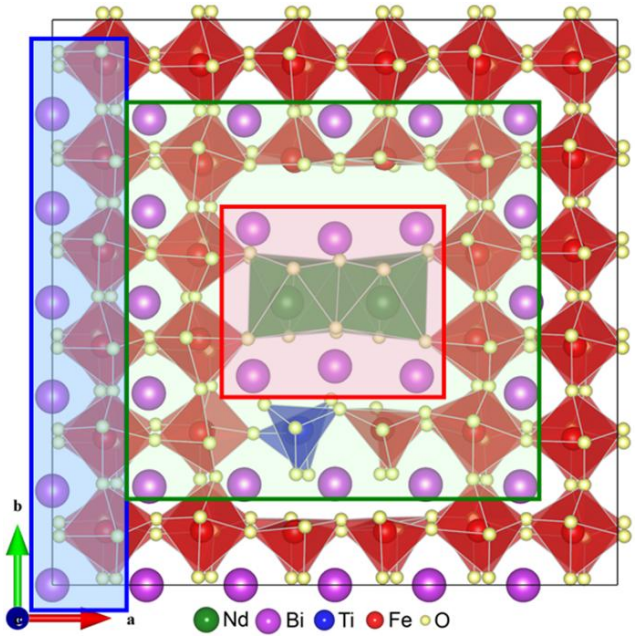

Figure 4.11. *Regions of the supercell model used for plotting local DOS in Figure 4.12; blue: matrix region; red: nanorod region and green: (outside red): interface region.*

Regarding the position of Ti ion, there were four possible non-degenerate positions of the Ti column at the interface towards the Nd rod precipitate relating to the relaxation of the $Fe(Ti)O_6$ lattice caused a displacement along the [113] axis of the supercell, which is parallel to the [111] pseudocubic axis of bulk rhombohedral $BiFeO_3$. The main difference between these four models was that Ti was most stable as five-coordinated (Figure 4.12 (a))when placed in one of the two columns displaced *towards* the Nd nanorod columns (along positive b-axis), but more stable as six-coordinated if placed in a column displaced *away from* (larger value along positive b-axis) the Nd nanorod columns (Figure 4.12 (b)). However, the displacement of Ti ions on either side

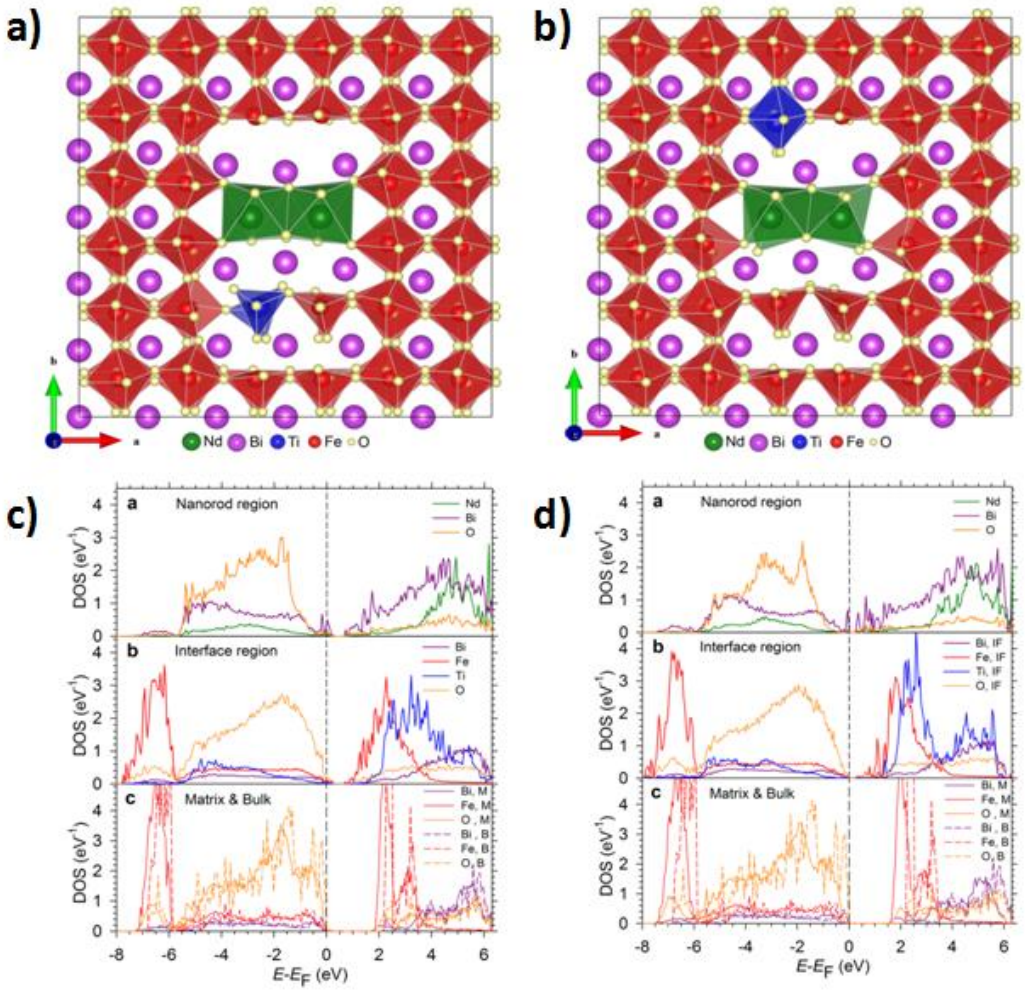

Figure 4.12. *Atomic structure models after DFT structural relaxations in end-on orientation and their correlated DOS; a) the model with five-coordinated Ti towards the Nd nanorod columns; b) is the model with six-coordinated Ti away from the Nd nanorod columns; c) DOS from model with five-coordinated Ti; d) DOS from model (b) with six-coordinated Ti.*

of the nanorod has negligible impact on the structure and DOS (Figure 4.12 (c), (d)). But with five-coordinated Ti, the additional two oxygens were found to be most stable in the Nd nanorod columns with seven-coordinated Nd. The total energy of the models with five coordinated Ti and seven-coordinated Nd was of the order of 1.7 eV lower than the models with six-coordinated Ti and Nd. Finally, the atomic positions were then relaxed fully using density functional theory (DFT). Note that, since our calculated supercell matrix does not contain Nd, our structural optimizations obtained the $a^-a^-a^-$ octahedral tilt structure of undoped $BiFeO_3$; when we imposed the $a^-a^-c^+$ pattern of the $PbZrO_3$-like

structure found in samples with this level of Nd doping, (which we could not subsequently allow to relax) we obtained the same qualitative behaviour that we present here. (Doping of the matrix with Nd was not included in our calculations due to the extra complexity this would introduce in the DFT calculations).

4.4.3 Structural model confirmation by multislice image simulation-QSTEM

Overall, our lowest energy calculated nanorod/matrix model should be the top-left one shown in Figure 4.12. To confirm its validity, multislice simulations of HAADF images were performed using the QSTEM package of Christoph Koch [Koch 2002] with the frozen phonon approximation for the treatment of thermal diffuse. Results were calculated for a sample split into 1.95 Å slices, with the atoms centred in each slice, for a total thickness of 40 unit cells or 80 slices, equivalent to 15.6 nm. Simulation results are displayed with experimental results in Figures 4.13 with (a) - (f) is for end-on defects while (g) and (h) involve a side-on defect. An excellent qualitative agreement was obtained between them. Figure 4.13a) show a HAADF image of an isolated nanorod which matches very well with a simulated HAADF image of a defect running through a thickness of 40 unit cells (~ 15.6 nm) in Figure 4.13 (b). In particular, the significant off-centering of the B-site ions immediately above the core is well reproduced in the simulation, giving confidence that the predicted DFT structure represents the real structure rather well. The HAADF image shown in Figure 4.13 (c) is of an overlap image showing features of both a nanorod and of the normal perovskite structure, but the contrast for the nanorod is stronger than that for the perovskite; this image matches well to the simulation shown in Figure 4.13 (d) which is for 10 cells of nanorod on the entrance surface followed by 30 cells of perfect perovskite (total thickness ~15.6 nm). Another HAADF image showing overlap is shown in Figure 4.13 (e), this time with the perovskite contrast stronger than that from the nanorod. Figure 4.13 (f) shows a simulation for 10 cells of perfect perovskite on the entry surface, followed by 20 cells of nanorod, and capped with 10 cells of perfect crystal (again making a total thickness of 15.6 nm); as before, this demonstrates a good match between experiment and simulation. The image simulations demonstrate that the range of experimental images observed in

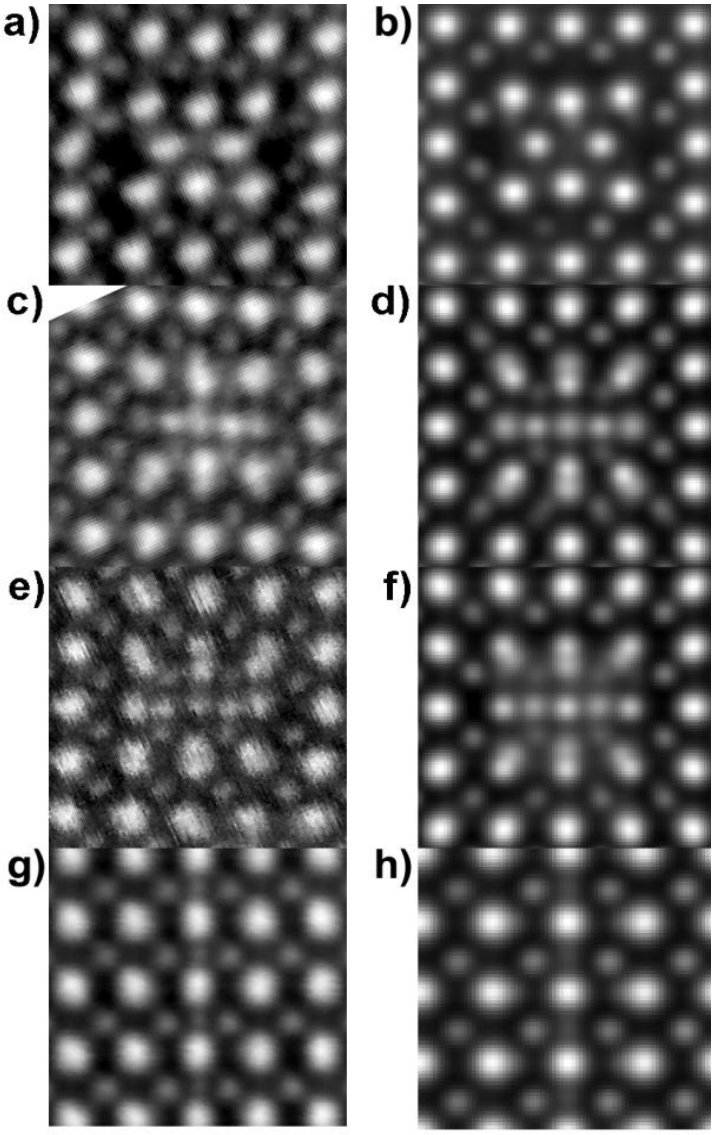

Figure 4.13. *HAADF image simulations for this model compared to real images: a) end-on image of a nanorod; b) simulation of a nanorod extending through the entire 40 cell thickness of the crystal; c) image of the overlap between a defect and perfect crystal; d) simulation of 10 unit cells of nanorod on the entrance surface followed by 30 unit cells of perfect perovskite $BiFeO_3$; e) image of another overlap between a nanorod and perfect crystal; f) simulation of 10 cells of perfect perovskite overlaying 20 cells of nanorod, followed by 10 more cells of perfect crystal; g) side-on view of a nanorod (detail from the same image as used in Figure 4.9a); h) simulation of an image of a nanorod lying right at the entrance surface of the crystal viewed along the a-axis (as shown in Figure 4.12), followed by perfect crystal, with a total thickness of 30 unit cells.*

Figure 4.1 (b) can be explained by a combination of a defect of suitable length embedded at some point in the perovskite matrix. Finally, a side-on view of one of the defects is shown in Figure 4.13 (g) (a detail from the same image was used in constructing Figure 4.9 (a)). This shows a good match to a simulation of a nanorod in side-on orientation (with the *a*-axis of Figure 4.12 placed vertical in this simulation). The nanorod that lies on the entrance surface of a crystal block was 30 unit cells thick (~11.9 nm). This excellent match between simulations and the experimental images confirms the 3-dimensional model of Figure 4.12 (top-left). Moreover, they re-emphasise the point that has been shown in other recent work that the visibility of atoms in HAADF STEM imaging depends strongly on their position in the crystal [Shannon 2007], and that STEM imaging is particularly sensitive to atoms on the entrance surface, such as the two Nd atoms in the side-on simulation, which are still clearly visible despite having another 28 layers of perovskite behind them in the simulation.

4.4.4 Summary of the features for the nanorod structural model

The most striking structural feature of our finalized model is the presence of (Fe/Ti)-O_5 square-based pyramids containing five-coordinated Fe/Ti ions immediately adjacent to the Nd-rich core; in contrast bulk $BiFeO_3$ contains FeO_6 octahedra. Oxygen atoms have been transferred from the FeO_6 octahedra to the Nd-rich core, so that the Nd ions become seven-coordinated. This is accompanied by significant off-centring of the B-site ions, especially the Fe ions above the Nd-rich core (with larger positive b value), which reproduces contrast in image simulations very much like the experimental observations (Figure 4.13). The structure of five-coordinated Fe/Ti and seven-coordinated Nd has lower energy than corner-sharing NdO_6 and FeO_6 octahedra. One origin of this configuration is likely chemical: the larger and more electropositive Nd^{3+} ions have a greater affinity for oxygen ions than Fe^{3+} ions do, and while Nd^{3+} is commonly found with a coordination number of 6 or higher in oxides, the coordination number of Fe^{3+} is usually 6 or lower.

4.5 Properties of The Nanorods and Their Effects on The Perovskite Matrix

4.5.1 Strain interactions with the matrix, spontaneous alignment and domain pinning

It has been reported that a so-called T-phase is quite common in compressively strained thin films of $BiFeO_3$ [Zeches 2009, Hatt 2010], with a huge *c/a* ratio and a five-fold coordination of Fe, which resembles to the FeO_5 square pyramids observed here. The "internal strain" caused by the cores of the nanorods, which contain only two A-site cations where there would be three in bulk $BiFeO_3$, appears to induce an analogous local phase change on the surrounding cells of perovskite $BiFeO_3$. Conversely, the ability of $BiFeO_3$ to adapt to the anisotropic local strain by morphing smoothly between structural allotropes likely facilitates the spontaneous formation of the nanorods, where their formation in a "harder" matrix material would introduce prohibitively large local strains. Indeed, super-saturated solid solutions usually form spherical rather than rod-shaped precipitates because the former minimize the unfavourable interfacial energy. The fact that rod-shaped precipitates have formed here suggests a significantly lower interfacial energy between the core and the matrix. Again similar structure like T-phase of local regions has been reported at the $BiFeO_3$-Bi_2O_3 interface in thin films [Liu 2012] and are predicted theoretically in Fe-doped Bi-based Aurivillius phase compounds [Birenbaum 2012]. The local tensile strain may also favour segregation of the smaller Ti^{4+} ions towards the nanorod/matrix interface, where configurational entropy would favour a random distribution of Ti in the matrix, although here the compensation of the higher valence Ti^{4+} B-site cations by the A-site vacancies likely also plays a role. The DFT calculations show that segregation of Ti to one column around the nanorod is energetically favourable in agreement with the experimental results such as Figure 4.6(d) and Figure 4.7 (b) for Ti. Indeed, as discussed in more detail elsewhere [Reaney 2012], the very formation of the nanorods is likely caused by the creation of A-site vacancies, specifically ex-solving a proportion of the Nd^{3+}, as an ionic compensation mechanism associated with the doping of an excess of Ti^{4+} into the ceramic. More detail regarding the doping level effect will be discussed in section 4.5.3.

In addition to the interplay between strain and local B-site coordination, it is likely that the observed parallel alignment of the nanorods is caused by minimisation of strain energy in the system. Our observation with the BNFTO-15_10 sample is that the precipitates are always parallel to specifically the [001] axis of the *Pbam* $BiFeO_3$ matrix, which is of particular interest since the nanorods form at high temperature during sintering, whereas the ferroelastic domain structure forms in a phase transition from a paraelectric (PE) *Pbnm* structure to antiferroelectric (AFE) *Pbam* structure transition at ~250 °C [Kalantari 2011]. At the PE-AFE transition the cell doubles along the b axis and there is a volume change of ~ 2% dominated by an anisotropic expansion of the pseudocubic b axis [Levin 2010]. It is likely, therefore that the nanorods formed parallel to the [001] axis in the high temperature *Pbnm* phase (also sometimes referred to in an alternate cell setting as *Pnam* [Karimi 2009]) and that this specific alignment is energetically favoured by strain considerations. Whilst it is unclear whether the growth of ferroelastic domains in the AFE structure is purely determined by the domain structure in the PE structure, or whether the additional strain fields of the nanorods also plays a role, it is likely that the presence of these aligned strain fields from the nanorods will strongly influence domain alignment and make AFE-FE switching more difficult. The PE-FE transition (orthorhombic to rhombohedral) also shows a large volume change and it is anticipated that similar domain-precipitate alignment is feasible. If the parallel nanorods could be generated in an FE composition, the nanorods will act as pinning centres for domain wall motion under applied field, hardening the FE behaviour. Their presence and configuration therefore hints at subtle ways in which domain structures in RE-doped $BiFeO_3$ may be engineered, a subject of potential importance for thin film applications.

4.5.2 Electronic properties of the nanorods

The electronic properties of the nanorods calculated from DFT (Figure 4.12 (c)) shows that the electronic structure of the nanorods and the adjacent interface layer deviates strongly from that of the $BiFeO_3$ matrix. In particular, the nanorods have a finite DOS at the Fermi energy indicating that there may be more electrically conducting than the $BiFeO_3$ matrix. In addition, in the interfacial $BiFeO_3$ region that is immediately next to the Nd oxide core, the band gap is reduced to 0.8 eV (Figure 4.12 (c):b). The origin of the reduction is the lowering in energy of the Fe *d* states at the bottom of the

conduction band due to the reduction in crystal field splitting. The electronic structure of the matrix region is very similar to that of bulk $BiFeO_3$ from our own calculations (Figure 4.12 (c):c) and previous studies [Neaton 2005] and shows the calculated literature band gap of ~2.0 eV. Conducting self-assembled parallel nanorods in a ferroelectric matrix could open intriguing new device directions, and verification of our predicted electrical properties will be the focus of future work.

4.5.3 Doping level effect on the nanorods and the perovskite matrix

Kalantari *et al.* [Kalantari 2011] reported that the structure of BFO co-doped with Nd and Ti would change from the orthorhombic phase to a rhombohedral phase with decreasing doping level. If this is the case, and nanorods are still formed there, we may be able to observe both the end-on and side view of the nanorods in the same domain and possibly with both orientation for the side-on view. This is confirmed by our experiment using high resolution MAADF STEM images along a [001] pseudocubic direction. Figure 4.14 and 4.15 show both end-on (marked with pink colour) and side view (marked with yellow-green) nanorods in the same domain for compositions of 12.5% Nd, 3% Ti and 10% Nd, 3% Ti, respectively. However, due to the depth of focus or the defects at different height, it is difficult to image clearly on both of them simultaneously. The inserted images, in Figure 4.15, showing side views of two nanorods with different orientations (90º with respect to each other) give further support to the structural evolution. Moreover, as the doping level decreases, the length of the nanorods reduces as well. Within our study so far, no nanorod with length more than 3-4 unit cells long (which is less than 2 nm, see the side view in Figure 4.14 & 4.15) has been observed with these two samples containing just 3% Ti. As we expected, apart from the reduction of the length of nanorods, the density of nanorods within samples of both compositions was also reduced (as shown in Figure 4.16), compared to the composition of 15% Nd, 10% Ti (Figure 4.16 (c)). However, there is not much difference with nanorods density between Figure 4.16 (a) and Figure 4.16 (b) as the Ti doping levels were the same and there was only a small difference (about 2.5%) in Nd doping level. This is consistent with Reaney *et al*. [Reaney 2012] where it is argued that nanorod formation is caused by excess Ti doping on the B-sites exsolving Nd from the matrix in preference to Fe and Bi in order to create A-site vacancies. Since images were taken using the MAADF detector, white patches are shown here again in all of these

images indicating that the strain field is around the nanorods within the perovskite matrix, but is rather localised and the short nanorods are not strongly interacting. If more Ti is doped to the B-sites, as in the BNFT-15_10 sample discussed in the earlier part of this chapter, more nanorods are formed and they are longer, so they have a much larger strain effect within the crystal and upon each other.

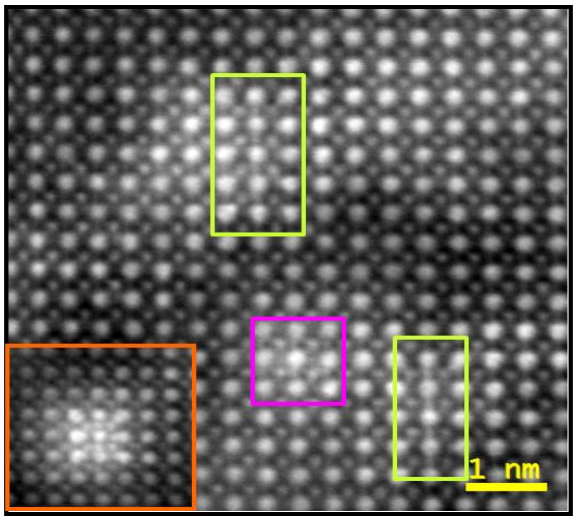

Figure 4.14. *MAADF image of BNFT-12.5_3 sample with inserted HAADF image, showing the coexistence of end-on (marked with pink colour) and side-on (marked with yellow-green colour) views of the nanorods.*

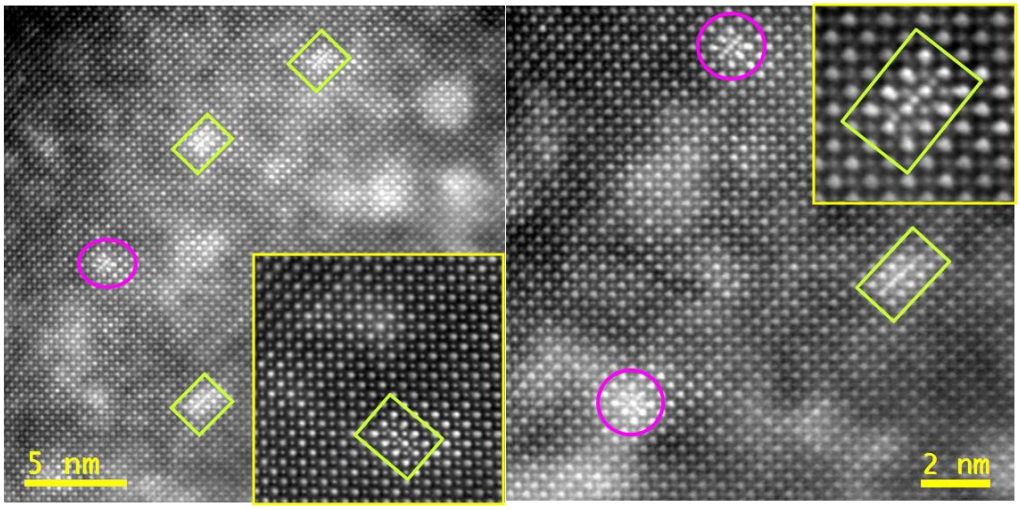

Figure 4.15. *MAADF images of BNFT-10_3 sample, showing the coexistence of end-on (marked with pink colour) and side-on (marked with yellow-green colour) view of the nanorods, but the length of side-on defects are quite short; inset are HAADF images showing the coexistence of side-on views of two orientations.*

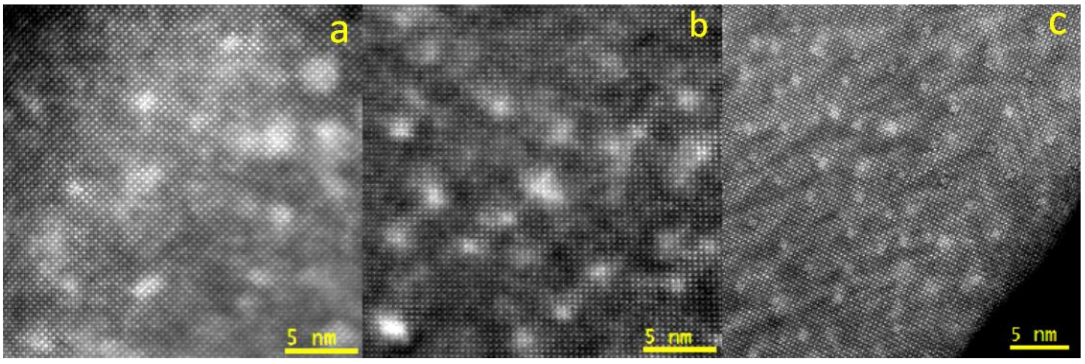

Figure 4.16. *MAADF images showing the doping level effect on density and strain with samples of BNFT-10_3, a); BNFT-12.5_3, b); BNFT-15_10, c).*

4.6 Conclusions

As stated in chapter one, nanostructure can play an important role in the properties of a crystal. The work presented in this chapter demonstrates the spontaneous formation and self-assembly of Nd-rich nanorods in $BiFeO_3$ co-doped with Nd and Ti, and a thorough investigation of their structure, chemistry and electronic structure was carried out using a combination of atomic resolution imaging and spectroscopy in the scanning transmission electron microscope together with density functional calculations. This work revealed that:

1) The structure of the nanorods are Nd oxide with surrounding interfacial region of "T-phase-like" BFO matrix which bridges the lattice mismatch and strain between the nanorods and bulk BFO.

2) The interplay between the strain of surrounding matrix and the structure of nanorods is important for the stabilisation of nanorods and their spontaneous alignment correlating with the domain structure in the $BiFeO_3$ matrix.

3) The very formation of nanorods is caused by excess Ti doping to the B-sites resulting in the creation of Nd vacancies to compensate the solution of extra Ti^{4+}, as there is no hint of a discrete second phase of Ti.

4) The ionic compensation mechanism as discussed in our paper [Reaney 2012] causes the formation of nanorods to create A-site vacancies; this suppresses the semi-conductivity and gives at least a partial explanation for the non-linear dependence of T_c for Ti-doped $Bi_{0.85}Nd_{0.15}FeO_3$.

5) Electronic structure calculations predict that the nanorods have higher electrical conductivity than the surrounding, insulating matrix, paving the way to additional novel functionalities in multiferroic BFO.

References:

Ahn C. C., Krivanek O. L., EELS Atlas - a reference guide of electron energy loss spectra covering all stable elements, ASU HREM Facility & Gatan Inc, Warrendale, PA: **1983**.

Allen L. J., D'Alfonso A. J., Findlay S. D., LeBeau J. M., Lugg N. R., Stemmer, S., (**2010)** Elemental mapping in scanning transmission electron microscopy, In Electron Microscopy and Analysis Group Conference 2009, Baker, R. T., Ed. IOP Publishing Ltd: Bristol, Vol 241.

Birenbaum Y., Ederer C. **(2012)** personal communication.

Catalan G., Scott J. F., **(2009)** Physics and applications of Bismuth Ferrite, Adv. Mater., **21**, 2463.

Choi T., Lee S., Choi Y. J., Kiryukhin V., Cheong S. W., **(2009)** Switchable ferroelectric diode and photovoltaic effect in $BiFeO_3$, Science, **324**, 63.

Cui Y. F., Zhao Y. G., Luo L. B., Yang J. J., Chang H., Zhu M. H., Xie D., Ren T. L., **(2010)** Dielectric, magnetic, and magnetoelectric properties of La and Ti codoped $BiFeO_3$, Appl. Phys. Lett., **97,** 222904.

Das S. R., Choudhary R. N. P., Bhattacharya P., Katiyar R.S., Dutta P., Manivannan A., Seehra M.S., **(2007)** Structural and multiferroic properties of La-modified $BiFeO_3$ ceramics, J. Appl. Phys., **101**, 034104.

Fujino S., Murakami M., Anbusathaiah V., Lim S. H., Nagarajan V., Fennie C. J., Wuttig M., Salamanca-Riba L., Takeuchi I., **(2008)** Combinatorial discovery of a lead-free morphotropic phase boundary in a thin-film piezoelectric perovskite, Appl. Phys. Lett., **92,** 202904.

Hatt A. J., Spaldin N. A., Ederer C., **(2010)** Strain-induced isosymmetric phase transition in $BiFeO_3$, Phys. Rev. B, **81**, 054109.

Houben L., iMtools imaging processing software, http://www.er-c.org/centre/software/imtools.htm

Kan D., Palova L., Anbusathaiah V., Cheng C. J., Fujino S., Nagarajan V., Rabe K. M., Takeuchi I., **(2010)** Universal behavior and electric-field-induced structural transition in rare-earth-substituted $BiFeO_3$, Adv. Func. Mater., **20,** 1108.

Karimi S., Reaney I. M., Levin I. and Sterianou I., **(2009)** Nd-doped $BiFeO_3$ ceramics with antipolar order, Appl. Phys. Lett. **94,** 112903.

Koch C. T., http://www.christophtkoch.com/DM-Plugin/index.html

Koch C., Determination of core structure periodicity and point defect density along dislocations, PhD Thesis,**(2002)** Arizona State University.

Levin I., Karimi S., Provenzano V., Dennis C. L., Wu H., Comyn T. P., Stevenson T. J., Smith, R. I., Reaney I. M., **(2010)** Reorientation of magnetic dipoles at the antiferroelectric-paraelectric phase transition of $Bi_{1-x}Nd_xFeO_3$ ($0.15 <= x <= 0.25$), Phys. Rev. B., **81,** (2), 020103.

Liu H. J., Yang P., Yao K., Ong K. P., Wu P., Wang J., **(2012)** Origin of a Tetragonal $BiFeO_3$ Phase with a Giant c/a Ratio on $SrTiO_3$ Substrates, Adv. Func. Mater., **22,** 937.

MacLaren I., Villaurrutia R., Schaffer B., Houben L., Pelaiz-Barranco A., **(2012)** Atomic-Scale Imaging and Quantification of Electrical Polarisation in Incommensurate Antiferroelectric Lanthanum-Doped Lead Zirconate Titanate, Adv. Func. Mater., **22,** (2), 261-266.

Murashov A., Rakov D.N., Dubienko I.S., Zvezdin A.K., Ionov V.M., **(1991)** *Sov. Phys. Crystallogr*. **35,** 538.

Neaton J. B., Ederer C., Waghmare U. V., Spaldin N. A., Rabe K. M., **(2005)** First-principles study of spontaneous polarization in multiferroic $BiFeO_3$, Phys. Rev. B., **71.**

Reaney I. M., MacLaren I., Wang L. Q., Schaffer B., Craven A., Kalantari K., Sterianou I., Karimi S., Sinclair D. C., **(2012)** Defect chemistry of Ti-doped antiferroelectric $Bi_{0.85}Nd_{0.15}FeO_3$, Appl. Phys. Lett., **100,** 182902.

Robb P. D., Finnie M., Longo P., Craven A. J., **(2012)** Experimental evaluation of interfaces using atomic-resolution high angle annular dark field (HAADF) imaging, Ultramicroscopy, **114**, 11-19.

Saeterli R., Selbach S. M., Ravindran P., Grande T., Holmestad R., **(2010)** Electronic structure of multiferroic BiFeO3 and related compounds: Electron energy loss spectroscopy and density functional study, Phys. Rev. B., **82**, 064102.

Schaffer B., Grogger, W.; Kothleitner, G., **(2004)** Automated spatial drift correction for EFTEM image series, Ultramicroscopy, **102**, (1), 27-36.

Scott J., Thomas P. J., MacKenzie M., McFadzean S., Wilbrink J., Craven A. J., Nicholson W. A. P., **(2008)** Near-simultaneous dual energy range EELS spectrum imaging, Ultramicroscopy, **108**, (12), 1586-1594.

Seidel J., Martin L. W., He Q., Zhan Q., Chu Y. H., Rother A., Hawkridge M. E., Maksymovych P., Yu P., Gajek M., Balke N., Kalinin S. V., Gemming S., Wang F., Catalan G., Scott J. F., Spaldin N. A., Orenstein J., Ramesh R., **(2009)** Conduction at domain walls in oxide multiferroics, Nat. Mater., **8**, 229-234.

Shannon M. D., Lok C. M., Casci J. L., **(2007)** Imaging promoter atoms in Fischer-Tropsch cobalt catalysts by aberration-corrected scanning transmission electron microscopy, J. Catal., **249**, (1), 41-51.

Yu B.F., Li M., Wang J., Pei L., Guo D., Zhao X., **(2008)** Effects of ion doping at different sites on electrical properties of multiferroic $BiFeO_3$ ceramics, J. Phys. D: Appl. Phys. **41** 185401.

Yuan G. L., Or S. W., **(2006)** Enhanced piezoelectric and pyroelectric effects in single-phase multiferroic $Bi_{1-x}Nd_xFeO_3$ (x=0-0.15) ceramics, J. Appl. Phys., **100**, 024109.

Yuan G. L., Or S. W., Liu J. M., Liu Z. G., **(2006)** Preparation and multi-properties of insulated single-phase BiFeO3 ceramics, Appl. Phys. Lett., **89**, 052905

Zeches R. J., Rossell M. D., Zhang J. X., Hatt A. J., He Q., Yang C. H., Kumar A., Wang C. H., Melville A., Adamo C., Sheng G., Chu Y. H., Ihlefeld J. F., Erni R., Ederer C., Gopalan V., Chen L. Q., Schlom D. G., Spaldin N. A., Martin L. W., Ramesh R., **(2009)** A Strain-Driven Morphotropic Phase Boundary in $BiFeO_3$, Science, **326**, 977.

Zhang S. T., Zhang Y., Lu M. H., Du C. L., Chen Y. F., Liu Z. G., Zhu Y.Y., Ming N. B. **(2006)** Substitution-induced phase transition and enhanced multiferroic properties of $Bi_{1-x}La_xFeO_3$ ceramics, Appl. Phys. Lett. **88**, 16290.

Chapter 5 Novel anti-phase boundaries

5.1 Introduction

As mentioned in chapter 1, the ABO_3 perovskite structure is constructed from corner sharing BO_6 octahedra that can accommodate a variety of compositions with a wide range of cations. However, according to the Goldschmidt tolerance factor [Goldschmidt 1926] $t = \frac{(r_A + r_O)}{\sqrt{2}(r_B + r_O)}$, if the substitution causes the factor t to deviate markedly from the ideal value (≈1), the oxygen octahedra have to rotate along a fourfold or twofold axis or deform to maintain a stable perovskite structure. Therefore, the symmetry of the structure will be lowered. A lowering in symmetry will of course introduce different orientation variants and translation variants, resulting in the formation of twins and anti-phase boundaries [Guymont 1978, van Tendeloo 2004]. A twin boundary is a special domain boundary that relates two domains by a simple symmetry operation, normally a reflection operation of a mirror plane (which is also called twin plane). An anti-phase boundary (APB) is an interface within a crystal where the origin of the crystal unit cell is related by a simple translation operation across the boundary plane (usually of half a unit cell in length). Local chemistry changes can also introduce the formation of APB like those reported by Lebedev *et al.* [Lebedev 1999] and the new one described in this chapter. An APB may also separate two domains with different orientations of the ferroelectric ordering; such APBs may be referred to as anti-phase domain boundaries (APDB). Obviously, not all domain boundaries are APDBs. In general, domain boundaries are defined as boundaries that separate domains with different orientations. In BFO, since there is spontaneous ferroelectric polarization along a pseudocubic <111> direction, there are eight available polarization orientation variants in total, which allows the formation of three types of ferroelectric domain walls with angles of 71º, 109º, 180º regarding the angle between the polarization vectors on either side of the wall. Generally, 71º domain walls are parallel to {110} plane, 109º walls are in {001} planes, and 180º walls are on planes containing [111] polar vector. In contrast to undoped BFO, the conventional domain boundaries in $PbZrO_3$ - type structures, such as 15% Nd-doped BFO, are 60º, 90º and 180º [Tanaka 1982, MacLaren 2010]. Unlike domain boundaries, compositionally different APBs induced by local chemistry changes are not mobile at ambient temperatures, thus they could have a significant impact upon

the properties of the materials via their effect on the microstructure and other defects [Lebedev 1999]. Hence, understanding of these features within the microstructure or nanostructure that associate directly to the structural change of the crystal is the prerequisite of understanding of associated physical behaviour changes. In this chapter, a type of novel APB observed in the (001) plane from the sample with composition of BNFT-15_10 is reported here and their formation is caused by extreme chemical doping in the BFO. Some of these APBs also act as domain boundaries. The characterization of the APB was carried out using the aberration corrected STEM and atomic resolution EELS and similar method as described in chapter 3. The whole chapter is structured as follows: firstly, details of the structure of this anti-phase boundary (APB) and its chemical information will be described in section 5.2, then a structural model will be built up and the validation of the proposed model by QSTEM simulation will be carried out in section 5.3 and 5.4, and the properties of the APB and its impact to the material will be discussed in section 5.5. Finally, a summary will be concluded in section 5.6.

5.2 About The Novel APB

Figure 5.1(a) shows a DF image of the studied area from a BNFT-15_10 sample, recorded by CTEM T20 with associated SAD along the [001] direction. Obviously, there are two dark ribbons, similar to those that have been observed in another area mentioned in Figure 4.1(a), running almost parallel across the sample from top to bottom with some nanorods spots (also see in Figure 5.1 (b)) between them. Such boundaries were frequently observed in this ceramic. Closer study of the high resolution HAADF image in Figure 5.1 (b) shows that the boundaries are constructed from two main structural units – flat terraces and steps, thus we will discuss these two parts separately. The central region between the two boundaries with nanorods of end-on view means that this region is along the $[001]_o$ direction. Although the precise character of the regions to the left and the right is undetermined, their orientation differences with the $[001]_o$ direction of the central region indicate that both boundaries shown here are also domain boundaries. Within the terrace part of the boundary, there is a vertical shift of one half of a primitive perovskite unit cell across the boundary, as required for an antiphase boundary, with brighter atom columns corresponding to the heavy Bi/Nd (A-site) atoms and weaker columns corresponding to the lighter Fe/Ti (B-site) atoms. Another key

feature of the structure in the terrace is the "ladder" appearance of pairs of A-site atoms in the boundary alternating with pairs of B-site atoms along the vertical direction. As for the steps, they can be treated as two terraces shifted with respect by one perovskite unit cell perpendicular to the terrace plane but with no A-site atoms between the pairs of B-site atoms at the step, i.e. the step consists of 4 B-site atoms, together with whatever oxygen co-ordinates these atoms. A further feature of note in the HAADF image is the very dark areas of contrast on either side of the boundaries in the vertical direction indicated by orange arrows. In order to make those subtle details of the low intensity part in the image to be readily seen in a way that would be difficult with a normal grey-scale image, a false colour scale is used in Figure 5.2 and Figure 5.4.

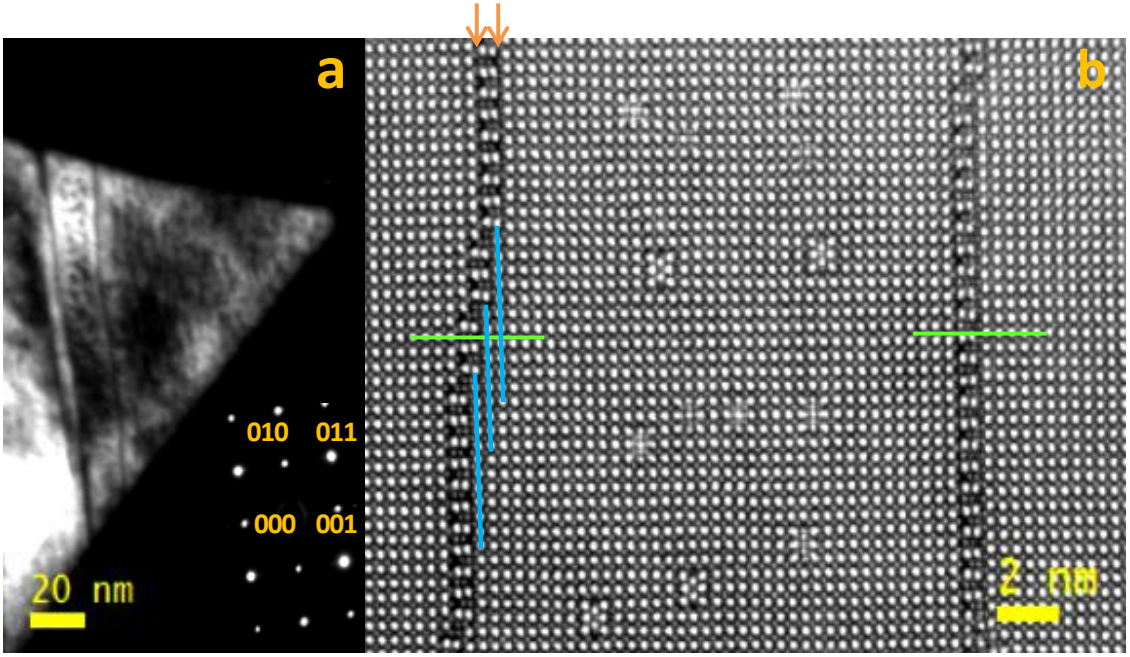

Figure 5.1. *a) DF image with SAD pattern showing an area with two darker ribbons running cross the sample; b) HAADF image reveals the two darker ribbons are actually APBs consisting of terrace parts with varied length and steps, and the dark spots between the two ribbons in DF image are corresponding the nanorods in between the two APBs. The half unit cell shifting cross the boundary is marked by the green lines; horizontal shift of one perovskite unit cell at the steps is indicated by blue lines.*

5.3 Quantitative Analysis of The APB - Terrace Part

5.3.1 Structural and chemical information about terrace

Figure 5.2 shows a HAADF image of one of the terraces recorded by SuperSTEM2 and a BF image with clear atomic resolution contrast which was recorded simultaneously as well. Comparing these two images, it is noticeable that the dark holes in the HAADF contrast correspond to the very bright areas in the BF image. To make this clearer, the HAADF image and the BF image are overlaid in a two colour red-cyan image and it is clear that the cyan-coloured BF image has bright peaks where one would expect to see oxygen-only columns in a <100> projection of a perovskite, which also gives the clue that the oxygen positions in and around the boundary can at least approximately be interpreted as corresponding to the bright peaks in the BF image when we try to build the structure model.

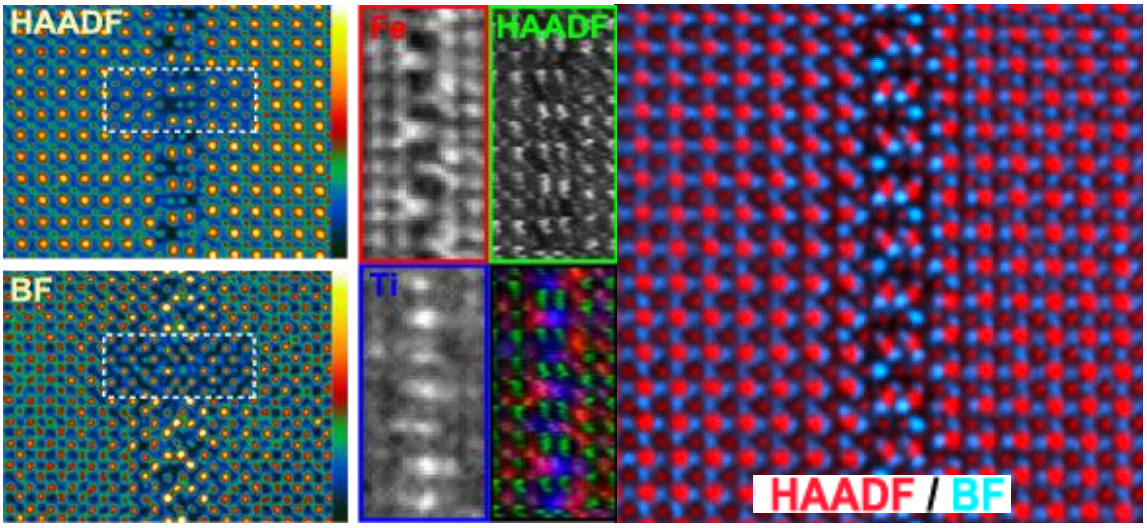

Figure 5.2. *Atomic resolution STEM images and EELS maps of the APB (terrace part) along the first projection; the colour scales are shown for the false colour images and the same scale was used for both HAADF and BF images. Insets of the simulated images are overlaid on the experimental images using exactly the same contrast scale. The EELS maps for individual images show the full contrast range, whereas the contrast has been enhanced to remove background intensity and thus to enhance visibility of the main atomic columns in the RGB image.*

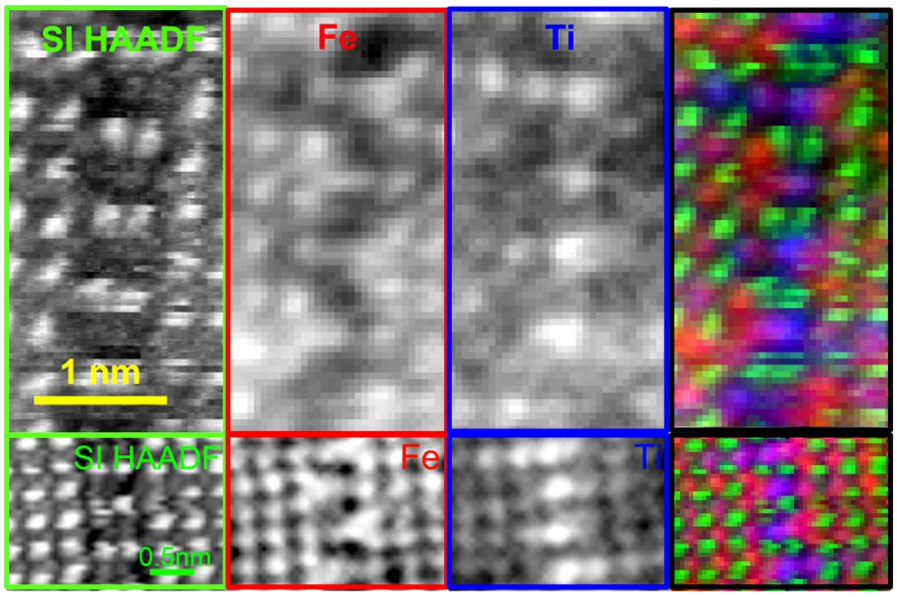

Figure 5.3. *Elemental maps from two other areas showing the chemistry similarity of the APBs (terrace part).*

In order to understand the chemistry of the boundary in more detail, atomic resolution EELS was performed on several areas of such a boundary over an energy loss range from about 250 eV to about 1100 eV. Chemistry distributions from the elemental maps of these EELS are all very similar and one of the results from the same area as HAADF image was taken are shown together in Figure 5.2 and two other results from different areas are shown in Figure 5.3 to show the similarity. Similar procedures as described in Chapter 4 were carried out to get the final results of the maps. The maps shown here are those for the Fe $L_{2,3}$ edge around 708 eV, and the Ti $L_{2,3}$ edge around 456 eV, with a red-green-blue (RGB) image showing Fe (R), HAADF (G) and Ti (B) signals together. The HAADF signals recorded simultaneously with the EELS signal are also shown in order to show the heavy A-site atoms in the RGB image. The Nd signal was also examined, but little Nd was found in the boundary, and limited amounts were seen randomly distributed on A-site columns in the matrix to either side. It is clear from the maps shown here that the central B-site columns are dominated by Ti with little Fe, additionally, there is a tendency for alternate columns to the left and right of the central Ti row to also contain some Ti.

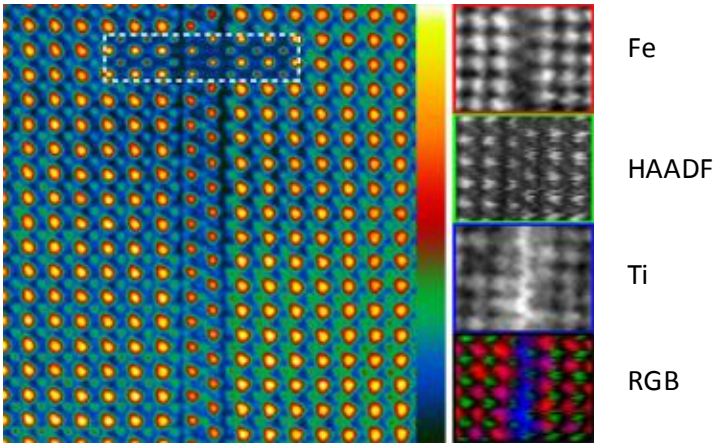

Figure 5.4. *HAADF image and EELS maps of the antiphase boundary along the second (perpendicular) projection. An inset of a simulated image is overlaid on the HAADF image using exactly the same contrast scale. The EELS maps for individual images show the full contrast range, whereas the contrast has been enhanced to remove background intensity and thus to enhance visibility of the main atomic columns in the RGB image.*

Interestingly, this striking planar APBs were also observed from the perpendicular <001> direction in the boundary. Figure 5.4 shows a high angle annular dark field image of such an edge-on view, as well as atomic resolution EELS maps, as before. Obviously, the image is dominated by the half unit cell shift in the bright A-site positions across the boundary, but a number of very weak B-site positions can also be distinguished as faint green dots using the false colour scale of this image. Bright field images have also been recorded for this second projection, but the details of the boundary were less easy to resolve and it was clear that a small mistilt of the crystal was having a negative effect on the imaging. Elemental maps show clearly that there is a deficiency of iron at the boundary core, and a strong segregation of titanium to the core, which is fully consistent with the pattern of the Ti segregation shown in Figure 5.2 from the perpendicular projection.

5.3.2 Creation of structural model and simulation results

Using the same techniques as described previously in chapter 3, atom positions for A-site and B-site atoms were measured quantitatively from the HAADF images from both projections as shown in Figures 5.2 and 5.3 and distortions from the scanning system were corrected afterwards. Additionally, the positions of bright peaks in the BF image of Figure 5.2 were also determined in the same way and treated as if these

represented oxygen positions, in accordance with the work of LeBeau *et al.* [LeBeau 2009]. The two projections were then combined to yield a three-dimensional atomic structure using a discrete tomography approach, similar to that of van Aert *et al.* [van Aert 2011]. Specifically, it was assumed that the co-ordination of atoms to either side of the boundary was perovskite like, and the only complex part was correlating the atomic positions in the boundary from the perpendicular view to get a reasonable structure. Errors on A-site atoms were of the order of 7 pm, errors on B sites were of the order of 8 pm, errors on O positions were of the order of 10 pm. It should be noted that no Nd atoms have been included in the model. Nd is isovalent to Bi, so will have no effect on charge balance in the model, and will substitute randomly onto Bi sites (almost 15%) outside the boundary. Similarly, outside the boundary, all B-site atoms are assumed to be Fe atoms for simplicity, but in reality, nearly 10% of B-sites will be Ti atoms. A final assumption in the creation of the model was regarding the positions of O atoms. For those pure O atom columns (without any B-site atoms within the column), O positions could be represented by the data extracted from the BF image in Figure 5.2. However, in this BF image, for those very bright peaks within the boundary corresponding to the very dark contrast in the HAADF image, a number of possibilities were considered: either no atoms in these columns at all, or maybe some oxygen occupancy (full or partial) there. To determine the oxygen level, we set up three simulations (other simulation conditions are the same as for the simulation of the final model as described in the next paragraph) with each model having a unit (as marked in Figure 5.6a) of the boundary with no oxygen atom columns, or one fully occupied O atom column for one bright peak position and the other one only half O occupied atom column, or fully occupied O atom columns for these two bright peaks, respectively. The simulation results are shown in Figure 5.5. Clearly, from the difference of the intensity of the spots, these very bright peaks in the BF image are unambiguously identified as fully occupied O atom columns (as marked in green circle in Figure 5.5). Regarding the positions of those O atoms in the Fe-O columns (viewing in the <100> direction), their positions are presumed to have almost the same (y, z) values as those O atoms in the columns with only O atom occupied (here we used averaged value) but with half unit cell shifted in the x direction with respect to B-site atoms positions (for the x, y, z direction see Figure 5.6). This is because that contrast from these O atoms are normally shadowed by the contrast from

the B-site atoms due to their positions are almost overlapped with each other. The result of the final 3D reconstruction is shown in the structural model of Figure 5.6.

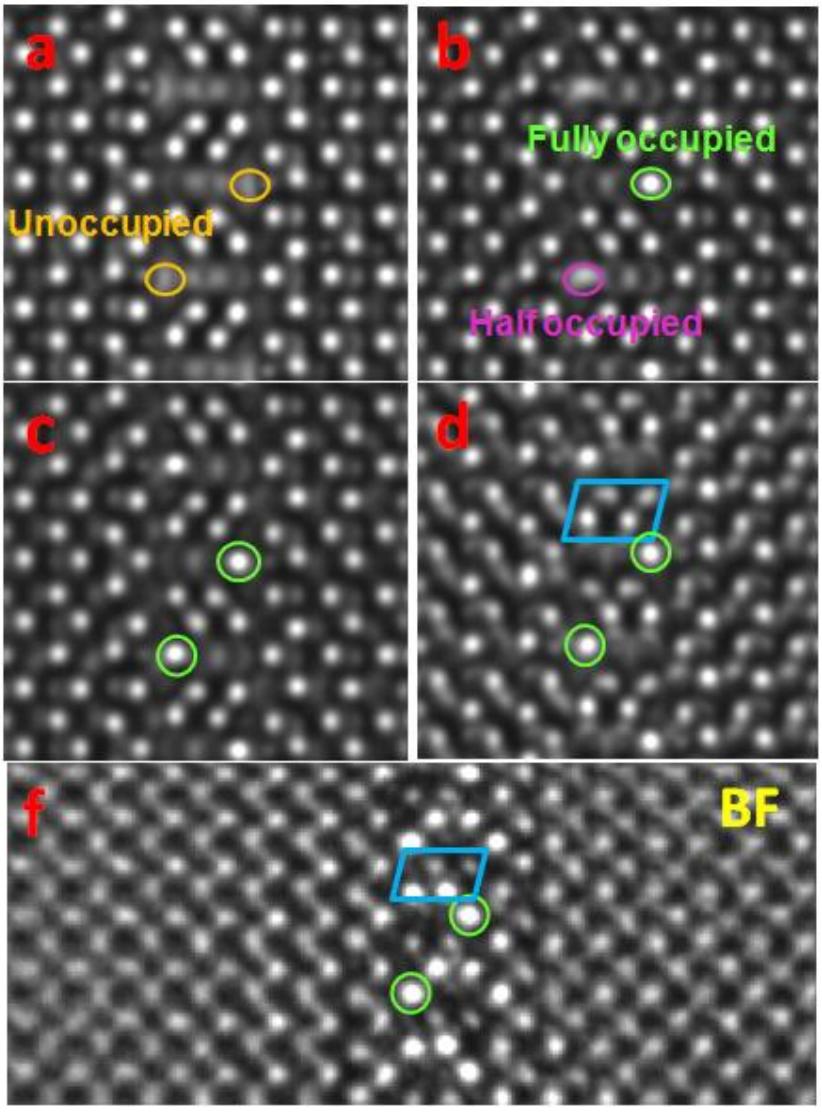

Figure 5.5. *QSTEM simulation results from different models. a) From a model with no oxygen in the unit occupies the position corresponding the very bright spot in BF image and very dark place in HAADF image. b) From a model with only one position in the unit is fully occupied by oxygen, which shows bright spot as circled, and the other one is half occupied by oxygen. c) From a model with both positions in the unit occupied by oxygen, resulting bright spots are circled as well. d) From the final model with 4 mrad-tilted angle. f) The same BF image in grey scale as was used in Figure 5.2 for the comparison with image (d). The blue parallelogram marks the two close pairs of oxygen with contrast difference between them.*

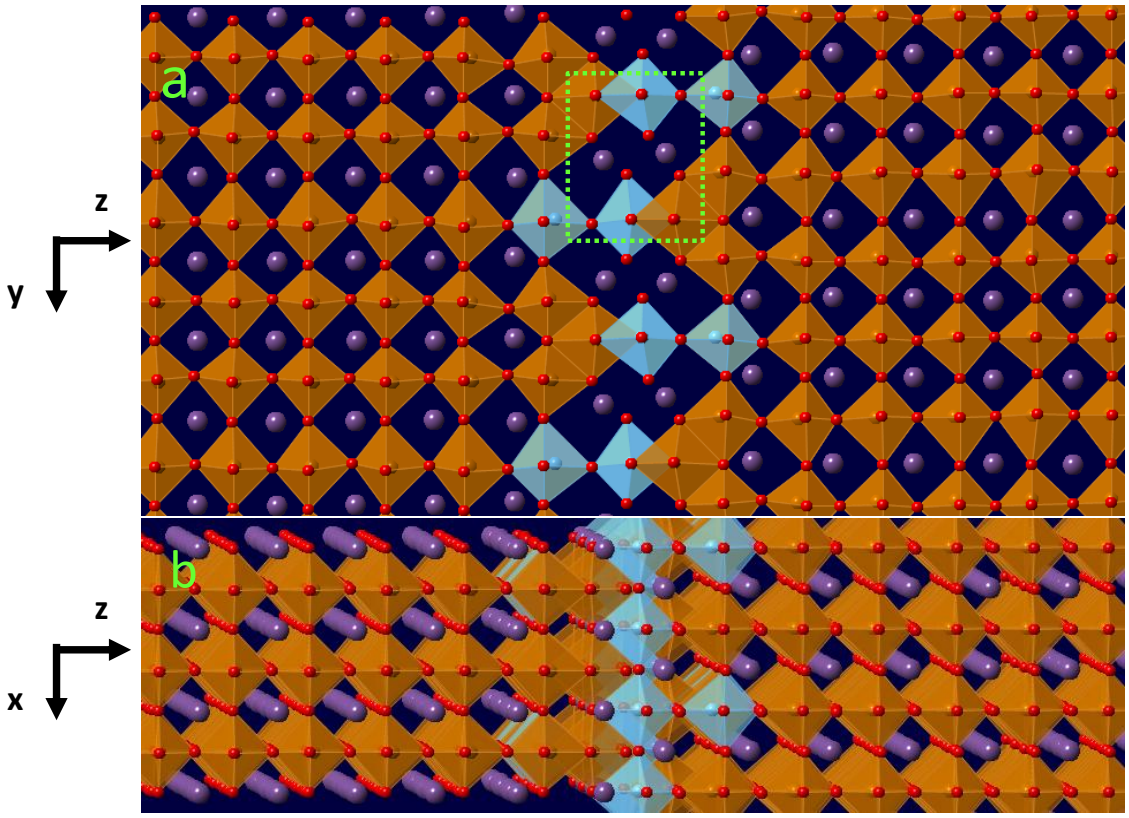

Figure 5.6. *2D visions from the final model of APB (the terrace part) with purple represents Bi atoms, red represents oxygen atoms, light blue for Ti and brown for Fe. a) Top view of the model. b) Tilted side view of the model to show the alternative B-site occupancies of Ti/Fe on either side of the terrace.*

In order to check that the way we interpreted the HAADF and BF image is really reliable, especially the bright peaks in the BF image as representing oxygen columns, image simulations with final model of fully occupied O atom columns representing the very bright peaks in the boundary were carried out using the QSTEM package of Christoph Koch [Koch 2002]. Simulations were carried out using the same conditions as mentioned in chapter 3 for QSTEM. Thicknesses of 40 primitive perovskite unit cells (~ 15.9 nm) were used for the images of Figure 5.2 (i.e. 20 supercells), and 39 primitive perovskite unit cells (i.e. 13 supercells ~ 15.5 nm) were used for the simulation in Figure 5.4. In both cases, slices of half a primitive unit cell in thickness (i.e. 1.9825 Å) were used. The frozen phonon method was used to give an average over 30 phonon configurations. The effects of a finite source size and other incoherent blurring (e.g. chromatic aberration) were simulated by convolution of the simulated images with a 0.7 Å Gaussian function. The results are overlaid on the experimental images and show

excellent qualitative agreement with the experiment and, in particular, the noticeable contrast difference between those close two pairs of O in the experimental BF image (as marked by blue parallelogram in Figure 5.5f) can be explained by the simulation result from the final model with 4mrad-tilted angle in Figure 5.5d. All of this confirms that our intuitive identification of peaks in HAADF with cation positions and peaks in BF with oxygen positions is reliable and trustworthy.

5.4 Quantitative Analysis of The APB - Step Part

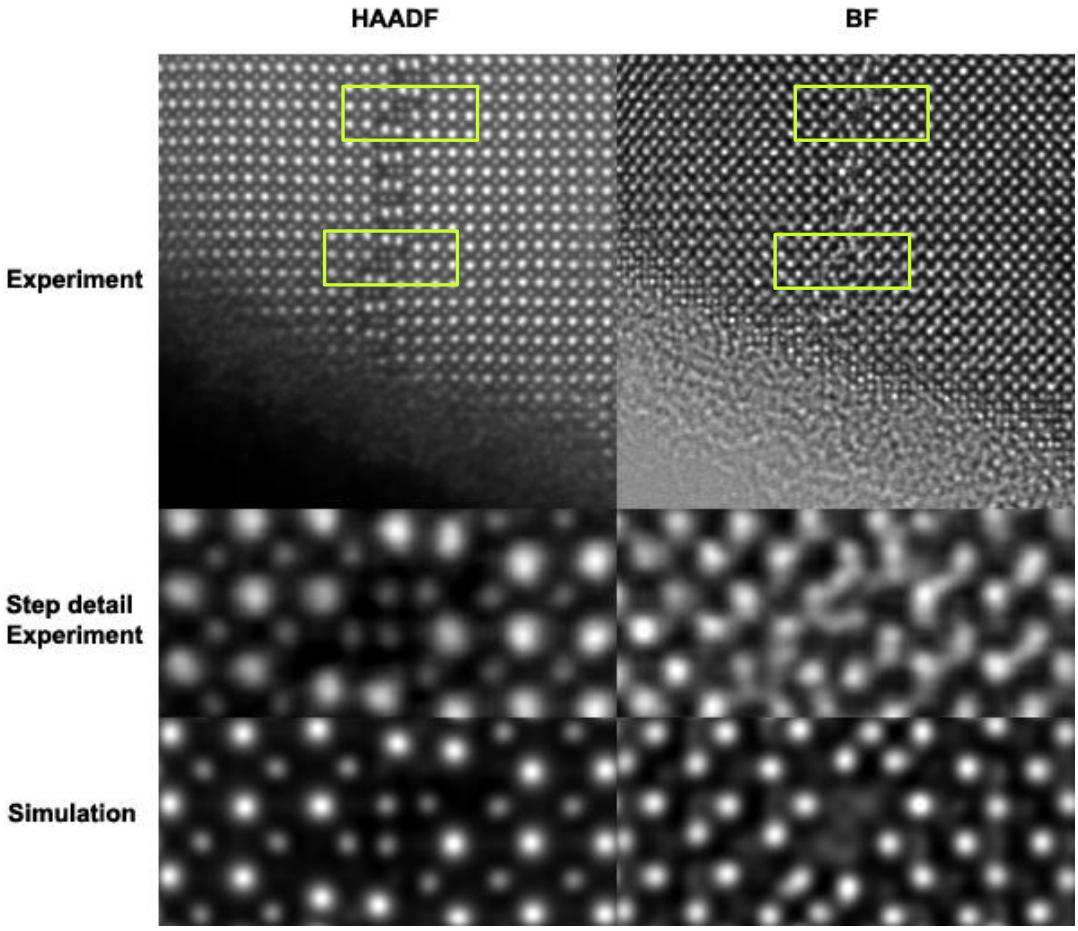

Figure 5.7. *HAADF image (left) with two steps and corresponding BF image (right); for further comparison, the lower step is magnified and displayed together with the simulation results.*

Figure 5.7 shows a HAADF image and its corresponding BF image used for our quantitative analysis of the steps. The main feature of the steps is the 4 B-site atom columns. The out of plane (vertical to the boundary) two pairs appear quite well aligned with the B-site atoms in the matrix to one side (A-site atoms on the opposite side). Each

pair could be treated as part of its terrace as their positions match quite well with the pattern of the B-site atoms within the terraces. The formation of the steps looks like the terraces with B-site atoms at each end, shifted with respect to each other by one whole unit cell. However, imaging alone does not reveal if these two pairs of B-site atoms are really the same as those pairs of B-site atoms within the terraces. Thus, chemical mapping is very important to understand them fully.

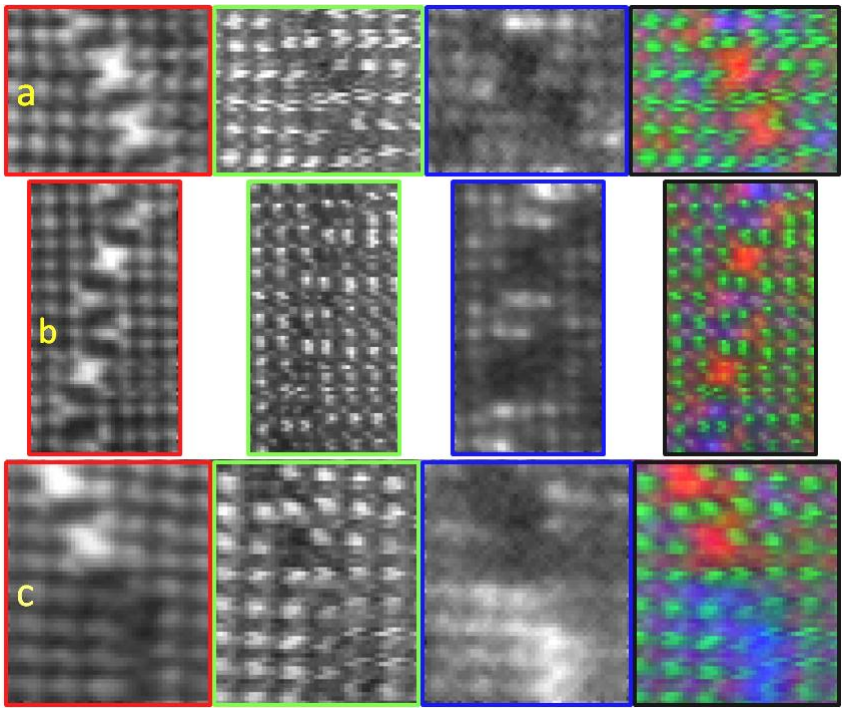

Figure 5.8. *Elemental maps from EELS of different areas as indicated by simultaneously recorded HAADF images (in green framed). Colour indications are the same as before: red for Fe, blue for Ti and green for HAADF.*

Figure 5.8 shows the elemental maps of several steps from the EELS we recorded from different areas, together with simultaneously recorded HAADF images to show the heavy A-site atom positions in the RGB images. Figure 5.8a is from an area with two steps following each other and a little bit terrace on the top of the upper step. Figure 5.8b is from an area with two steps separated by a terrace of only one unit (see Figure 5.6a about unit definition) length in between and half a unit of terrace following each step on the other side. Figure 5.8c is from an area with two steps on the top without any terrace between them, and then followed by the edge-on view of the boundary. The strong Ti segregation to the terraces in either viewing orientation is consistent with the

results discussed in section 5.3. Apart from this, Ti atom columns are also distributed near the edge of the steps and the terraces. Critically, however, the steps are actually very rich in Fe with little or no Ti. This indicates that the pairs of B-site atoms in the step are very different from the pairs of B-sites atoms in the terrace within which the central columns are occupied by Ti with columns to the left and right of the central Ti alternately occupied by part Ti and part Fe (see Figure 5.6b).

To investigate the chemical environment surrounding the Fe ions in the step, the multiple linear least squares (MLLS) fitting routine in DM was employed by fitting reference spectra that represent the main phases present to the datasets recorded. With the spectrum-image (SI) technique, reference spectra with fingerprints can be extracted directly from SI dataset and the resulting fit-coefficient maps can be interpreted as the chemical phase distribution of these particular spectra. As the fingerprint of oxygen K-edge spectrum is particularly sensitive to the nature of the 3d-orbitals of the transition-metal oxides [Brydson 2000, Docherty 2001, Park 2008], oxygen K-edge spectrum from the perovskite and steps were chosen as the reference spectra. Figure 5.9 shows the fit-coefficient maps corresponding to these two reference spectra which are shown below the maps, together with the Fe $L_{2,3}$ edge fine structure displayed as well. Obviously, the distribution of oxygen in the step is very different from that of the perovskite but similar to the distribution of oxygen of Fe-O bond from the edge of the terrace as marked by the yellow box in the fit-coefficient map. The O K-edge fine structure shown here from the perovskite is in good agreement with theoretical calculation and others' experimental reports [Park 2008, Saeterli 2010]. Comparing the oxygen energy loss near edge structure (ELNES) from the step with those of α/γ - Fe_2O_3 reported by Paterson *et al.* [Paterson 1990], the chemical structure of the step is more like γ - Fe_2O_3, characterized by the splitting shape of the first peak above 528ev. This splitting is determined by the hybridization of O 2p with the Fe 3d states. No significant difference of splitting can be observed between the threshold peak (around 538eV) of the step and that of both type of the Fe_2O_3, which is associated with the hybridization of oxygen 2p character with the Fe 4sp states [de Groot 1989]. The discrepancy of the intensity ratio of the first peak with respect to the threshold peak can be explained by the number of unoccupied 3d states available for mixing with O 2p states. In our case, it seems the ratio is bigger than that from γ - Fe_2O_3 reported by Paterson *et al.*. This may be due to the small distortion

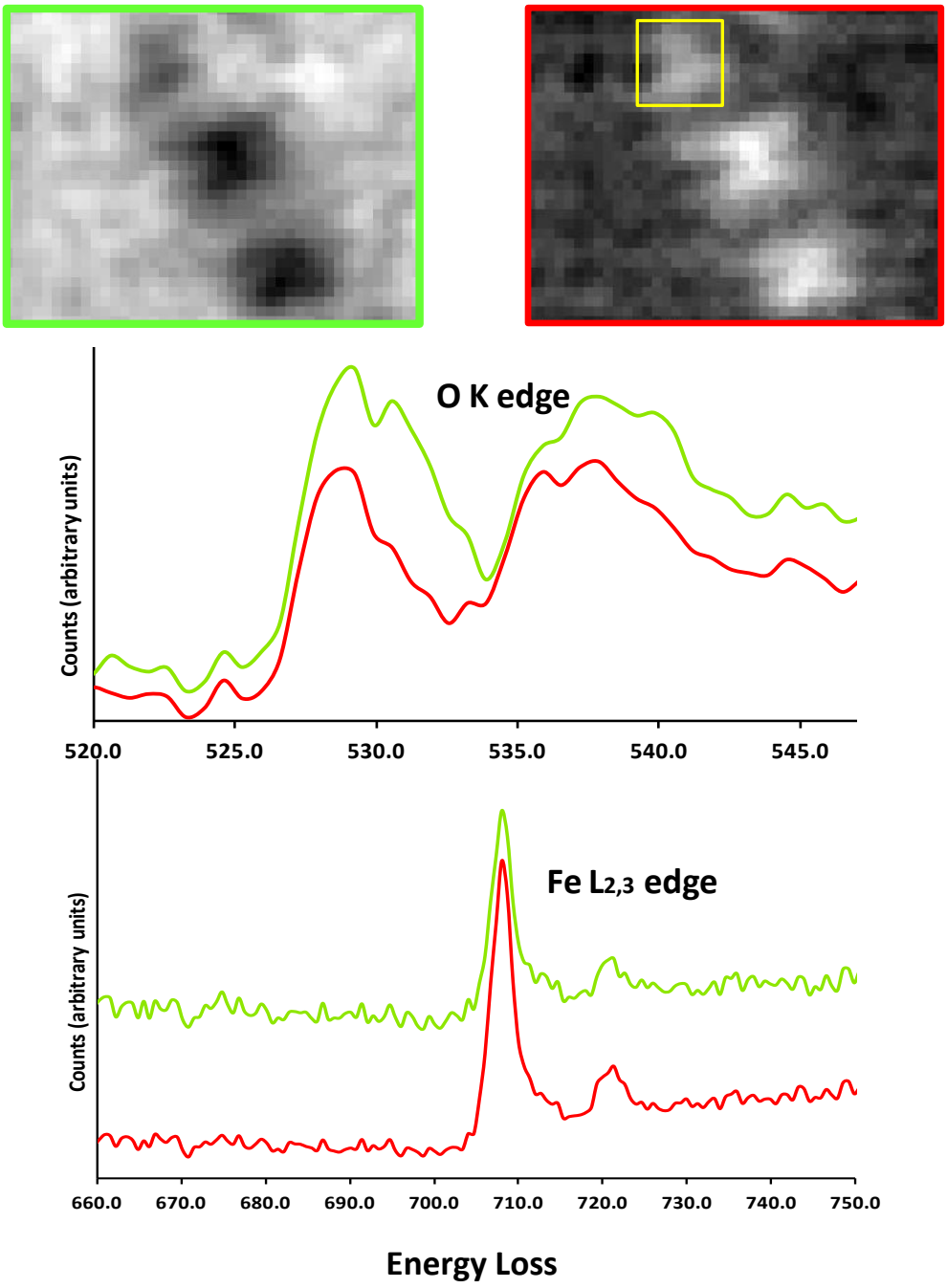

Figure 5.9. *Co-efficient fitting maps corresponding to the O K-edge reference spectra as displayed below and Fe ELNEFS. (Green colour represents the spectrum from the perovskite and red represents the spectrum from the step). Maps are smoothed by the application of a low pass filter and O K-edge and Fe ELNEFS are from PCA reconstructed EELS.*

that decreases the exchange splitting resulting more unoccupied 3d states available. Taking a closer look at the Fe $L_{2,3}$ edge, none of the splitting on the lower energy side of the L_3 white line due to the octahedral crystal field has been observed, which would mean that Fe^{3+} ions in the step are very unlikely to be octahedral coordinated. However, it is apparent that the L_3 peaks are broadened in both spectra from the perovskite and the step. The absence of the splitting and the broadening of the L_3 peak indicate that the lattice is somehow distorted due to the chemical doping [Brydson 1989], which is more likely to be the psuedotetragonal structure when comparing the Fe ELNEFS with those reported by Krishnan [Krishnan 1990] and Rossell *et al*. [Rossell 2012].

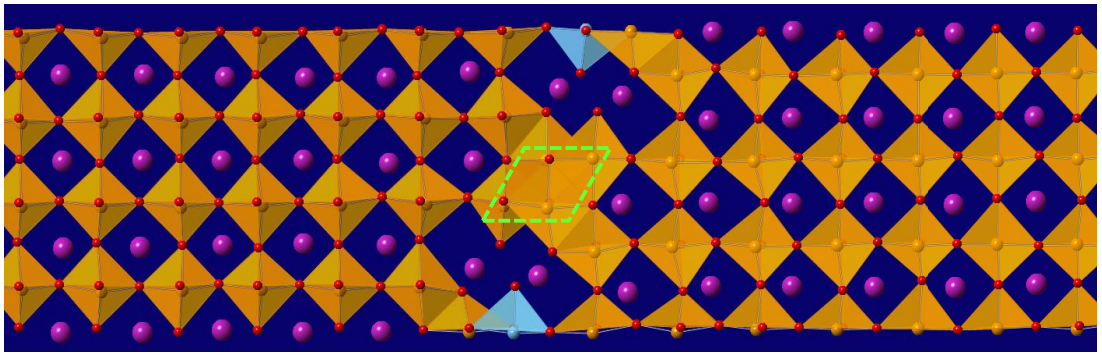

Figure 5.10. *Top view of the 3D structural model for APB (step part) with main feature of the step marked with bright green parallelogram.*

A 3D structural model of the step is shown in Figure 5.10, which was constructed using the same techniques of combining atom positions from imaging and atom identity from spectrum imaging as were used in chapter 4 for nanorods and in this chapter for APB terraces; this included BF imaging to determine oxygen positions. However, for the step, as the second projection of <001> direction gives overlaps and no clear atomic resolution images of steps from this orthogonal direction. Therefore, the third dimension of the model was constructed by using the knowledge of normal bonding in perovskites and the insights about the bonding in the boundary from the terrace structures. Data of two steps from HAADF and BF images in Figure 5.7 were averaged to get the final positions for the atoms. However, due to the bending effects near the edge of the sample as sample becomes very thin together with serious scanning distortions at the left-hand side of the boundary, errors are slightly worse than for the terrace analysis, with averaged values of about 25 pm. Again to simplify the model, a

similar idea was adopted as for the terrace part above. It was assumed that the co-ordination of atoms to either side of the boundary was perovskite like; outside of the boundary, all the A-site atoms are Bi and all the B-site atoms are occupied with Fe though in reality there should be some Nd and Ti distributed randomly. To verify the validity of the model, again simulation was carried out using QSTEM. Simulation conditions corresponding to the experiment were the same as for the terrace. Thicknesses of 40 primitive perovskite unit cells (~ 15.6 nm) and slices of half a primitive unit cell in thickness (i.e. 1.95 Å) were used. Magnified versions of the HAADF and BF images are shown in Figure 5.7 next to simulations, and it is clear that all key features are reproduced in the simulations, giving confidence in the proposed 3D model.

5.5 The Effect of The APB with Its Adjacent Matrix

On inspection of the model of the terrace, it is obvious that the first layer to either side of the boundary is massively distorted with a much larger Bi-Bi spacing than in bulk bismuth ferrite. The variation of the Bi-Bi layer spacing was quantified and plotted against position in Figure 5.11a and shows a clear variation from a peak value of about 4.3 – 4.4 Å near the boundary, decaying in about 3-4 unit cells distance to the value close to the bulk lattice parameter of 3.965 Å. Highly distorted unit cells have first been reported in highly compressively strained $BiFeO_3$ thin films [Zeches 2009], and have also been seen around nanorod defects in doped bismuth ferrite as discussed in chapter 4 and our published work [MacLaren 2012]. Such highly strained pseudotetragonal bismuth ferrite phases are typically associated with a strong off-centering of the B-site atom from the cell defined by the A-site atoms, and a consequent large polarisation. This has been shown to go up to 1.50 C m^{-2} in extreme cases of the pseudotetragonal phase [Zhang 2011]. (Compare this to 0.8 C m^{-2} for a highly tetragonal, titanium-rich lead zirconate titanate [Jia 2008]). In the present case, it seems that a similar tetragonal-like phase is present near the APB with a large polarisation easily visible in the overlay of HAADF and BF images in Figure 5.2 where the oxygen columns appear to be strongly displaced away from the boundary and the bismuth columns appear strongly displaced towards the boundary. Using a similar method that has been used previously for other perovskites [Seidel 2009, MacLaren 2012], the

resulting polarisation was calculated from the measured atomic displacements relative to their ideal atoms positions using

$$\vec{P} = \sum_i q_i \vec{u}_i$$

where q_i is the Born effective charges for the *i*-th ion and $\vec{u}_i$ is its displacement with respect to the ideal perovskite position. The values of the Born effective charges are the same as those given by Kan *et al.*[Kan 2010] e.g. $q_{Bi} = 6.2$, $q_{Fe} = 3.9$, $q_{O_1} = -2.5$, (for transverse O), $q_{O_2} = -3.4|e|$ (for Oxygen's parallel direction being along the Fe-O-Fe bond). The error bars were calculated from the standard deviation in the out-of-plane atomic position measurement after averaging as shown in Figure 5.11.

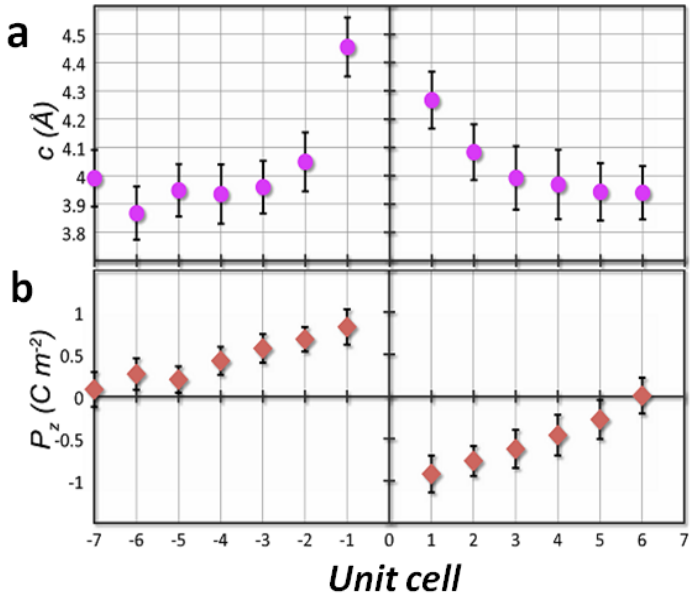

Figure 5.11. *a) Out-of-plane lattice parameter dependence on distance from the boundary; b) local polarisation dependence on distance from the boundary.*

Due to the effect of polarization, a slight asymmetry in the positions of the light atoms with respect to the heavy atoms across the whole image can be observed. This has been seen in earlier work [MacLaren 2012, Lubk 2012]. For the purposes of the polarisation calculation only, this was symmetrised by shifting all Bi atoms 10 pm to the left and all Fe/Ti atoms 5 pm to the left with respect to the unshifted oxygen positions. These figures are purely phenomenological and give an approximately symmetric

polarisation distribution across the boundary but this treatment should not change the tendencies discussed below.

The out-of-plane polarisation shows a clear peak immediately to either side of the boundary to about 0.8 – 0.9 Cm^{-2} and decays rapidly over about 5-6 unit cells to approximately zero. It should also be noted that the polarisation changes sign abruptly at the boundary [Figure 5.11b]. This indicates that there is a strong **E** field radiating out from the boundary which is then polarising the perovskite, Ti and Nd, co-doped $BiFeO_3$ resulting in a transformation from its bulk phase, which is an antiferroelectric with a $PbZrO_3$-like structure [Levin 2010, Kalantari 2011], into a tetragonally-distorted, polarised phase. The presence of this **E** field indicates that there is an excess negative charge at the boundary. The amount of excess charge can be calculated from the quantitative 3D models of Figure 5.6 and Figure 5.10. The repeat units for terrace and step are shown in Figure 5.12, correspondingly. Within one perovskite unit cell thickness, there are 2 Ti^{4+} atoms, 2 Fe^{3+} atoms, 4 Bi^{3+} atoms and 14 O^{2-} atoms for terrace. This gives a total charge of -2e. This results in an excess charge density on the antiphase boundary of -0.68 Cm^{-2}. As for the step, within one perovskite unit cell thickness, there are 4 Fe^{3+} atoms, 2 Bi^{3+} atoms and 10 O^{2-} atoms, which gives total charge of -2e. Thus the resulting charge density on the boundary is -1.08Cm^{-2}, which may well result in even stronger electric fields around steps, although the determination of whether this results in stronger polarisation of the surrounding perovskite around the steps is still a work in progress. The very formation of this negatively charged APB could be explained as follows. When the doping level is low (<1%), Ti^{4+} compensates for the oxygen vacancies and Fe^{2+}. But when the level exceeds 1%, extra Ti^{4+} substitution is more likely causes Nd-vacancies thus driving the formation of Nd-cored nanorod precipitates, as well as Ti segregating to the edges of such precipitates [Reaney 2012, MacLaren 2012]. Although nanorod precipitates are still formed at lower doping levels such as 3%, such APBs have not been observed in samples with such a low level of Ti doping. Thus, the extreme Ti doping is more likely to induce the formation of the APBs reported here as the excess Ti cannot be dissolved by just forming the nanorods. The formation of this charged APB therefore has two driving forces: firstly, they will accommodate many titanium atoms, thus taking them out of solid solution; and secondly, these negatively charged anti-phase boundaries will provide a charge balance

for the excess positive charge of Ti^{4+} substitution in the matrix, which can be visualized in Figure 5.8 where some Ti columns in the periphery of the terrace and steps apart from those Ti columns in the core of the APB can always be seen. At the cost of precipitating some Fe^{3+} out of the solution to form iron oxide at the steps, negative charged steps also help to compensate the charge of excess Ti^{4+} at the periphery of the steps. All in all, the very formation of these nonstoichiometric whole APBs is clearly driven by the overdoping with Ti^{4+} and deals with this both directly in absorbing Ti, as well as indirectly in compensating excess charge from Ti in the perovskite.

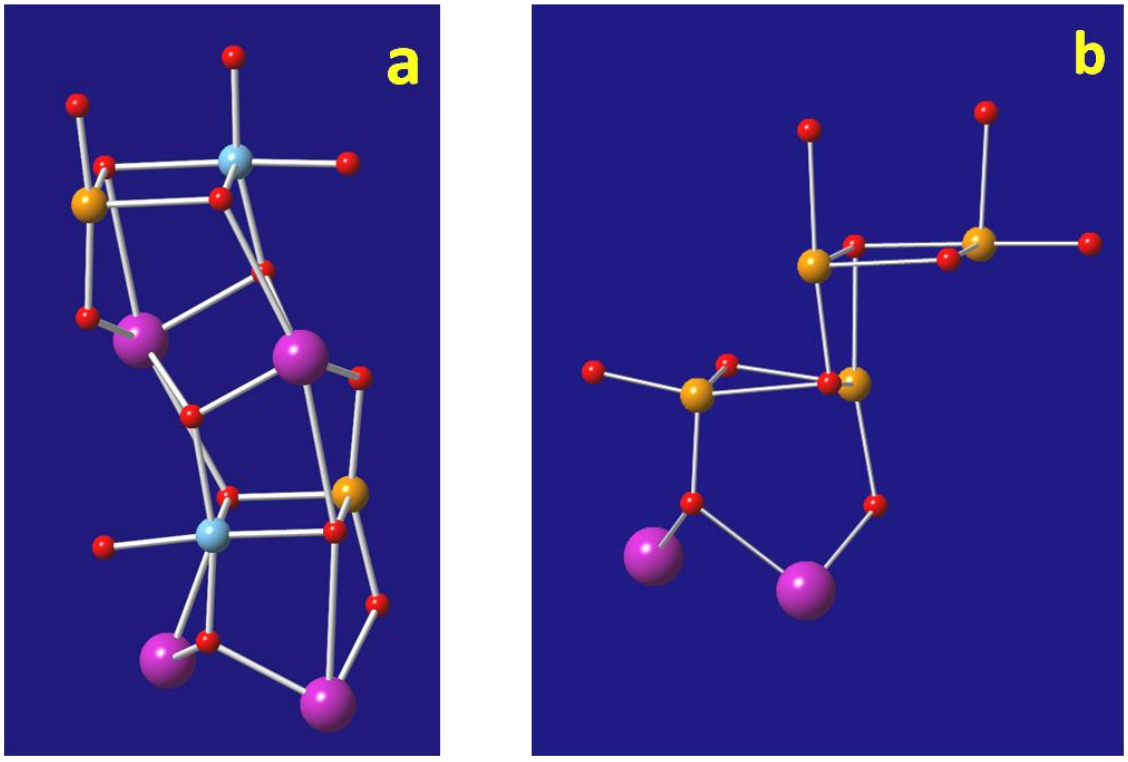

Figure 5.12. *The repeat units for the calculation of charge densities for terrace (a) and for step (b); purple for Bi, brown for Fe, light-blue for Ti and red for O.*

5.6 Conclusions

In summary, a very unusual structure of APB with sample of composition of BNFT-15_10 has been shown and elucidated. The 3D structure of this boundary was recovered by combining HAADF and BF imaging to determine the ion positions, together with atomic resolution EELS. Multislice frozen phonon simulations of the BF and DF images were carried out using the reconstructed APB structure as an input. Simulation results are in good qualitative agreement with experimental images, thereby

validating positions of O columns from BF images. The formation of this novel APB is caused by the over doped Ti into the material. The effect of this unusual APB on its surroundings is dramatic, causing a massive polarisation in ~4-5 unit cells either side of the terraces to peak values of ~0.9 Cm^{-2} within a pseudotetragonal phase rather than the orthorhombic antiferroelectric phase found throughout the bulk of the material away from such APBs though further quantification of polarisation around steps need to be done.

It may worth pointing out that the model for the APB is totally based on the experimental information from HAADF and BF images from STEM, which results in the conclusion that the APB is negatively charged. It may be noted that this is slightly different to the approach adopted in chapter 4, where strict charge neutrality was assumed at the unit cell level. There is, however, no evidence currently to challenge this assumption for the nanorods, although direct imaging of the oxygen columns in the nanorods would be required in order to confirm or deny any assumptions about absolute oxygen content across such defects, and this would require further work that is beyond the scope of the present thesis.

References:

Brydson R., Sauer H., Engel W., Thomass J. M., Zeitler E., Kosugi N., Kuroda H., **(1989)** Electron energy loss and x-ray absorption spectroscopy of rutile and anatase: a test of structural sensitivity, J. Phys.: Condens. Matter **1,** 797-812.

Brydson R., **(2000)** A brief review of quantitative aspects of electron energy loss spectroscopy and imaging, Mater. Sci. Tech. 1**6**(10), 1187-1198.

de Groot F. M. F., Grioni M., Fuggle J. C., **(1989)** Oxygen 1s x-ray-absorption edges of transition-metal oxides, Phys. Rev. B **40**(8), 5715-5723.

Ding Y. and Liang D. D., **(2002)** A model of phase transition induced antiphase boundaries in perovskite and layered perovskite oxides, J. Appl. Phys. **92**(9), 5425.

Docherty F. T., Craven A. J., McComb D. W., Skakle J., **(2001)** ELNES investigations of the oxygen K-edge in spinels, Ultramicroscopy **86**, 273–288.

Goldschmidt V. M., **(1926)** Die Gesetze der Krystallochemie, Die Naturwissenschaften **21**, 477–485

Guymont M., **(1978)** Domain structures arising from transitions between two crystals whose space groups are group-subgroup related, Phys. Rev. B **18**(10), 5385.

Jia C. L., Nagarajan V., He J. Q., Houben L., Zhao T., Ramesh R., Urban K., Waser R., **(2007)** Unit-cell scale mapping of ferroelectricity and tetragonality in epitaxial ultrathin ferroelectric films, Nat. Mater. **6**, 64-69.

Kalantari K., Sterianou I., Karimi S., Ferrarelli, M. C., Miao S., Sinclair D. C., Reaney I. M., **(2011)** Ti-doping to reduce conductivity in $Bi_{0.85}Nd_{0.15}FeO_3$ ceramics, Adv. Func. Mater. **21**, 3737-3743.

Kan D., Palova L., Anbusathaiah V., Cheng C. J., Fujino S., Nagarajan V., Rabe K. M., Takeuchi I., **(2010)** Universal behavior and electric-field-induced structural transition in rare-earth-substituted $BiFeO_3$, Adv. Funct. Mater. **20**, 1108–1115.

Koch C., **(2002)** Determination of core structure periodicity and point defect density along dislocations. *PhD Thesis*, Arizona State University.

Krishnan K. M., **(1990)** Iron $L_{2,3}$ near-edge fine structure studies, Ultramicroscopy **32**, 309-311.

LeBeau J. M., D'Alfonso A. J., Findlay S. D., Stemmer S., and Allen L. J., **(2009)** Quantitative comparisons of contrast in experimental and simulated bright-field scanning transmission electron microscopy images, Phys. Rev. B **80**, 174106

Lebedev O. I., Van Tendeloo G., Abakumov A. M., Amelinckx S., Leibold B., Habermeier H. U., **(1999)** A study of the domain structure of epitaxial $La_{1-x}Ca_xMnO_3$ films by high-resolution transmission electron microscopy, Philos. Mag. A, **79(**6), 1461-1478.

Levin I., Karimi S., Provenzano V., Dennis C. L., Wu H., Comyn T. P., Stevenson T. J., Smith, R. I., Reaney I. M., **(2010)** Reorientation of magnetic dipoles at the antiferroelectric-paraelectric phase transition of $Bi_{1-x}Nd_xFeO_3$ ($0.15 <= x <= 0.25$), Phys. Rev. B. **81**(2), 020103.

Lubk A., Rossell M. D., Seidel J., He Q., Yang S.Y., Chu Y.H., Ramesh R., Hytch M. J., Snoeck E., **(2012)** Evidence of sharp and diffuse domain walls in $BiFeO_3$ by means of unit-cell-wise strain and polarization maps obtained with high

resolution scanning transmission electron microscopy, Phys. Rev. Lett. **109**, 047601.

MacLaren I., Villaurrutia R., Pelaiz-Barranco A., **(2010)** Domain structures and nanostructures in incommensurate antiferroelectric $Pb_xLa_{1-x}(Zr_{0.9}Ti_{0.1})O_3$, J. Appl. Phys. **108**, 034109.

MacLaren I., Villaurrutia R., Schaffer B., Houben L., Pelaiz-Barranco A., **(2012)** Atomic-scale imaging and quantification of electrical polarisation in incommensurate antiferroelectric lanthanum-doped lead zirconate titanate, Adv. Func. Mater. **22**(2), 261-266.

MacLaren I., Wang L. Q., Schaffer B., Ramasse Q. M., Craven A. J., Selbach S. M., Spaldin N. A., Miao S., Kalantari K. and Reaney I. M., **(2013)** Novel Nanorod Precipitate Formation in Neodymium and Titanium Codoped Bismuth Ferrite, Adv. Func. Mater., **23,** (2), 683-689.

Park T. J., Sambasivan S., Fischer D. A., Yoon W. S., Misewich J. A., Wong S. S., (**2008)** Electronic structure and chemistry of iron-based metal oxide nanostructured materials: a NEXAFS investigation of $BiFeO_3$, $Bi_2Fe_4O_9$, α-Fe_2O_3, γ-Fe_2O_3, and Fe/Fe_3O_4, J. Phys. Chem. C **112**, 10359–10369.

Paterson J. H. and Krivanek O. J., **(1990)** ELNES of 3d transition-metal oxides II. Variations with oxidation state and crystal struture, Ultramicroscopy **32**, 319-325.

Reaney I. M., MacLaren I., Wang L. Q., Schaffer B., Craven A., Kalantari K., Sterianou I., Karimi S., Sinclair D. C., **(2012)** Defect chemistry of Ti-doped antiferroelectric $Bi_{0.85}Nd_{0.15}FeO_3$, Appl. Phys. Lett. **100**, 182902.

Rossell M. D., Erni R., Prange M. P., Idrobo J. C., Luo W., Zeches R.J., Pantelides S. T., Ramesh R., **(2012)** Atomic structure of highly strained $BiFeO_3$ thin films, Phys. Rev. Lett. **108**, 047601.

Saeterli R., Selbach S. M., Ravindran P., Grande T., Holmestad R., **(2010)** Electronic structure of multiferroic $BiFeO_3$ and related compounds: electron energy loss spectroscopy and density functional study, Phys. Rev. B **82**, 064102.

Seidel J., Martin L. W., He Q., Zhan Q., Chu Y. H., Rother A., Hawkridge M. E., Maksymovych P., Yu P., Gajek M., Balke N., Kalinin S. V., Gemming S., Wang

F., Catalan G., Scott J. F., Spaldin N. A., Orenstein J., Ramesh R., **(2009)** Conduction at domain walls in oxide multiferroics, Nat. Mater. **8**, 229-234.

Van Aert S., Batenburg K. J., Rossell M. D., Erni R. & Tendeloo G. V., **(2011)** Three-dimensional atomic imaging of crystalline nanoparticles, Nature **470,** 374-377.

Van Tendeloo G., Lebedev O.I., Hervieu M., Raveau B., **(2004)** Structure and microstructure of colossal magnetoresistant materials, Rep. Prog. Phys. **67**, 1315–1365.

Zeches R.J., Rossell M. D., Zhang J. X., Hatt A. J., He Q., Yang C. H., Kumar A., Wang C. H., Melville A., Adamo C., Sheng G., Chu Y. H., Ihlefeld J. F., Erni R., Ederer C., Gopalan V., Chen L. Q., Schlom D. G., Spaldin N. A., Martin L. W., Ramesh R., **(2009)** A strain-driven morphotropic phase boundary in $BiFeO_3$, Science **326,** 977.

Zhang J. X., He Q., Trassin M., Luo W., Yi D., Rossell M. D., Yu P., You L., Wang C.H., Kuo C. Y., Heron J. T., Hu Z., Zeches R. J., Lin H. J., Tanaka A., Chen C.T., Tjeng L. H., Chu Y.H., and Ramesh R., **(2011)** Microscopic origin of the giant ferroelectric polarization in tetragonal-like $BiFeO_3$, Phys. Rev. Lett. **107,** 147602.

Chapter 6 Summary and Future Work

6.1 Summary

Over more than one decade, BFO has once again received tremendous attention from researchers due to its ferroelectric and antiferromagnetic properties, together with a potential ME effect at room temperature if a stronger coupling between the ferroelectricity and weak ferromagnetism could be induced. This would enable device applications such as non-volatile magnetic storage with information written using a voltage and read using a magnetic field. However, high conductivity and weakly canted ferromagnetism has put a great restriction on its widespread application. Nd and Ti co-doping have proved to be a very effective way to reduce the conductivity caused by the electron hopping between Fe^{2+} and Fe^{3+}. A series of Nd^{3+} and Ti^{4+} co-doped BFO compositions have been studied in this work using a combination of atomic resolution imaging and spectroscopy in STEM, especially concentrating on nanostructures within the $Bi_{0.85}Nd_{0.15}Fe_{0.9}Ti_{0.1}O_3$ composition, as nanostructures can play an important role in the properties of a crystal. The work presented here has demonstrated that Nd and Ti co-doping induced spontaneous formation and self-assembly of Nd-rich nanorods, and the formation of novel APBs. A thorough investigation of their structure and chemistry was carried out. The 3D structure of these novel nanorods and APBs were fully and reliably reconstructed. The electronic structure of the nanorods was additionally studied with density functional calculations. A summary of this work is as follows:

1) The structure of the nanorods is Nd oxide, which has 7-coordinated Nd, with surrounding interfacial region of "T-phase-like" BFO matrix, which bridges the lattice mismatch and strain between the nanorods and bulk BFO. The interplay between the strain of the surrounding matrix and the structure of nanorods is important for the stabilisation of nanorods and their spontaneous alignment correlating with the domain structure in the $BiFeO_3$ matrix.

2) The very formation of nanorods is caused by the excess Ti doping to the B-sites resulting in the creation of Nd vacancies to compensate the solution of extra Ti^{4+}. Additionally, when Ti doping level is extremely high (>3%), these high Ti levels are not only the trigger for the formation of nanorods but also for the formation of APBs, which also accommodate some of the excess Ti.

3) The detailed study of nanorods has shed light on a new ionic compensation mechanism as proposed in our published work [Reaney 2012], i.e. at Ti lower doping level (<1%), Ti^{4+} substitution is to eliminate the Fe^{2+} thus suppresses the polaron hopping between Fe^{2+} and Fe^{3+}; at higher level, the excess Ti^{4+} has substituted the Fe^{3+} resulting the creation of Nd vacancies by the formation of nanorods. Consequently, the formation of nanorods gives at least a partial explanation to the suppression of the semi-conductivity and the non-linear dependence of T_c for Ti-doped $Bi_{0.85}Nd_{0.15}FeO_3$.

4) Electronic structure calculations predicted that the distorted, T-phase like regions surrounding the nanorods have higher electrical conductivity than the surrounding, insulating matrix, which might pave the way to additional novel functionalities in multiferroic BFO.

5) The structure of the novel APB is also elucidated in this work. Within the terrace, Ti^{4+} ions occupied in the core of the APB while Ti^{4+}/Fe^{3+} occupied the adjacent B-sites columns alternatively. The Bi^{3+} ions in the terrace parts act like bridges joining the matrices on each side together. The step is consisted of iron oxide with structure very similar to γ-Fe_2O_3.

6) The APB is negatively charged. As a consequence, such charged APB causes the local polarization of the bulk BFO, thus a local phase transformation from antiferroelectric to ferroelectric.

6.2 Future Work

Through the thorough investigation of these novel features, good understanding of their structure and properties has been achieved. However, these fascinating features of nanorods and APBs are of great further interest, not only because of their novelty but also because of their effects on the properties of doped BFO compositions for potential future applications. Consequently, there is much still to be done. First of all, with the 3D model of APB from this work, detailed electronic structure calculations need to be done with DFT to provide a deeper understanding of its structure and transport properties. From the HAADF image, it is clear that the first layer on either side of the APB is massively distorted. The distorted structure of these layers is very similar to the "T-phase" structure. In this case, five-coordinated B-site atoms (Fe/Ti) would be expected at the edge of APB from the DFT calculation results. However, it would also be interesting

to find out the detailed coordinations of those B-sites atoms within the core of the APB, together with their electronic structures. If the B-site atoms at the edge of the APB became five-coordinated rather than six-coordinated with O, the O released from these B-sites atoms would be more involved in coordinating their neighbouring Bi and Fe/Ti ions in the core, thus these oxygen anions might have some impact on the electronic structures of those cations in the APB. Secondly, more EELS analysis regarding the oxygen and Fe near edge fine structure need to be done with atomic resolution microscopes that have dual EELS technique which allows zero-loss and core-loss spectra to be taken simultaneously. When performed at atomic resolution, such studies will enable us to quantify in detail local variations in the chemistry in this complex boundary. Thirdly, we have already shown that the excess negative charge density at the APB steps must be even higher than that on the terraces, which means the induced electric field might even stronger around the steps, therefore more quantitative analysis need to be done to check if this higher charge density causes larger polarisation in the perovskite matrix surrounding the steps. Fourthly, the monotonic decrease of T_N with Ti doping suggests the presence of the nanorods together with the induced local strain centres surrounding the nanorods may also have some influence on the precise configuration of the local magnetic dipolar order. Thus, the magnetic structure of the nanorods and its influence on the surrounding perovskite and the bulk magnetic properties requires further study using atomic-resolution magnetically sensitive imaging, either using Lorentz microscopy techniques or using new electron vortex beam techiques. Last but not least, special attention could be paid to find out the exact doping level of Ti^{4+} to rhombohedral ferroelectric compositions of $Bi_{1-x}Nd_xFeO_3$ ($x<0.115$) with which the conductivity could be reduced sufficiently to allow ferroelectric applications without the pinning effect of nanorods. This could be done using in-situ TEM and HRSTEM to monitor the interactions between the domain walls and nanorods in various compositions with different doping levels to understand how Ti doping levels affect nanorod concentrations and domain wall pinning. Although other groups have done much work regarding the growth of BFO thin films, relatively little has been done on the growth of Nd and Ti co-doped BFO thin films. The knowledge obtained here together with a further systematic study with these fascinating bulk materials will be very useful for the growth of doped thin films of potential device applications.

References

Reaney I. M., MacLaren I., Wang L. Q., Schaffer B., Craven A., Kalantari K., Sterianou I., Karimi S., Sinclair D. C., **(2012)** Appl. Phys. Lett. **100**, 182902